VILNIUS UNIVERSITY

Vytautas Jukna

CONICAL WAVE TRIGGERED TRANSIENT SPATIO-TEMPORAL EFFECTS IN KERR MEDIA

Doctoral dissertation
Physical sciences, Physics (02P)

Vilnius, 2012

The researched was performed in 2008-2012 at Vilnius University

Scientific supervisor:

prof. habil. dr. Gintaras Valiulis (*Vilnius University*, Physical Sciences, Physics - 02P)

Consultant:

prof. habil. dr. Audrius Dubietis (*Vilnius University*, Physical Sciences, Physics - 02P)

VILNIAUS UNIVERSITETAS

Vytautas Jukna

KŪGINIŲ BANGŲ NENUOSTOVŪS ERDVĖLAIKINIAI REIKŠKINIAI NETIESINĖSE KERRO TERPĖSE

Daktaro disertacija
Fiziniai mokslai, fizika (02P)

Vilnius, 2012

Disertacija rengta 2008-2012 metais Vilniaus Universitete

Mokslinis vadovas:

prof. habil. dr. Gintaras Valiulis (*Vilniaus Unviersitetas*, Fiziniai mokslai, fizika - 02P)

Konsultantas:

prof. habil. dr. Audrius Dubietis (*Vilniaus Unviersitetas*, Fiziniai mokslai, fizika - 02P)

Contents

Acknowledgements

During the slow and bumpy road of filament generation perception I have accumulated the knowledge of numerous persons and have a great debt to acknowledge at least a part of them here. I am grateful to many people who have helped me through my long study. I would like to thank all colleagues and students who contributed to this study.

I would like to express my spacial thanks to scientific supervisor Prof. Gintaras Valiulis whose suggestions, support and patience helped me all the time.

I want to express my gratitude to Lab workers who let me be a part of their team, at least for a glimpse or two. I thank for the trust and permission to use their precious lab instruments. For introduction to experiment world I am grateful to Dr. M. Clerici and Dr. G. Tamošauskas. Thanks to Dr. M. Vengris for letting to use some of his equipment. Many thanks for Dr. A. Dubietis for believing that experiment findings can and should be explained referring numerical modeling.

Materialization of the thesis would be hard without numerous STELLA schools, therefore I am grateful for Dr. P. Di Trapani, Dr. D. Faccio, Dr. O. Jedrkiewicz, Dr. A. Couairon, Dr. M. Kolesik and other who contributed in school materialization.

I am greatly in debt for all the paperwork and extra care for students to L. Mikalauskienė and Dr. D. Kaškelytė, where even a ton of chocolate and candies will not compensate the work they do.

I am thankful to Dr. D. Faccio for permission to use explanatory figures from his book. His book on filamentation is perfect for conical understanding of the process, and some of the questions which may come in mind by reading this thesis

could be answered there.

I also want to thank the former head of the Quantum Electronics Department of Vilnius University Prof. Algis Petras Piskarskas as well as present Dr. Valdas Sirutkaitis for giving the possibility to be acknowledged as laser physics researcher, and providing the necessary environment to do the research.

I am very grateful for my wife Dovile and daughter Evelina for the support and enlightening of the days. I thank my parents and other family members for the support in all my student years. Special thanks goes for the friends who did not leaved me in the need. I also want to apologize if I have inadvertently omitted anyone who had impact in my thesis.

List of the abbreviations

n_2 nonlinear refractive index.

CCD Charge-Coupled Device.

ETWM Effective Three Wave mixing Model.

FROG Frequency-Resolved Optic Gating.

FWHM Full Width Half Maximum.

FWM Four Wave Mixing.

GV Group Velocity.

GVD Group Velocity Dispersion.

HOKN Higher Order Kerr Nonlinearity.

MF Multiple Filaments.

MPA Multiphotn Absorption.

PDF Probability Density Function.

SPM Self Phase Modulation.

WLC White-Light Continuum.

XPM Cross Phase Modulation.

Chapter 1

Introduction

Long and narrow material damage string was observed from 1964 [1], however femtosecond pulse filamentation was observed for the first time by Braun *et. al.* [2] in 1995. The intense infrared pulse did not diffract during 20 meters propagation in air, but becomes focused and keeps nearly constant beam diameter over a long distance. Such effects are called self-focusing and filament generation. The first explanation of the intense peak propagation was based on idea of self-channeling (self guiding) [3]. Many scientific papers devoted to the study of intense beam propagation through various substances were published in short period. Later it was understood that filament propagation could not be explained via help of self guiding due to various causes. The moving focus [4] and dynamic spatial replenishment [5, 6] models were proposed as more suitable. Nevertheless the proposed models are capable to explain many of experimentally observed phenomena, the far field properties of filament was a mystery. It was noticed, that X wave angular dispersion closely fits the observed spatio-temporal spectrum [7], therefore the model of the filaments based on conical wave idea was proposed [8].

In 2004 it was demonstrated [9, 10], that filament which forms in nonlinear medium with Multiphotn Absorption (MPA) is a conical wave. The conical nature of filament allows to explain how filament is capable to keep nearly constant values of the peak intensity and diameter even in absorbing medium. Multiple filaments occur when the initial beam is broad and nonsymmetric. Usually, the radially symmetric (cylindrical) beams were used for filament generation. Just

recently the filament array was generated using nonsymmetric beam. In this thesis we discuss three filament generation cases: simple single filament generation, filaments generated in scattering medium and multiple filaments generation by elliptical beams.

As it was mentioned before, filament central peak is almost not influenced by absorption while propagating in nonlinear and absorbent medium. Since scattering particles creates an additional energy dissipation mechanism, the filament formation and propagation in scattering medium seems possible and deserves to be discussed. Filamentation in water with different scattering particle concentration was studied experimentally and numerically. To induce scattering the 2 μm diameter polystyrene spheres were added in water. It was discovered that filament in scattering medium formes at longer distances, but when energy losses due to scattering exceed some level the self-focusing filament do not occur at all.

Multiple filament generation by elliptical beam is appealing method to produce repeatable and stable filament arrays. It was demonstrated, that filaments generated by elliptical beam, arrange themselves on major ellipse axis, and their period depends on beam energy. Physical nature of self arrangement was not fully understood. The proposed analytic model of multifilamentation supported by numerical simulations and experimental approvement will be discussed in chapter 5.

The temporal spectrum of the radiation becomes drastically broadened when the filament is formed. That is caused by many physical effects, and among them the pulse splitting phenomenon seems is the most important. The statistical analysis of generated spectrum revealed, that intensity statistical distribution at fixed wavelength is not symmetric. At some specific wavelengthes the intensity may exceed mean value many times. A careful examination of the pulse spectral intensity profiles revealed L - shaped statistical distribution [11]. The appearance and suppression of specific statistical events will be discussed in chapter 6.

The main tasks of the thesis

Thesis is aimed to:

1. Examine supercontinuum spectra dependence on initial beam diameter.
2. Study of the filamentation in scattering medium.
3. Study of the multifilamentation with elliptical beams.
4. Search and study for rogue wave statistics in supercontinuum generation and filamentation processes.
5. Provide a unified understanding of mentioned above phenomenon via conical wave formation process.

Scientific novelty

1. The explanation of the supercontinuum spectra dependence of the initial beam diameter.
2. The explanation of the filament and supercontinuum spectra via event of pulse splitting into two X pulses with intensity dependant group velocities. The explanation of the spectrum cut-off (spectrum edge frequency values) by intensity clamping of splitted pulses.
3. The development of new numerical scheme which could be used for the investigation of almost any laser beam propagation through scattering medium.
4. The numerical observation of the small scale filamentation in scattering medium (water with the polystyrene particles).
5. The explanation of the elliptical beam multifilamentation process via cascaded four wave mixing process.
6. The explanation of the small scale intensity structures via X wave modulation instability.
7. The numeric observation, and explanation of the rogue wave statistics in the filamentation process in bulk medium, for the first time. The proposition of the rogue wave statistical suppression mechanism based on the pulse intensity clamping.

Practical value

A revealed role of the initial beam diameter to the red part of the supercontinuum, could be used for the formation of better seed in parametric amplification scheme (Such as NOPA). It was also demonstrated, that filaments are able to form and propagate through scattering medium. These results could be used in

various scattering environments when the high peak intensity radiation transmission is needed. The developed numerical scheme could be used for the study of laser beam propagation in any scattering medium. The addressing of the elliptical beam multifilamentation process to the Four Wave Mixing (FWM) and material nonlinearity, shows the possibility to control and use of the periodic filament arrays for the multichannel microfabrication. The revealed nature of the rogue wave statistics via X wave formation, gives also the recipe for the damping mechanism of the mentioned extreme events.

Statements to defend

1. Strong scattering leads to distortions of the filament energy reservoir developing an apparent speckle structure, but does not greatly alter filament formation and propagation dynamics.
2. Self-focusing of high power beams with large ellipticity leads to formation of periodic and high reproducible multiple filaments arrays. Multiple filament arrays emerge as apparently regular patterns in the space domain, the spatiotemporal dynamics of the individual filaments is governed by the input-beam power and the input-beam ellipticity.
3. In three-dimensional space, space-time coupling leads to rogue events that are associated to X-wave formation in the normal group-velocity dispersion regime.
4. In the certain input-pulse energy interval the blue-shifted spectral components of the supercontinuum exhibit large shot-to-shot intensity variations that obey extreme-value statistical distribution.

Approbation

Scientific papers related to the topic of this thesis

[**A1**] V. Jukna, G. Tamošauskas, G. Valiulis, M. Aputis, M. Puida, F. Ivanauskas, A. Dubietis, Filamentation of ultrashort light pulses in a liquid scattering medium, Appl. Phys. B **94**, 175-179 (2009).

[**A2**] D. Majus, V. Jukna, G. Valiulis, A. Dubietis, Generation of periodic filament arrays by self-focusing of highly elliptical ultrashort pulsed laser beams, Phys. Rev. A. **79**, 033843 (2009).

[**A3**] D. Majus, V. Jukna, G. Tamošauskas, G. Valiulis, A. Dubietis, Three - dimensional mapping of multiple filament arrays, Phys. Rev. A. **81**, 043811 (2010).

[**A4**] D. Majus, V. Jukna, G. Valiulis, D. Faccio, A. Dubietis, Spatiotemporal rogue events in femtosecond filamentation. Phys. Rev. A **83**, 025802 (2011).

[**A5**] D. Majus, V. Jukna, E. Pileckis, G. Valiulis, A. Dubietis, Rogue-wave-like statistics in ultrafast white-light continuum generation in sapphire, Opt. Express **19** (17), 16317-16323 (2011).

[**A6**] V. Jukna, D. Majus, G. Valiulis, A. Dubietis, Transformation of the probability density function in an optical parametric amplifier: application to rogue-wave-like statistics, Opt. Commun. **285**, 3654-3658 (2012).

Other scientific papers

[**A7**] G. Valiulis, V. Jukna, O. Jedrkiewicz, M. Clerici, E. Rubino, P. DiTrapani, Propagation dynamics and X pulse formation in phase-mismatched second harmonic generation, Phys. Rev. A **83**, 043834 (2011)

[**A8**] A.Zaukevičius, V. Jukna, R. Antipenkov, V. Martinėnaitė, A. P. Piskarskas, G. Valiulis, Manifestation of spatial chirp in femtosecond noncollinear optical parametric chirped-pulse amplifier, JOSA B **28** (12), 2902-2908 (2011).

Conference presentations

Presented by Vytautas Jukna:

[**C1**] CLEO/Europe-EQEC 2009, Miunchen, Germany, V. Jukna, D. Majus, G. Valiulis, A. Dubietis, Generation of periodic filament arrays by self-focusing of highly elliptical ultrashort pulsed laser beams, 2009.

[**C2**] COFIL 2010, Heraklion, Greece, V. Jukna, D. Majus, G. Tamošauskas, G. Valiulis, A. Dubietis, Three-dimensional mapping of multiple filament arrays, 2010.

[**C3**] CLEO/Europe-EQEC 2011, Miunchen, Germany, V. Jukna, G. Valiulis, O. Jedrkiewicz, M. Clerici, E. Rubino, P. DiTrapani, Self-phase matching and X pulse formation in phase-mismatched second harmonic generation due to dimensionality transition, 2011.

[**C4**] 39th LNFK, Vilnius, Lithuania, V. Jukna, A. Zaukevičius, R. Antipenkov, V. Martinėnaitė, A. Varanavičius, A. Petras Piskarskas, G. Valiulis, Spatial chirp and angular dispersion dynamics in femtosecond noncollinear OPCPA, 2011.

[**C5**] ASSP 2012, San Diego, USA, V. Jukna, A.Zaukevičius, R. Antipenkov, V. Martinėnaitė, A. P. Piskarskas, G. Valiulis, Spatial chirp and angular dispersion dynamics in femtosecond noncollinear OPCPA, 2012.

Co-author of the presentation:

[**C6**] 38th LNFK, Vilnius, Lithuania, D. Majus, V. Jukna, G. Valiulis, A. Dubietis, Generation of periodic filament arrays by self-focusing of highly elliptical ultrashort pulsed laser beams, 2009.

[**C7**] Northern Optics 2009, Vilnius, Lithuania, D. Majus, V. Jukna, G. Valiulis, A. Dubietis, Generation of periodic filament arrays by self-focusing of elliptical ultrashort pulsed laser beams, 2009.

[**C8**] Mokslas ir visuomenė modernioje Europoje, Vilnius, Lithuania, D. Majus, V. Jukna, G. Tamošauskas, G. Valiulis, A. Dubietis, Three-Dimensional Mapping of Multiple Filament Arrays, 2010.

[**C9**] Open readings, Vilnius, Lithuania, A.Zaukevičius, V. Jukna, R. Antipenkov, V. Martinėnaitė, A. P. Piskarskas, G. Valiulis, Spatial chirp and angular dispersion dynamics in femtosecond noncolinear OPCPA, 2011.

[**C10**] CLEO/Europe-EQEC 2011, Miunchen, Germany, D. Majus, V. Jukna, G. Valiulis, D. Faccio, A. Dubietis, Spatiotemporal rogue events in femtosecond filamentation, 2011.

[**C11**] 39th LNFK, Vilnius, Lithuania, G. Valiulis, V. Jukna, O. Jedrkiewicz, M. Clerici, E. Rubino, P. DiTrapani, X pulse formation via phase-mismatched second harmonic generation, 2011.

[**C12**] 39th LNFK, Vilnius, Lithuania, A. Dubietis, D. Majus, V. Jukna, E. Pileckis, G. Valiulis, Rogue-wave-like statistics in femtosecond white-light filaments, 2011.

Co-authors contribution

All research was done in Vilnius University, Physics faculty, department of Quantum electronics under a supervision of Habl. Dr. G. Valiulis. Experiments were held in Dr. A. Dubietis laboratory. All numerical calculations and a filamentation in scattering media experiment was done by the author himself. Nevertheless it is important to notice the significant contribution of these co-authors:

1. Habl. Dr. G. Valiulis was a guidance in all the work I've done, provided a good conditions for attaining thesis results. The proposition of four wave mixing contribution in periodicity of generated filaments by elliptical beam was also G. Valiulis idea.
2. Habl. Dr. A. Dubietis was the key person providing collaboration between theoretic and experiment part of the team.
3. The help of the Dr. G. Tamošauskas was very needful in introduction to experimental laser physics, and in performing experiments.

4. PhD student D. Majus performed some of experiments and provided data for numerical comparisons.

The knowledge in filamentation was greatly enhanced by discussions in various STELLA schools. Interpretation of supercontinuum and filamentation spectra generation was discussed various times with D. Faccio, M. Clerici and P. Di Trapani. The numerical stimulus and guidance was a result from discussions and various papers of A. Couairon.

The structure of the thesis

Thesis consists of introduction, followed by five main chapters and conclusions. Introduction is devoted to the explanation of filamentation process. The mechanisms responsible for filament generation and evolution are explained first and various models of the filamentation are presented as well. The second chapter is devoted to the study on supercontinuum spectrum dependence on the initial pulse diameter. The chapter 4 is devoted to the study of the filamentation in scattering medium, and covers the performed experiment, explanation of new developed numerical scheme, and finally comparison of the numerical and experimental results. The chapter 5 describes the multifilamentation with elliptical beam. The role of the four wave mixing to the filaments periodicity is briefly explained. The periodicity dependence on the wave of intensity as well the evolution of multifilamentation is shown. Three dimensional study of the modulation instability during multifilamentation process is also presented in chapter 5. The last chapter 6 is devoted to the origin of the rogue wave statistics in supercontinuum generation, and comparison of the numeric results with experimental. At the end (chapter 7) the main conclusions of the current work are presented.

Chapter 2

Ultrashort pulse propagation in nonlinear Kerr media

2.1 Physical processes involved in filament formation

Nonlinear propagation of intense ultrashort pulse in nonlinear Kerr medium is complicated process which rise a lot of nonlinear physical processes starting from modulation instability followed by self-focusing and unsymmetrical pulse splitting, enhanced by self steepening, non-instantaneous nonlinear response, chased by MPA, and developed plasma defocusing and absorption, also not excluding Raman contribution. Therefore we will discuss and introduce step by step the most important physical effects that occur during light filamentation process.

2.1.1 Diffraction and dispersion

Pulse transformation during propagation in linear medium is the most important issue of understanding the filament capability to overcome dispersion and diffraction. Actually, the overcoming of the diffraction means just significant suppression of the beam broadening in comparison with the standard Gaussian beam. As it is known, the Gaussian beam $A(x,y) = a_v \exp\left(-\frac{x^2+y^2}{\rho_0^2}\right)$ linear propagation in paraxial limit is described by equation:

$$\frac{\partial A}{\partial z} = -\frac{i}{2k_0}\left(\frac{\partial^2}{\partial x^2} + \frac{\partial^2}{\partial y^2}\right) A. \tag{2.1}$$

The solution remains Gaussian, but acquires parabolic wavefront

$$A(r,z) = \frac{a_v}{1-\frac{2iz}{k_0\rho_0^2}} \exp\left(-\frac{r^2}{\rho_0^2\left(1-\frac{2iz}{k_0\rho_0^2}\right)}\right), \tag{2.2}$$

where $r = \sqrt{x^2+y^2}$ is radial transverse coordinate, a_v is the initial beam peak amplitude, ρ_0 is the initial Gauss beam width, k_0 is the wave number, z is the propagation distance. Diffraction could be characterized by Rayleigh length, when collimated Gaussian beam diameter increase by factor $\sqrt{2}$:

$$Z_R = \frac{k_0\rho_0^2}{2} = \frac{\pi\rho_0^2}{\lambda_0}. \tag{2.3}$$

Namely, form Eq. 2.2 we obtain that beam width increases as

$$\frac{\rho(z)}{\rho_0} = \sqrt{1+\left(\frac{z}{Z_R}\right)^2}. \tag{2.4}$$

However, the overall beam power is constant while beam amplitude drops as

$$\frac{a_v(z)}{a_v} = \frac{1}{\sqrt{1+\left(\frac{z}{Z_R}\right)^2}}. \tag{2.5}$$

Note, that even in vacuum beam diffracts, since it is a superposition of the plane waves propagating at slightly different directions.

The pulse temporal broadening during propagation in dispersive media is analogous to the diffraction of the beam caused by Group Velocity Dispersion (GVD). It can be described by equation:

$$\frac{\partial A}{\partial z} = \frac{i}{2} g_0 \frac{\partial^2 A}{\partial t^2}, \tag{2.6}$$

where g_0 is the GVD coefficient. Initial Gaussian pulse $A(t) = a_v \exp\left(-\frac{t^2}{\tau_0^2}\right)$

during linear propagation remain Gaussian but also acquires temporal chirp

$$A(r,z) = \frac{a_v}{\sqrt{1-\frac{2izg_0}{\tau_0^2}}} \exp\left(-\frac{t^2}{\tau_0^2\left(1-\frac{2izg_0}{\tau_0^2}\right)}\right). \tag{2.7}$$

Dispersion is characterized by dispersion length, when the transform limited Gaussian pulse duration increases by factor of $\sqrt{2}$

$$L_d = \frac{\tau_0^2}{2g_0}. \tag{2.8}$$

Namely, form Eq. 2.7 pulse duration grows as

$$\frac{\tau(z)}{\tau_0} = \sqrt{1+\left(\frac{z}{L_d}\right)^2}. \tag{2.9}$$

However the amplitude decreases as

$$\frac{a_v(z)}{a_v} = \frac{1}{\sqrt[4]{1+\frac{z^2}{L_d}}}. \tag{2.10}$$

Note, that both diffraction and dispersion sustain Gaussian shape of the wave packet but lead to phase modulation. Moreover, pulse chirp sign is defined by the sign of the GVD coefficient g_0. Here, just the second order dispersion terms are discussed. Higher order terms become important for ultrashort pulses and makes pulse profile and phase modulation nonsymmetric. The sign of the GVD coefficient is the most important since it defines the main features of the filamentation spectrum. The higher order dispersion terms affect filament spectral components far from the central frequency and do not change significantly the topology of the far field. Nevertheless, in order to have good agreement between numerical results and experiment, the higher order dispersion terms should be included (or even total dispersion of the material).

2.1.2 Self-focusing

High intensity light propagating in transparent nonlinear material modifies its refractive index *i. e.* the refractive index depends on intensity $n = n_0 + n_2^{(I)} I$. The most materials under usual experimental conditions possess positive nonlinear refractive index (n_2) value, and only a bunch of materials have negative one. Some materials have complex and pronounced n_2 dependence on wavelength [12], some of materials have complicated n_2 dependence on time [13]: the n_2 sign can change from positive to negative. Nevertheless usually the filaments are generated and studied in media with not so complex n_2 behavior.

The beam with transverse intensity distribution $I = I(x, y)$ produces transversely dependant refractive index change. Obviously, phase velocity in most intense part of the beam becomes less than in low intensity peripheral part, consequently, the plane wave front of the beam starts to sag during beam propagation and overall beam starts to self-focus. Self-focusing of the beam was predicted in 1964 by R. Chiao, E. Garmire and C. Townes [14]. When the beam power exceeds some critical value it collapses (blows up) in finite distance. The distance where collapse occur is called critical distance. The most used expression is Dawes-Marburger, which estimates Gaussian beam collapse distance:

$$z_c = \frac{0.367 Z_R}{\sqrt{\left[\left(\frac{P_0}{P_c}\right)^{1/2} - 0.852\right]^2 - 0.0219}}, \tag{2.11}$$

where Z_R is Rayleigh length, P_0 is initial beam power, $P_c = \alpha \frac{\lambda^2}{8\pi n_0 n_2}$ is critical power for self- focusing. Expression 2.11 is retrieved by fitting numerical simulation results to nonlinear function. The first attempt was not accurate [15], but after Marburger [16] retrieved expression used up to now [17]. More accurate is Fibich proposed empiric formula [18]:

$$z_c = 0.317 Z_R \left(\frac{P_0}{P_c} - 1\right)^{0.6346}, \tag{2.12}$$

which has relative accuracy of 1%, while Marburger's expression 2.11 has about 10%.

The collapse of the wavepacket can be arrested by various effects. The most important phenomenon is MPA [19] as well as the defocusing of plasma. Additionally, when pulse duration is very short material dispersion is also capable to arrest collapse [20]. Moreover the saturating and noninstant nonlinear response [18, 21], nonlinear loss, nonparaxiality, and manifestation of the non scalar nature of the electromagnetic radiation [22, 23, 24] are also capable to arrest collapse.

2.1.3 Self phase modulation

The nonlinear change of the refractive index could be induced not only in transverse space by beam intensity distribution, but also become time-dependant due to wave amplitude temporal modulation. Namely, pulse generates temporal phase-shift during propagation in nonlinear material. This phenomena is called Self Phase Modulation (SPM). It could be understood by studying simple equation, which accounts only phase change due to nonlinear refractive index during wave propagation in medium:

$$\frac{\partial A}{\partial z} = i\beta|A|^2 A. \tag{2.13}$$

The solution of the equation 2.13 is

$$A\left(t,z\right) = A_0(t)\exp\left(-i\beta|A_0|^2 z\right). \tag{2.14}$$

For the wave amplitude and phase we obtain:

$$\begin{aligned} a(t,z) &= a_0(t,z), \\ \varphi(t,z) &= \varphi_0(t) - \beta|A_0(t)|^2 z. \end{aligned} \tag{2.15}$$

Obviously the amplitude does not change in propagation, but the phase acquires time-dependant phase-shift proportional to the pulse intensity and propa-

gation distance. The accumulated phase-shift reads as

$$\delta\varphi(t,z) = -\beta z|A(t)|^2 = -z\frac{\omega_0}{c}n_2^{(I)}I_0(t). \tag{2.16}$$

The frequency shift induced by SPM reads as

$$\delta\omega(t,z) = \frac{\partial(\delta\varphi)}{\partial t} = -\beta z\frac{\partial|A_0(t)|^2}{\partial t} = -\frac{\omega_0 z}{c}n_2^{(I)}\frac{\partial I_0(t)}{\partial t}. \tag{2.17}$$

Since the intensity of the propagating pulse remains constant, the SPM steadily generates new frequency components and broadens the pulse spectrum. Lets discuss the effect of the SPM to the Gaussian pulse propagation through nonlinear medium. We introduce maximum phase shift as

$$\varphi_{max} = \frac{\omega_0 z}{c}n_2^{(I)}I_0(0), \tag{2.18}$$

and nonlinear SPM length L_{spm} by condition $\varphi_{max} = 1$, thus

$$L_{spm} = \frac{c}{\omega_0 n_2^{(I)}I_0(0)}. \tag{2.19}$$

The phase and frequency change for a Gaussian pulse $I_0(t) = I_0(0)\exp(-t^2/\tau_0^2)$ are

$$\begin{aligned}\delta\varphi(t) &= -\varphi_{max}\exp\left(-\frac{t^2}{\tau_0^2}\right),\\ \delta\omega(t) &= \frac{2}{\tau_0^2}t\varphi_{max}\exp\left(-\frac{t^2}{\tau_0^2}\right).\end{aligned} \tag{2.20}$$

The dependencies 2.20 are depicted in Fig. 2.1. As it seen the pulse acquires negative chirp mostly linear in vicinity of the pulse peak, and some positive chirp in the periphery (Fig. 2.1c). Furthermore, there are two time-moments (τ_1 and τ_2) when the two equal frequency shifts occurs (obviously except the central frequency). Due to the fact that these frequency components correspond to the distinct time moments, and do not have the same phase, therefore, they should

interfere in frequency domain: the pulse spectrum consists of number of interference fringes (see Fig. 2.2). The number of peaks is equal to integer part of ϕ_{max}/π. From equation 2.20 and extremum condition $\frac{d}{dt}\delta\omega(t) = 0$ we find time moments when frequency shift reaches maximum and minimum values: $t_{min} = -\tau_0\sqrt{2}$ and $t_{max} = \tau_0\sqrt{2}$. Thus the maximum frequency shift is $\delta\omega_{max} = \sqrt{\frac{2}{e}}\frac{\varphi_{max}}{\tau_0}$.

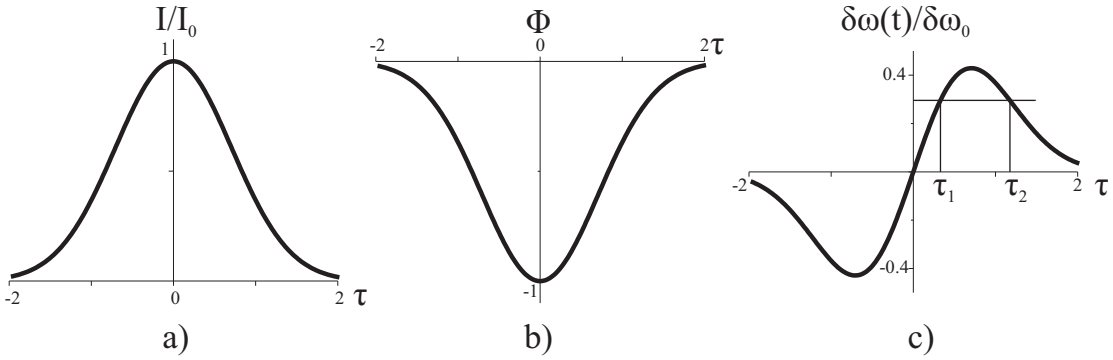

Figure 2.1: The Gaussian shape (a), the reduced phase $\Phi = \varphi/\varphi_{max}$ (b), and reduced frequency deviation (c), where $\delta\omega_0 = 2\varphi_{max}/\tau_0$.

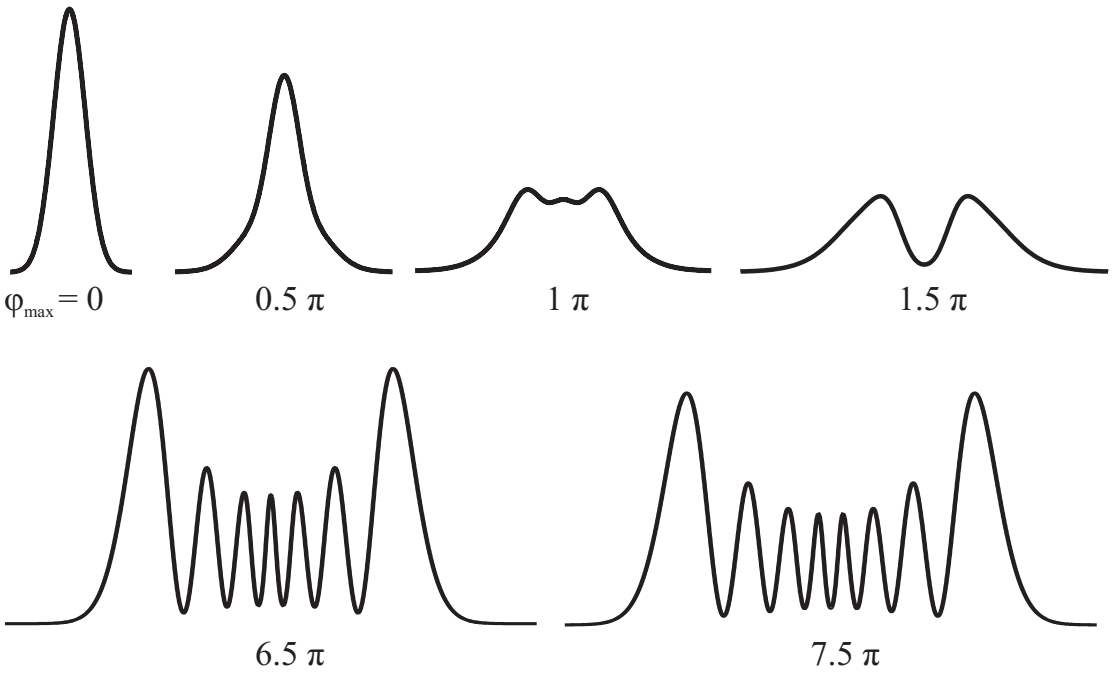

Figure 2.2: Spectrum of the Gaussian pulse at different ϕ_{max} values.

Presented above explanation of SPM was derived without the accounting of the material dispersion. That is true, either the pulse is very long or the dispersion is negligible. The interesting case (in future we use it to explain pulse splitting in normal Group Velocity (GV) dispersion region) of pulse propagation in non-

linear $\chi^{(3)}$ material with normal GVD is reshaping to flattop pulse. The required conditions for such reshaping are: self phase modulation length L_{spm} must be much shorter than material length ($L_{spm} << L$), and dispersion length would be larger than length of the material, namely, ($L_{spm} \ll L \approx \sqrt{L_{spm}L_d} < L_d$). The dynamics of the simultaneous action of the material dispersion and SPM is determined by length of self-action defined as $L_{sa} = \sqrt{L_{spm}L_d}$. The result of the combined action is formation of nearly flattop pulse with linear chirp at the distance $z \sim 2L_{sa}$. As it is depicted in Fig. 2.3 in the initial part of the propagation SPM is dominant process. Linear chirp produced by normal GVD has the same sign as the chirp produced by SPM in central part of the pulse ($t \approx 0$). Therefore, the central part of the pulse undergoes stretching, however the peripherical part what possesses the opposite chirp induced by SPM, undergo temporal compression. Finally combined action of stretching of the central part and compression of peripherical one, reshapes Gaussian pulse into flattop.

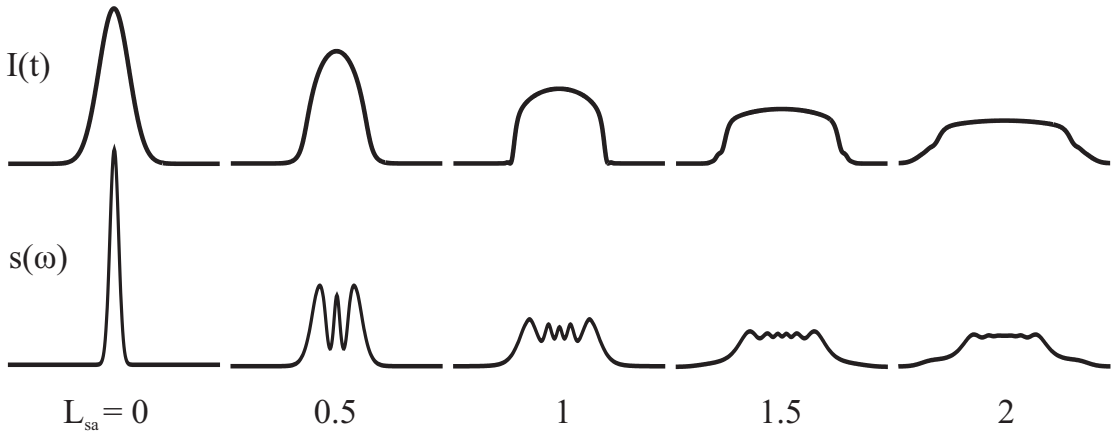

Figure 2.3: Flattop pulses formation in nonlinear dispersive $\chi^{(3)}$ material. Pulse intensity top line and spectrum bottom line evolution.

A completely different scenario of the SPM takes place in anomalous dispersion region and positive n_2. In this case, the chirp induced by SPM (positive) and chirp obtained due to GVD (negative) have opposite signs, and starts to compensate each other. That happens when self-action length L_{sa} becomes equal to dispersion length L_d. The pulse formed under such condition is capable stationary propagate without any distortions of the envelope *i. e.* we obtain single soliton pulse. The

soliton solution could be presented in form

$$A(z,t) = A_s \exp(-i\Gamma z). \tag{2.21}$$

Substituting Eq. 2.21 into Nonlinear Schrödinger (NLS) equation

$$\frac{\partial A}{\partial z} - \frac{i}{2} g_0 \frac{\partial^2 A}{\partial t^2} = i\beta |A|^2 A, \tag{2.22}$$

we obtain

$$\frac{1}{2} g_0 \frac{\partial^2 A_s}{\partial t^2} + \Gamma A_s + \beta A_s^3 = 0. \tag{2.23}$$

This equation can be rewritten in a form

$$\frac{1}{2} g_0 \left(\frac{\partial A_s}{\partial t} \right)^2 + \Gamma A_s^2 + \frac{1}{2} \beta A_s^4 = 0. \tag{2.24}$$

The solution of this equation when $\beta > 0$ (self-focusing nonlinearity) and $g_0 < 0$ (anomalous GVD) is

$$A_s(t) = A_0 sech(t/\tau_s), \tag{2.25}$$

where soliton amplitude A_0 and duration τ_s satisfies the relation

$$2\Gamma = \frac{|g_0|}{\tau_s^2} = \beta A_0^2. \tag{2.26}$$

According to (2.26), the soliton with the higher amplitude has shorter duration. When the hyperbolic secant pulse has peak power equal to critical $P = P_{cr}$ ($P_{cr} = \frac{g_0 A_{eff}}{\tau_s^2 \beta}$, where A_{eff} is effective area, and not the same as P_c), such pulse propagates stationary in a fiber with the anomalous dispersion. The pulse propagation dynamics may be presented by three different scenario. The first, when $P < P_{cr}$ the nonlinearity does not able to compensate material dispersion, therefore pulse is dispersively broadening (Fig. 2.4 a). In second case when $P = P_{cr}$, SPM fully compensates the phase modulation produced by GVD, propagation be-

comes stationary (Fig. 2.4 b). In the third case, when $P > P_{cr}$, the SPM is dominating at the initial stage (thanks to high intensity) and spectrum is broadening. Due to anomalous GVD such pulse starts to compress till some minimum value, when GVD (proportional to $1/\tau_s^2$, where τ_s is pulse duration) becomes capable to overcome pulse compression, and pulse starts to spread. Such compression-decompression cycles are periodic (Fig. 2.4 c). This oscillating pulse behavior become very complex when the peak power significantly exceeds the critical power. The multiple soliton bound states occur. The integer part of $N = P/P_{cr}$ ratio gives the N'th soliton bound state number.

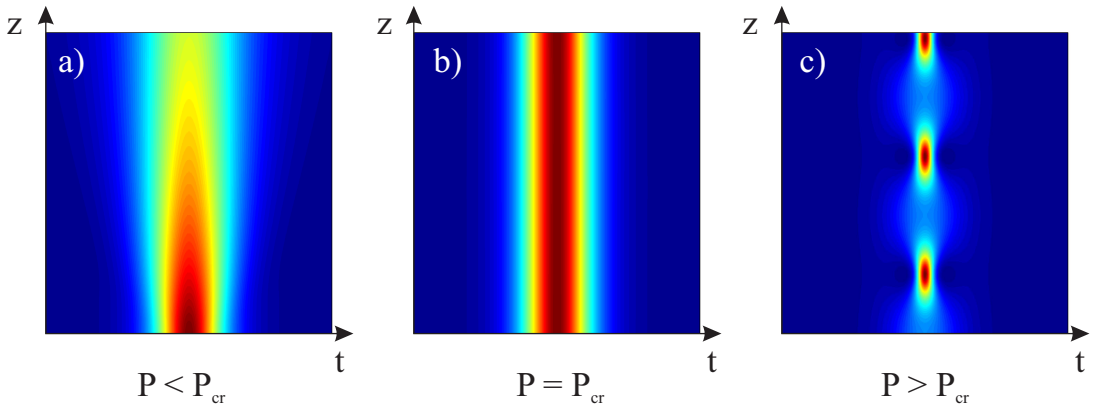

Figure 2.4: Pulse envelope change when pulse peak power is lower than critical a), when peak power equals to critical power, soliton propagation case b), and peak power is more than critical power c) in this particular case $P = 2P_{cr}$.

2.1.4 Modulation instability and skewed coherence

The modulation instability driven noise amplification may manifest itself as generation of high intensity peaks with random spatio-temporal positions, and could initiate the process known as multifilamentation formation process. The nature of the modulation instability can be explained by FWM process. The optical pulse propagating in nonlinear $\chi^{(3)}$ medium experiences not only SPM, but also FWM process. Conversely as the SPM, that is always phase-matched, the FWM process requires a phase matching of the interacting waves *i.e.* the condition $\overrightarrow{k}_s + \overrightarrow{k}_i - 2\overrightarrow{k}_p = 0$ must be satisfied. There the $\overrightarrow{k}_p$, $\overrightarrow{k}_s$, $\overrightarrow{k}_i$ are the wave vectors of the pump, signal and idler wave, respectively. We will assume

that pumps are plane monochromatic wave directed along some axis, but signal and idler waves are matched non-collinearly (Fig. 2.5).

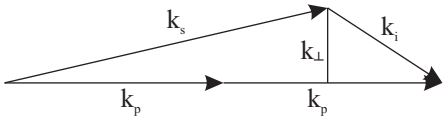

Figure 2.5: Noncollinear FWM phase match scheme.

In such case we have

$$k_{s\perp} = k_{i\perp} = k_\perp, \tag{2.27}$$

and

$$k_{sz} + k_{iz} - 2k_p = 0. \tag{2.28}$$

The longitudinal wave-vector is defined as $k_z = \sqrt{k^2 - k_\perp^2}$. However in paraxial approximation $k_z = k - \frac{k_\perp^2}{2k}$. We will account material dispersion just till second order, thus we have $k(\omega_0 + \Omega) = k_0 + k'\Omega + \frac{1}{2}k''\Omega^2$, where $k_0 = k(\omega_0)$, and $\omega = \omega_0 + \Omega$. For the plane and monochromatic pump we have $k_p = k_0 \equiv k(\omega_p)$. The frequency of the signal wave component ($\omega_s = \omega_0 + \Omega$), and frequency of the idler wave ($\omega_i = \omega_0 - \Omega$) are coupled by condition $\omega_s + \omega_i = 2\omega_p$. Thus from phase matching condition we obtain

$$k_s(\omega_0 + \Omega) + k_i(\omega_0 - \Omega) - 2k_0 = \frac{k_\perp^2}{2k_0}. \tag{2.29}$$

The condition 2.29 within approximation of the material dispersion till second order reads as:

$$k_\perp = \sqrt{k_0 k''\Omega}. \tag{2.30}$$

This condition is equal to the angular dispersion of the X pulse *i. e.* the FWM supports the X pulse generation in $\chi^{(3)}$ material. However, discussed above phase matching condition was obtained in so-called "cold" regime, when the SPM

and Cross Phase Modulation (XPM) induced change of refractive index was not accounted. The phase matching in paraxial limit with accounted SPM and XPM could be obtained from Eq. 2.29. We should account the SPM for pump wave by adding extra term to the wave number: $k_p = k_0 + n_2 I\frac{\omega_0}{c}$. Similarly the XPM for the signal and idler waves could be introduced as $k_s = k_0 + k'\Omega + \frac{1}{2}k''\Omega^2 + 2n_2 I\frac{\omega_0}{c}$ and $k_i = k_0 - k'\Omega + \frac{1}{2}k''\Omega^2 + 2n_2 I\frac{\omega_0}{c}$. Finally from Eq. 2.29 we have

$$k_\perp = \sqrt{(k_0 + n_2 I\frac{\omega_0}{c})(k''\Omega^2 + 2n_2 I\frac{\omega_0}{c})}. \tag{2.31}$$

The corrected phase matching expression corresponds to the three cases. The first is "X" shaped and characterized by gap in spatial frequencies (Fig. 2.6 a), the second one is also "X" shaped and characterized by gap in temporal frequency domain (Fig. 2.6 e), and the third is "O" shaped (Fig. 2.6 i).

Such phase matching conditions sustain generation of some spatiotemporal patterns and could be characterized by skewed coherence property. The similar skewed coherency was found in $\chi^{(2)}$ materials [25, 26]. To retrieve the spatiotemporal intensity distribution of the patterns discussed above, we removed pump spectrum, leaving just the FWM generated components. The analysis of the spatiotemporal correlation function revealed the hidden coherence (Fig. 2.6)

Multifilamentation in nonlinear medium was studied numerically solving the NLS equation. The same model was used and explained in ref. [27]. The numerical simulation results corresponding to the three different cases are summarized in Fig. 2.6. It reveald the skewed coherence appearance in spectrum and intensity domains. The first row represents the appearance of the skewed coherence in self-focusing nonlinear material with normal GVD. Such case correspond to the angular dispersion support presented in (Fig. 2.6 a) and is consistent with the results of numerical experiment, (Fig. 2.6 b-d) *i. e.* distribution of the spectral components in the far field renders the phase matching induced angular dispersion (Fig. 2.6 a). The near field (Fig. 2.6 c) was retrieved by filtering of the pump

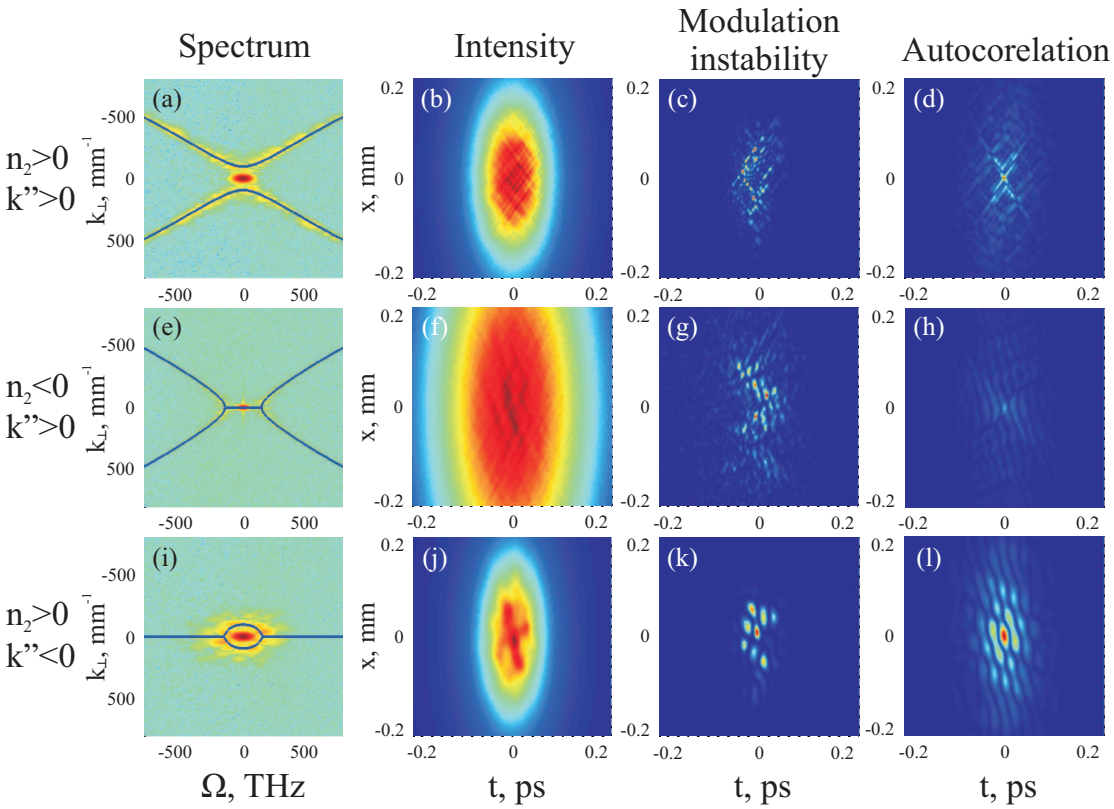

Figure 2.6: Skewed coherence types in $\chi^{(3)}$ medium. First row represents self-focusing, normal dispersion case; where first figure is a spatiotemporal spectrum, and solid lines represents analytically estimated FWM phase matching condition, second is spatiotemporal intensity profile, third is skewed coherence developed intensity distribution, fourth is a single shot autocorrelation. Second row represents self-defocusing, normal dispersion case. Third row represents self-focusing in anomalous dispersion region.

field (in spectrum domain). The autocorrelation patterns were retrieved by use of Wiener-Kintchine theorem. Both the autocorrelation and near field reveals the X-shaped coherence. Autocorrelation result is grainy because one pulse can constitute only a portion of statistical ensemble while integrating autocorrelations over many shots granularity will get smoothed [26].

The second row in Fig. 2.6 corresponds to the self-defocusing medium with normal GVD case. The near, far field, and autocorrelation patterns are X - structured.

The third row corresponds to the self-focusing case with anomalous GVD. The angular dispersion line corresponding to the phase matching condition, is ”O” shaped. The near field do not show clear shape of O-wave, but far field and autocorrelation (Fig. 2.6 i, l) reveal typical O-coherence: all peaks are placed

around pump component.

As it was shown, the skewed coherence is a freak state, where light package does not have temporal or spatial coherence, but it is skewed crosswise. Traditional methods like Michelson interferometer and Young interferometer performs correlation measurements just in time, or just in space and are not capable to show skewed coherence: the volume of coherence found by such traditional methods seems infinite small.

Generation of the object possessing skewed coherence requires high energy distributed over large spatiotemporal area or, in other words, large energy reservoir. It is possible to enhance skewed coherence object formation on one axis and suppress on another just by changing from radial Gaussian beam to elliptic. In limit condition when semi-minor elliptical beam diameter approaches the diameter of the filament and is much less than in perpendicular semi-major axis, the skewed coherence objects occurs on semi-major ellipse axis and time, and almost extinct on other space-time dimension. Another limiting condition is peam power. When it exceeds few critical powers ($P_{cr} = 3.77\frac{\lambda^2}{8\pi n n_2}$, where λ is wavelength, n is refractive index, n_2 is nonlinear refractive index), FWM is inefficient, and almost extinct, therefore beam experiences self-focusing, reshapes to Townes profile, and later forms a single filament. However, more powerful wave-packet ($P \gg P_{cr}$) experiences modulation instability, develops stationary modes, and finally, evolves into number of filaments. The position of each filament depends on intensity peaks developed by modulation instability. Note, that FWM phase matching curve do not approaches the spectrum of the stationary mode (X-wave), defined by transverse k-vector: $k_\perp = \sqrt{k^2(\omega) - k_z^2(\omega)}$, where $k(\omega) = \frac{n(\omega)\omega}{c}$ is the wavenumber, and $k_z(\omega) = k(\omega_p) - \beta + \left(\frac{\partial k}{\partial \omega}|_{\omega_p} - \alpha\right)(\omega - \omega_p)$. Here ω_p is the carrier frequency of wave packet (pump), α and β are free parameters.

The modulation instability driven skewed coherence spectrum deviation from stationary mode (X-wave) condition is presented in Fig. 2.7. The modulation instability spectrum generated via FWM process is symmetric and corresponds

(with good accuracy) to the phase matching curve (white dotted line in Fig. 2.7). However, the stationary propagation requires nonsymmetric angular dispersion depicted by red dashed line Fig. 2.7. Since the phase matching condition and the modulation instability pattern spectra could be (at least vicinity of the pump) approximated by intersection of two straight lines (green lines) the near field (Fig. 2.7 b) also exhibits the multiple superposition of the spatio-temporal patterns distributed at appropriate angle.

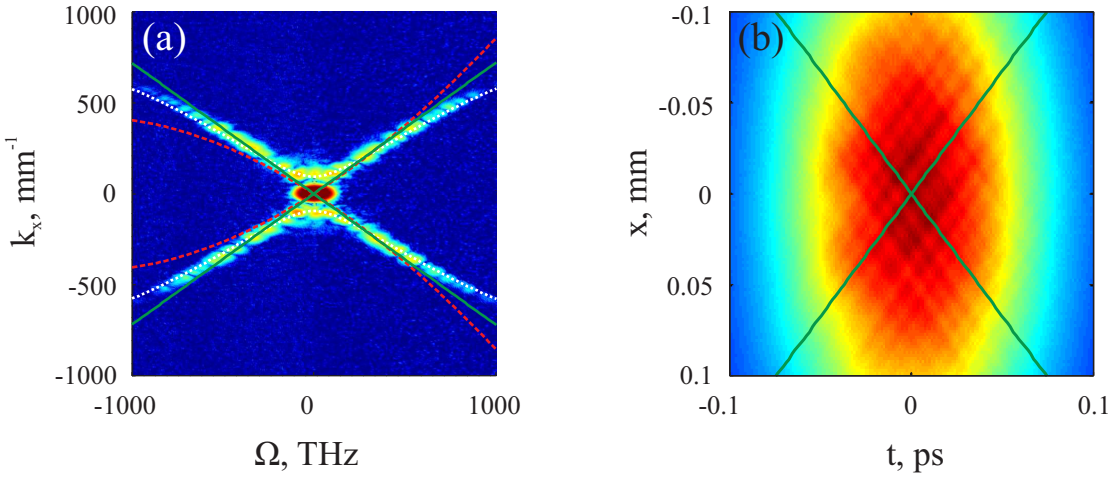

Figure 2.7: The far (a) and near (b) field intensity distribution of the modulation instability driven patterns. White dotted line depicts the modulation instability induced FWM phase matching, red-striped line shows the angular dispersion of stationary mode. The green crossed lines shows the slope of the tilted spatio-temporal patterns in near field. Normal GVD case was considered.

The similar comparison between multifilament spectra and stationary X wave angular dispersion curve is presented in Fig. 2.8. The red-dashed line corresponds to the X wave propagating with group and phase velocity (parameters $\alpha = 0$ and $\beta = 0$) equal to that of the pump [28]. The pulse-splitting [29] initiates a formation of the X waves propagating with different group velocities [30]. However, each of these X waves are characterized by its own central frequency and, thus the generated filament spectra vicinity the pump ($\Omega = 0, k_\perp = 0$) central component significantly differs from the stationary X wave condition described by red-dashed line. Despite that, in the periphery the filament spectra approaches the stationary mode condition. The total spectrum becomes blurred due to subsequent pulse splitting events: formed X waves patters have different velocities and

spatio-temporal positions. Simulations were performed for fused silica with the incident beam diameters $610\mu m$ and $90\mu m$ and $250fs$ duration at Full Width Half Maximum (FWHM), central wavelength was $800nm$. The properties for the fused silica were taken from [27]. The intermediate state between skewed coherence and stationary mode are wavy fringes in near field, and are called "snake" or "worm" instability.

The skewed coherence in $\chi^{(2)}$ material was studied earlier by Picozzi *et al.* [31, 25, 26]. The material discussed in current subchapter is necessary for the explanation of different multifilamentation stages in Chapter 5.

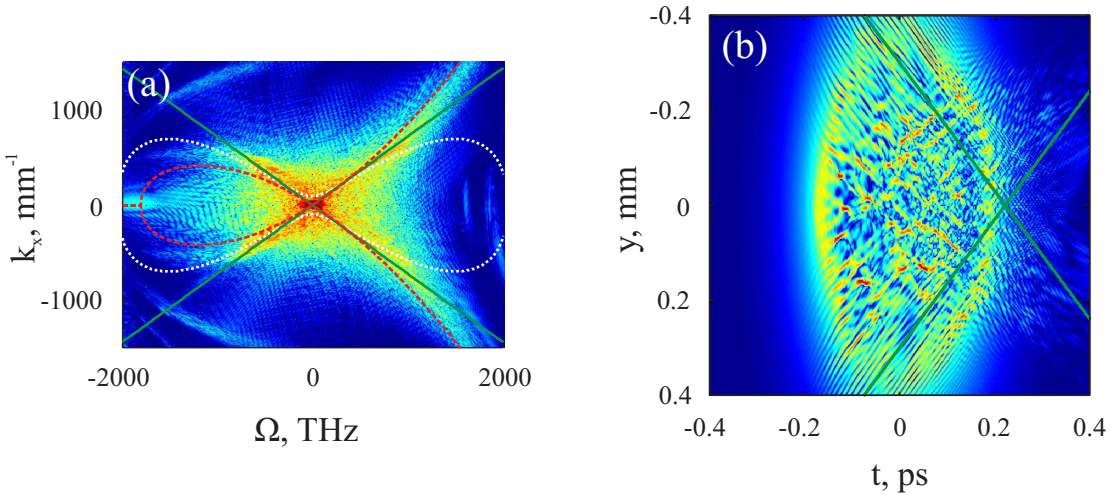

Figure 2.8: The multifilamentation far (a) and near (b) field intensity distribution in normal GVD and self-focusing ($n_2 > 0$) case. White dotted line depicts the modulation instability induced FWM phase matching, red-striped line shows the angular dispersion of stationary mode. The green crossed lines shows the slope of the tilted spatio-temporal patterns in near field.

2.1.5 Pulse splitting

The intense pulse propagating in nonlinear medium with normal GVD undergoes pulse-splitting [29]. The pulse-splitting is one of the most important phenomenon preventing wave packet collapse during filamentation process, it can be explained by GVD. Indeed, it was demonstrated [29], that GVD can arrest the collapse, however it is valid just in certain power range [32]. As it is known, the self-focusing in normal GVD case leads to flat-top pulse formation. Thus if the self-focusing sustains beam shrinking, the normal GVD, on contrary, leads to the pulse broadening during propagation. Since the pulse temporal broadening is

one-dimensional effect but beam shrinking due to self-focusing takes place in two dimensional space the temporal pulse peak intensity keeps growing, and pulse becomes shorter in time despite the continuous energy flux from the pulse peak to the periphery (caused by normal GVD). Due to such dynamics (Fig. 2.9) the power in the central part of the pulse ($t \approx 0$) becomes less than critical ($P(t = 0) < P_{cr}$) and self-focusing under the pulse peak becomes impossible. However, in the periphery part of the pulse (Fig. 2.9), beam power (due to energy brought by GVD) becomes higher than critical ($P > P_{cr}$). Thus the self-focusing starts formation of two intense peaks, or in other words, makes pulse-splitting (Fig. 2.9 g). Two pulses produced by such event have slightly different group velocities respect to initial pulse.

Such arrest of the collapse is possible only within distinct power range, higher power pulse will collapse due to insufficient dispersion, while lower power beams may have too small nonlinear effect. The range of power where dispersion is able to arrest collapse was estimated analytically and studied numerically by Luther *et al.* [32]. It was demonstrated, that the blow-up power depends nonlinearly on GVD.

It is worth to note, that pulse collapse could be arrested not only by GVD, but also plasma generated during filamentation process [33]. Plasma sustains the defocusing of the trailing part of the pulse and shifts the remaining, truncated part of the pulse to the leading part, which still keeps to self-focus. Such dynamics causes the pulse superluminal propagation. The collapse becomes impossible because of the balance between self-focusing and plasma induced defocusing. The plasma induced defocusing is non dissipative, however the nonlinear losses induced by MPA also are among the effects capable to prevent collapse: the most intense part of the pulse dissipates and becomes limited at some intensity level. The nonlinear losses sustain formation of flat-top pulse with the subsequent pulse-splitting (also induced by MPA) [33]. All mentioned above (Chapter 2) effects must be included in numerical code, in order to get simulation results compatible with the

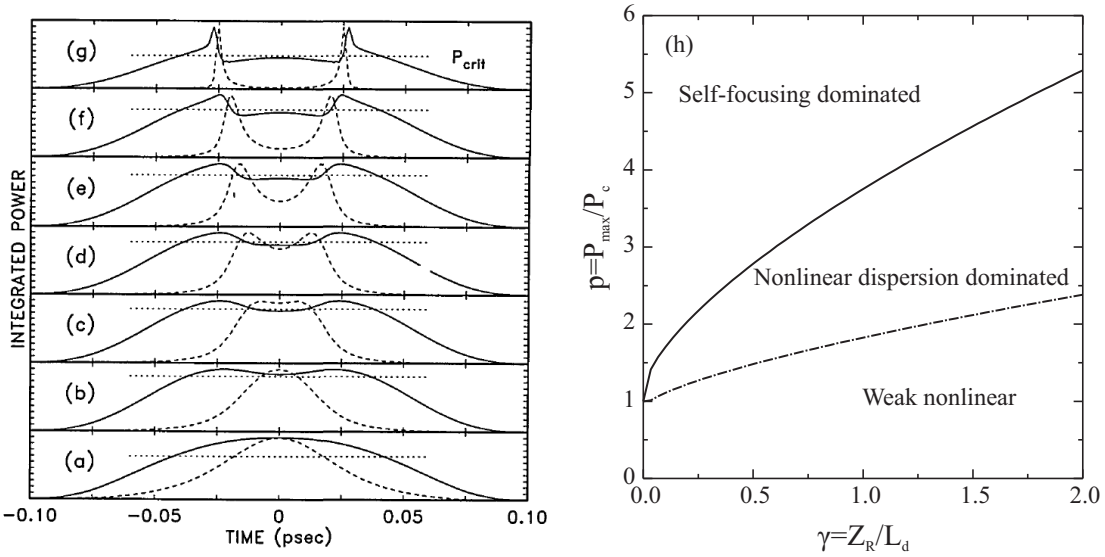

Figure 2.9: The pulse-splitting dynamics (a)-(g) explained by pulse on axis intensity profile (dash) and instantaneous power (solid line) evolution. The dotted line depicts the critical power. [29]. (h) The self-splitting power range dependence on material parameter γ. $\gamma = Z_R/L_d$ is relative material dispersion strength over the diffraction. Where Z_R and L_d are Rayleigh and dispersion length respectively, P_{max} is the peak input power of Gaussian pulse. Self-splitting power restricted by two curves. Pulse having lower power when dash-dotted curve will not split, however pulse having higher power than solid curve will undergo collapse. [32]

experiment. Just in very few cases, when the radiation temporal spectrum remains narrow and limited, or when we are interested in time-integrated output the temporal effects could be excluded.

2.1.6 Higher order Kerr nonlinearities

Since discovery of the filamentation in gasses [2], it has been described as the interplay between the Kerr self-focusing and free electron plasma defocusing. Recently that paradigm was revised not only by X wave theory (see section 2.3.4), but also by a suggestion, that Higher Order Kerr Nonlinearity (HOKN) is able to saturate and even change the sign of the Kerr effect [34]. The investigation sparkled from the measurement of higher order HOKN in atomic and molecular gasses [34, 35]. It was shown, that refractive index dependence on intensity is not linear but more complex: negative nonlinear refractive index could be achieved at very high intensity. It was claimed that such phenomenon could occur even before the significant contribution of free electric charges. Statements were quickly adopted to numerical filament generation analysis [36]. Authors claim, that plasma contri-

bution could be replaced by HOKN, and plasma contribution is not so important as it was supposed. A number of papers were published, some of them were supporting [37, 38, 39, 40, 41], some were rejecting [42, 43, 44, 45] the importance of the HOKN. Here we present some details of this contraposition.

Loriot *et al.* used polarization pump and probe technique for measuring high order Kerr refractive index. Recently single-shot supercontinuum spectral interferometry measurement technique was adopted for direct measurement of the nonlinear optical response in argon and nitrogen [45]. Results were contradicting with the Loriot [34] statement. No any deviation from linear dependence on the intensity till the point where the response abruptly turns to negative values due to plasma defocusing was found.

The ultrashort pulse filamentation numerical study by Bejot *et al.* [36] revealed, that it is possible to include HOKN contribution in numerical calculations, do not account plasma generation and get the almost correct results. Polynkin *et al.* [43] experimentally measured plasma density generated through filamentation in air and argon. It was found, that significant amount of free electrons were generated via multiphoton ionization on beam axis. The Kosareva's group made comparison of experimentally measured filament intensity with results from 2 numerical models: the first one with HOKN and second without HOKN but with plasma account as the major effect in beam defocusing [44]. It was demonstrated, that the HOKN model does not reproduce intensity evolution, and in some cases, may lead to incorrect result. When collapse is arrested by plasma, the blue shifted component has X-shaped angular spectrum, what is consisted with experiments. While the collapse is arrested by HOKN, the far field becomes O-shaped, without blue-shifted component.

The dynamics of higher harmonic generation with and without HOKN effect, is different [37]. Therefore, the experiment to measure and compare the relative power of third and fifth harmonic, was proposed [42]. When just the third order nonlinearity is accounted, the ratio between intensities of 5-th and 3-rd harmonics

$\eta = \frac{I_5}{I_3}$ is about 10^{-4}. However when the HOKN terms are accounted it becomes: $\eta \sim 10$. Till now no experimental verification was performed. The Brown *et al.* studied [46] the relative roles of the HOKN effect and ionization in gases. The 1D atomic model with the electron in attractive delta-potential that approximates the electron-ion Coulomb potential, was implemented. The obtained results are consistent with [42]. It was concluded, that supercontinuum generation is almost not effected by higher order Kerr nonlinearity, however harmonic continuum generation is, since the harmonics continuum is generated in short media using very tight focusing, and very high intensities, therefore, the filament and supercontinuum build up not possible. Volkova *et al.* [47] performed 3D quantum simulations of silver atom and also came to conclusion that the HOKN does not show significant influence.

2.2 Early numerical simulations of pulse propagation in $\chi^{(3)}$ media

The numerical simulation of the intense short light pulse propagation in nonlinear $\chi^{(3)}$ material were began since the aurora of the nonlinear optics. A simple model based on (3+1)-dimensional NLS equation was introduced [16] as early as 1975. The progress in stable ultrashort pulse laser [48], sophisticated measuring techniques, development of new equipment and computers progress provided opportunity to compare numerical findings with experimental data [29, 49]. The first experimental confirmation of pulse-splitting was given by Ranka and colleagues [49] in 1996. The simple NLS model predicts symmetric pulse-splitting. Indeed, the experimental data provided by most popular temporal autocorrelation technique confirmed the pulse-splitting symmetry. However, the autocorrelation technique always gives symmetric results, but more sophisticated Frequency-Resolved Optic Gating (FROG) technique revealed the nonsymmetry of pulse-splitting [50]. Later, nonsymmetric pulse-splitting was also observed with cross-correlation [51] technique. In order to explain the nonsymmetric pulse-splitting the numerical

model should include additional effects, such as, MPA, space-time focusing (non-paraxial propagation), Raman nonlinearity, nonlinear shock, plasma generation [52, 53, 54, 55, 56, 57, 58, 17]. As the model step by step gained additional physical effects the understanding about filamentation and supercontinuum generation iteratively evolved.

2.3 Filamentation models

2.3.1 The self-guiding model

The first explanation of long non diffractive propagation of the beam rested on the idea that Townes intensity profile is a stationary state of NLS equation [3]. Townes profile indeed meets conditions when self-focusing is compensated by diffraction and it is similar to Gaussian [59]. Therefore, a spontaneous reshaping should take place in nonlinear beam propagation, and indeed, it was demonstrated experimentally that elliptical beam can reshape into radially-symmetric Townes profile beam [60]. The Townes profile corresponds to the beam which power is equal to the critical power of self-focusing. That contradicts to the experimental data, where a filament can exceed the critical power [61]. Furthermore, the Townes profile represents unstable solution, where the only diffraction is compensated by self-focusing, excluding other physical processes. Therefore, it implies that solution is very sensitive to nonparaxiality, dispersion and other higher order effects which are present in experiment and affects output results. The study of instability of the Townes profile in nonlinear, self-guiding regime revealed, that spatio-temporal modulation instability in Kerr medium lead to the Y-wave generation [62].

2.3.2 The moving focus model

The distinct model of filamentation is called "moving focus". It is based on the assumption, that pulse can be split into temporal slices, and different slice should collapse at different distances [4]. The most intense part of the pulse will collapse at shortest distance and determine the nonlinear focus. The less intense parts

of the pulse will focus at longer distances. That explains how the moving focus is capable to maintain almost constant intensity and diameter in propagation. Such model was used, for the first time, to explain filamentation in air and was quite promising [63]. However, the moving focus model has obvious draw back, because it lay on the assumption, that individual slices are not coupled in any way, thus GVD, plasma and other effects should be weak. The model also fails, when the beam is initially passed through the lens, or has a phase modulation: as it will change the nonlinear focusing distance. However, this model predicts that pulse should split during the propagation through the nonlinear medium into two pulses: one with super-luminal and other with luminal group velocity [64]. Also the pulse temporal compression before the nonlinear focus was foreseen, as it was not done in self-guiding model.

2.3.3 Dynamical spatial replenishment

One of most successful explanation of filamentation, is called dynamical spatial replenishment [5, 6]. This model based only on spatial effects: induced self-focusing and plasma generation, and it very simplifies the filamentation process. The beam, with the power larger than critical undergoes self-focusing. Intensities near nonlinear focus approaches values needed for MPA and plasma generation. The generated plasma is characterized by $n_2 < 0$, and sustain the beam defocusing. If defocused beam also affected by nonlinear losses still has sufficient power to self-focus, it may undergo second focusing-defocusing cycle. Obviously, such beam has less power and the focusing-defocusing period gets elongated. The repetition of such cycles may explain filaments long range propagation property, but only for very high energy beams.

2.3.4 The conical X wave model

The discussed above filamentation models does not explain generation of the filament specific far field. The modern approach is based on X wave formation and has advantages compared with other models. The idea behind the "X wave" model

is, that filament is nothing, than few X waves spontaneously generated during interaction of conical wave packets. The conical nature of X waves sustains the intense central peak propagation without diffraction and dispersion. It also can explain suppression of nonlinear losses, treating the central peak as an interference result, when the energy is dynamically refilled from the not so intense background. The angular dispersion needed for non-diffracting and non-dispersive propagation can be expressed via transverse wave vector

$$k_\perp = \sqrt{k^2 - k_z^2}, \tag{2.32}$$

where the longitudinal wave-vector is a linear function of frequency $k_z = k_0 - k_0'\Omega$. The far and near field of X wave in normal dispersion regime is X-shaped, therefore they are called an "X waves". The nonlinear X-wave formation, for first time was demonstrated in $\chi^{(2)}$ material [65]. The recent paper of G. Valiulis *et al.* [66] examines the X wave formation in second harmonic generation. The conical nature of the filament was demonstrated in beautiful experiment of Dubietis *et al.*. In order to verify the guiding mechanism a filament was formed in water from an input Gaussian beam focused in cuvette. At the point where the filament appears they placed a pin-hole so that only the central spike of the filament passes through. That caused the abrupt death of the filament and strong diffraction of transmitted peak. However, when a stopper was placed in the path of the filament so that all beam passed except just the central spike, then the spike was reformed nearly immediately. This finding was explained by conical nature of the filament: the energy is continuously flowing from the surrounding energy reservoir toward to the central spike. When the spike is removed by stopper the refiling mechanism recreated it, but when the reservoir was removed by the pin-hole, then the tiny central spike disappeared due to strong diffraction. Mentioned above series of experiments [9, 10] revealed that the filament propagates without self-channeling mechanism, in contrast with the most popular opinion [2]. Later

Kolesik *et al.* [7] from numerical calculations gave the explanation that spectrum indeed reshapes into X waves after a pulse split. Numerical calculations demonstrated, that spectrum of two X waves generated during a single pulse-splitting event can be approximated by X wave condition 2.32. The angular dispersion, of the first closely fits to superluminaly propagating X wave, but the second one correspond to luminaly propagating X wave.

2.3.5 The effective three wave mixing model

One more closely followed filament distinct spectrum generation explanation is Effective Three Wave Mixing (ETWM) model [8]. The model is derived from unidirectional optical pulse propagation equation, and the idea behind the ETWM model is that distinct spectrum is generated due to scattering of the input field by nonlinear medium response. The three waves are: input field, nonlinear medium response and scattered field. Due to the pulse split in to two pulses the contribution to the generated spectrum should be accounted for both superluminaly and luminaly propagating pulses. Therefore the total nonlinear change in susceptibility $\Delta\chi$ is a sum of two peaks with different velocities:

$$\Delta\chi\left(x,y,t\right) \approx \sum_{r=1,2} \Delta\chi_r\left(x,y,t-z/v_r\right). \tag{2.33}$$

By decomposing response peaks into fourier spectrum components and inserting into unidirectional pulse propagation equation, the end result is:

$$A_{k_x,k_y,\omega}\left(z\right) = \frac{i\omega^2}{2c^2 k_z\left(\omega,k_x,k_y\right)} \times \int dz \sum_{r,u,v,\Omega} \Delta\chi^{(r)}_{k_x-u,k_y-v,\omega-\Omega}\left(z\right) A_{u,v,\Omega}\left(z\right) \times \exp\left[iz\left(-k_z\left(\omega,k_x,k_y\right)+k_z\left(\Omega,u,v\right)+\frac{\omega-\Omega}{v_r}\right)\right]. \tag{2.34}$$

The largest contribution to the scattered field gives the term which satisfies the phase matching condition. Therefore the scattered field is most efficient, when the

exponential term becomes constant (the argument of the exponent is equal 0). So, the spectral energy is concentrated in the region determined by

$$\left| -k_z\left(\omega, k_x, k_y\right) + k_z\left(\Omega, u, v\right) + \frac{\omega - \Omega}{v_r} \right| = 0. \tag{2.35}$$

This equation describes the phase matching condition for generation of scattered wave of frequency ω and transverse wave-numbers $k_{x,y}$ from scattering optical wave of frequency Ω with a material wave of $\omega - \Omega$ frequency. When the input wave is plane and monochromatic, the scattered wave phase matching condition is equal to X wave angular dispersion requirement (Eq. 2.32), which describes stationary propagating conical waves. These two explanations (X wave and ETWM) of filamentation spectra have similarities: they both state that filamentation in normal dispersion regime will spontaneously generate X waves. The difference comes in the origin of X waves, the ETWM model explain the origin of the X waves via linear scattering process, and do not gives explanation on filamentation dynamics, specifically what are group velocities of split pulses, The X wave model presumes the X waves are being generated due to material nonlinearity. Wave dynamics is explained as a relaxation toward the stationary mode. It should be noted that it is not derived from any mathematical means, but is postulated referencing numerical and experimental data. As an example of supercontinuum generation and its complexity, next chapter will discuss the difference in supercontinuum generated spectrum simply by changing initial beam diameter.

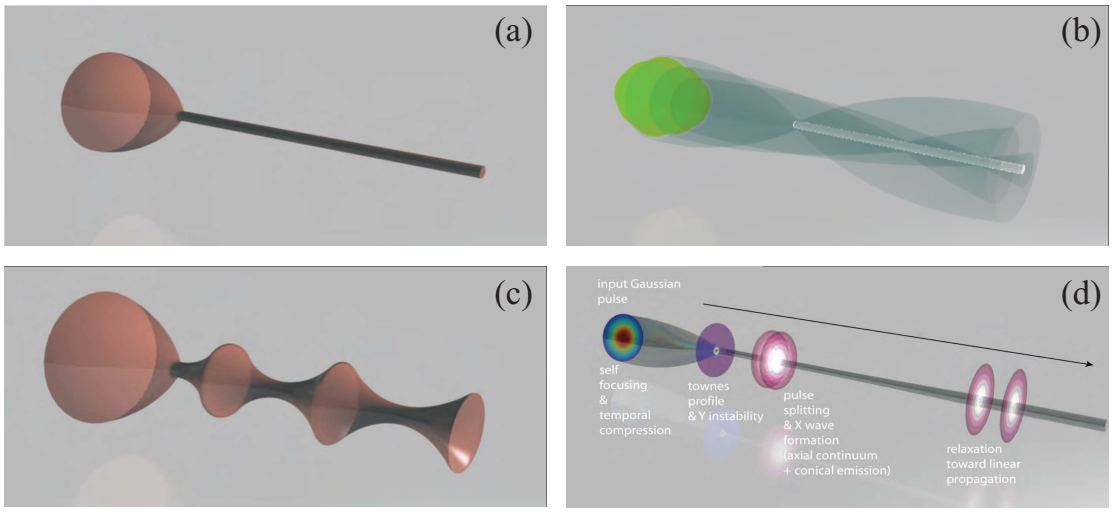

Figure 2.10: Comparison of four filamentation models: (a) self-guiding model, (b) moving focus model, (c) dynamical spatial replenishment and (d) conical X wave model.

Chapter 3

Supercontinuum spectra dependence on initial beam diameter

Supercontinuum generation is a key element for creation of modern tunable optical parametric generators. The super broad spectrum generated via tightly focusing initial beam is coherent and allows to compress produced pulses till extremely short duration. Supercontinuum generation associated physical effects are SPM, FWM, shock-front formation and others, common for all Kerr media. The generated supercontinuum spectrum has angular dispersion which is associated with X wave formation [30, 67]. The group and phase velocities of X wave can take any particular value. The larger GV difference from GV at central frequency leads to the wider supercontinuum spectra. The first analysis of generated supercontinuum spectra dependence on initial diameter was performed by Faccio *et al.* [68]. It was noticed that the change of sample position respect beam focuss (initial diameter and wave front change) changes the blue peak position, even if beam energy is fixed.

To investigate more deeply the dependence of the supercontinuum spectra on the initial beam size we carried out a series of numerical experiments with four different initial beam diameters of 6 μm, 12 μm, 24 μm and 48 μm. That corresponds to the 1.6 mm diameter FWHM Gaussian beam focussed by 5 cm, 10 cm, 20 cm, 40 cm focal length lenses. The 130 fs duration Gaussian pulses with central

wavelength of 800 nm was in all cases. In all cases the spectral broadening becomes visible at different input energy. The larger initial beam diameter requires the higher energy to initiate supercontinuum generation. The dependence of the intensity maximum reached by filament (it takes place at some distance, usually just before pulse splitting event) on the input energy is presented in Fig. 3.1. Note that, in all cases the calculated lines have extremums at some input energy values. Such limit intensity is known as a level of intensity clamping. When the input energy exceeds the corresponding value of the intensity clamping the maximum reachable intensity of the filament drops due to energy losses caused by MPA and plasma generation, also due to multiple pulse splittings or/and multifilamentation. The intersections of the calculated plots with the black horizontal line defines the energy values when the filament maximum intensity during propagation reaches 32 TW/cm^2 (at some propagation distance). As can be seen from Fig. 3.1 6 μm, 12 μm, 24 μm, 48 μm diameter beams reaches 32 TW/cm^2 maximal intensity when the input energy is 0.26 μJ, 0.282 μJ, 0.334 μJ and 0.466 μJ, respectively.

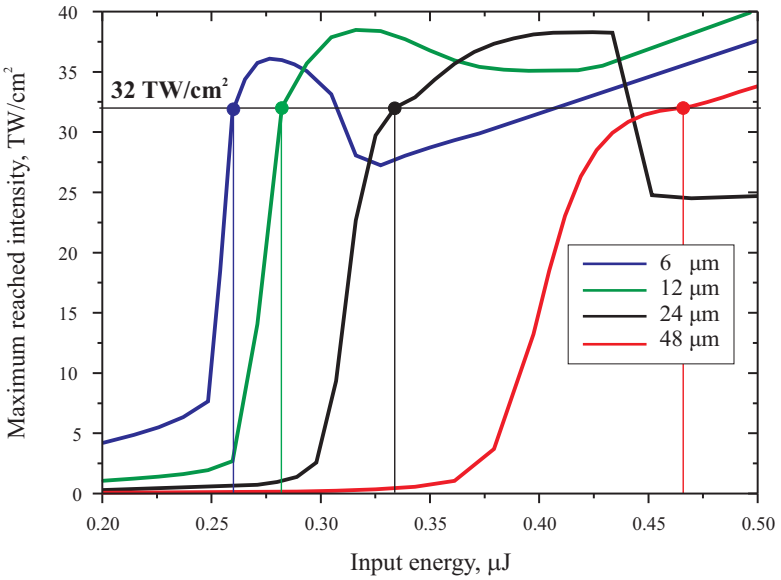

Figure 3.1: The filament maximum intensity value dependence on input energy in sapphire crystal for four different initial diameter 6 μm, 12 μm, 24 μm and 48 μm. Black horizontal line represents the value of $32 TW/cm^2$.

As it was mentioned the intense Gaussian pulse in Kerr medium undergo complex spatio-temporal focusing till the moment when GVD splits it to 2 pulses: one

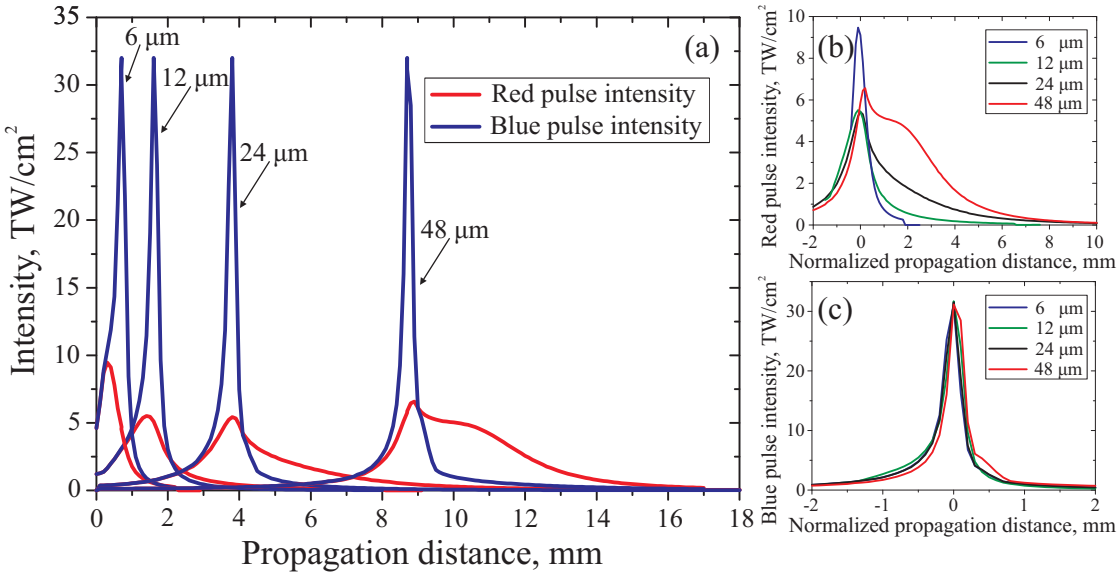

Figure 3.2: (a) "Blue" and "red" pulse intensity dynamics during propagation in nonlinear media, for four different input diameters (6 μm, 12 μm, 24 μm and 48 μm). The composition of the red (b) and blue (c) pulse intensity dynamics for different input diameters. Zero distance value correspond to the distance, when the blue pulse maximum intensity was reached.

is composed by red-shifted spectral components and propagates superluminaly, the second pulse is composed by blue-shifted spectral components and propagates luminaly *i. e.* with the group velocity nearly equal to the initial pulse. The intensities of the red and blue pulses have different dynamics during the propagation in nonlinear medium (see Fig. 3.2). It is evident, see Fig. 3.2a,c, that in all investigated cases (diameters 6 μm, 12 μm, 24 μm and 48 μm) the blue pulse reaches the same maximum intensity (32 TW/cm^2 in our case), but at different distances. However the red superluminal part have different maxima for different input beam size (Fig. 3.2a,b). The blue-shifted pulse intensity dynamics seems is not sensitive to the input beam diameter (Fig. 3.2 b), but the red part of the filament becomes sensitive on focusing conditions: the larger input beam sustains longer red pulse propagation with relatively high intensity (Fig. 3.2 c). Such high intensity pulse propagating in Kerr medium generates new frequency components via FWM process, accordingly to the phase matching conditions. The intensity dependant phase matching was calculated using relation between the group velocity and the pulse intensity, as it was described in [30]. The axial part of the filament is usually addressed to the broad band spectrum and is called

supercontinuum radiation. Obviously the axial radiation does not have angular dispersion. However, off-axis radiation posses some angular dispersion and satisfy the condition of X wave [7]. Computer simulation of the filamentation process gives opportunity to analyze separately supercontinuum and spectrum of filament. The spatio-temporal spectra (supercontinuum part, filament and intermediate) is presented in Fig. 3.3, for 4 different input diameter. It is obvious, that the angular dispersion is much more visible in the blue part than in red one. Note also, that the limit values of the spectrum broadening in the blue side does not depend on the beam focusing conditions (Fig. 3.4). This could be explained by the fact that the maximum reached intensity of the blue peak was the same in all 4 cases (32 TW/cm^2, see Fig. 3.2). However, the red-shifted pulse when the focusing is loose (48 μm diameter) propagates over longer distance and keeps high intensity. That causes more spectra broadening to the red side (see Fig. 3.4). The red-shifted pulse nearly invariant propagation over long distances when the focusing is loose, could be explained by conical wave large size energy reservoir, capable to refill energy and suppress diffraction and nonlinear absorption. The red-shifted pulse intensity is lower and group velocity is much less than the blue pulse, therefore it does not exhausts the energy reservoir so quick as the blue pulse.

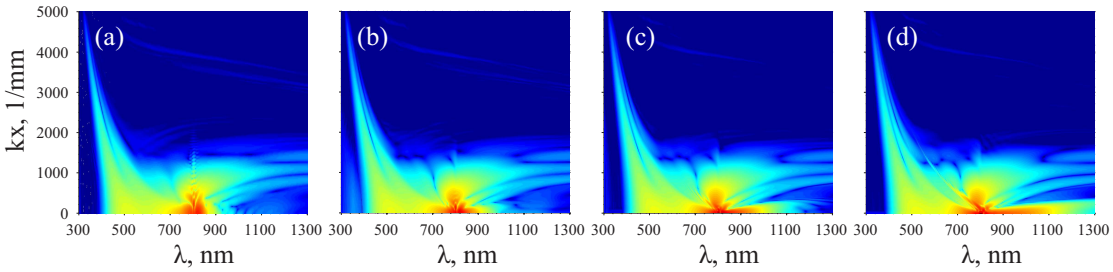

Figure 3.3: Spatio-temporal spectrum intensity distributions for the case of 6 μm(a), 12 μm(b), 24 μm(c) and 48 μm(d) initial diameter pulses. In all cases the maximum intensity level was $32 TW/cm^2$.

The angular dispersion of split pulses is different for the blue and red pulses (see Fig. 3.5). The higher intensity of the split pulse makes the GV larger difference from central frequency GV (initial pulse). Both red and blue-shifted pulse

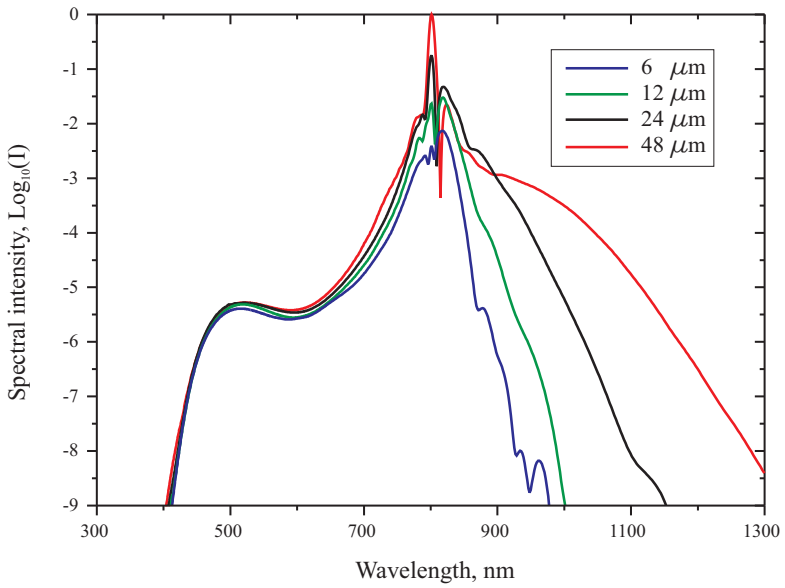

Figure 3.4: On-axis supercontinuum spectrum for the four different initial beam diameters (6 μm, 12 μm, 24 μm and 48 μm). Pulse maximum intensity in all cases was fixed at $32 TW/cm^2$.

angular dispersion has a gap in temporal frequencies. The right branch of the angular dispersion curve of the blue-shifted pulse is fixed at the central wavelength (800 nm), but the left branch moves to the blue side when the intensity of the blue pulse is increasing. Notice, that shift to the blue side of the spectrum slows down, and may look alike for distinct high intensity. However, the red pulse angular dispersion is totaly different. The red shifted components forms O-shaped angular dispersion due to anomalous dispersion in that spectral region. The angular dispersion O-curve shrinks, and even disappears while increasing pulse intensity (see Fig. 3.5 arrow down). Therefore during the pulse-splitting event, pulse produces just blue-shifted axial components. The red shifted spectral components are generated via steep forward front (shock front), because of vanished phase matching in this spectral area. When the red pulse intensity drops to certain value, the phase matching condition for red shifted components becomes possible.

We also performed one numerical experiment of very tight focusing condition. The input diameter was 3 μm. In such case the pulse intensity becomes immediately so high, that the generated plasma absorbs the trailing part of the pulse and leads to formation of short superluminal pulse (see Fig. 3.6). Pulse becomes much shorter, but also it contains much less energy and intensity. Further propagation

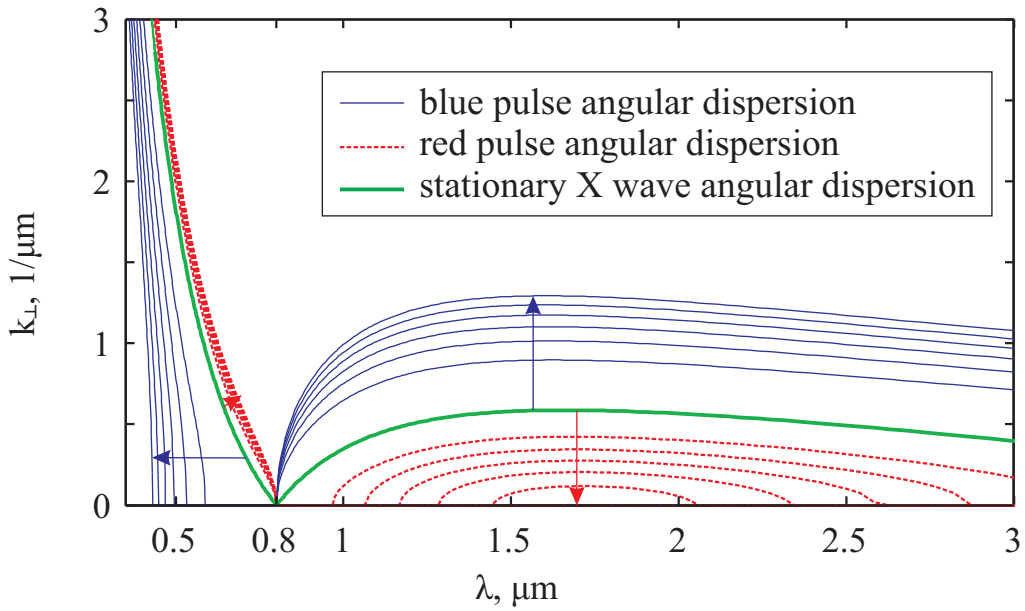

Figure 3.5: Split pulse angular dispersion dependence on pulse intensity (which is proportional to group velocity of the pulse). Blue lines depicts blue (luminal) pulse angular dispersion. Different lines represents pulse intensity change from 5 TW/cm^2 to 30 TW/cm^2 by 5 TW/cm^2. Red lines depicts red (superluminal) pulse angular dispersion. Different lines represents pulse intensity change from 1 TW/cm^2 to 6 TW/cm^2 by 1 TW/cm^2. The arrows in the graph indicate the directions in which the curves move with increasing intensity. Notice the absence of angular dispersion in red shifted components when red pulse intensity reaches 6 TW/cm^2.

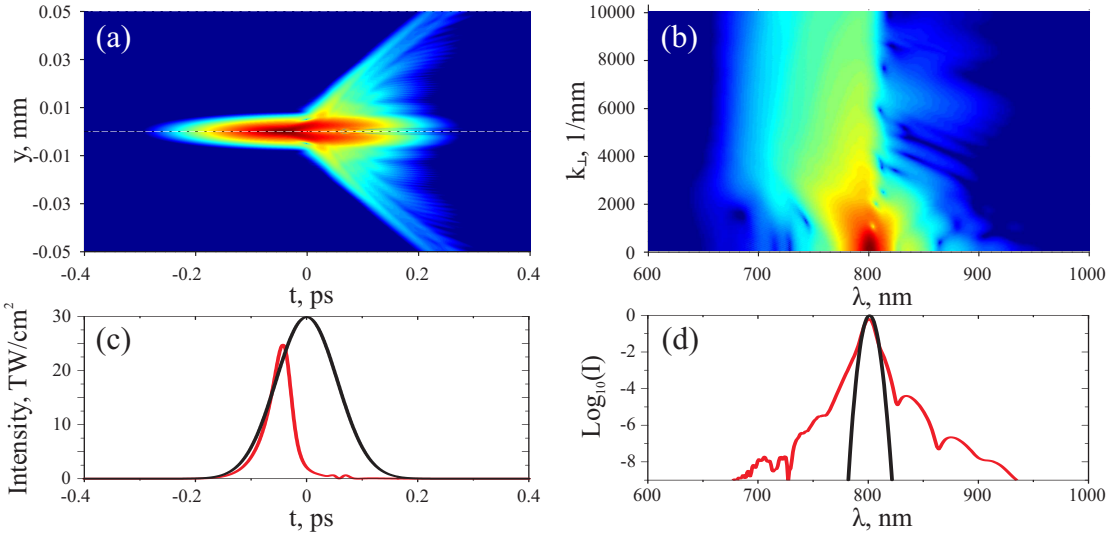

Figure 3.6: Tightly focused beam spatio-temporal intensity profile (a) and angular spectrum(b). Initial (blue) and after some propagation in nonlinear medium (red) temporal profiles and spectrum are presented in (c) and (d) figures.

of such pulse may lead to filamentation, but the permanent damages persisting in the material makes such regime unfeasible.

3.1 Conclusions

The increase of initial beam diameter causes the enhancement of the red-shifted part of the supercontinuum spectra. It can be associated with the larger geometrical size of the reservoir capability to support longer red-shifted conical wave propagation without remarkable intensity drop and without intensity clamping. The *insensitivity* of the supercontinuum blue-shifted part to the beam initial diameter is determined by the intensity clamping of the generated blue-shifted conical wavepacket. Extreme spectra-broadening during filamentation and supercontinuum generation can be explained via intensity dependent phase-matching of the blue- and red-shifted conical waves emerging after the pulse-splitting event. The effect of the intensity clamping at some level predefines the edge values of the supercontinuum spectra.

Chapter 4

Ultrashort light pulse filamentation in a liquid scattering medium

Material related to this thesis chapter was published in [A1]

The extended explanation of filamentation process was presented in previous chapters. As it was mentioned, the recent experiments, involving near-field detection proved spontaneous transformation of the input Gaussian beam into the nonlinear conical wave driven by complex interplay between self-focusing, nonlinear losses (MPA) and diffraction [9]. The conical wave is composed of an intense narrow core (termed a filament), which carries just a small fraction of the total energy, and an extended, low-intensity, but large energy reservoir, which travel locked as a single quasistationary profile. Only the intense core interacts nonlinearly with the medium, and so experiences nonlinear energy losses, while the extended energy reservoir propagates linearly and continuously refills the core during its propagation. The refilling feature is universal and is observed in transparent solid-state, liquid or gaseous media. To this regard light filaments were shown to survive the collisions with the filament-size obstacles, such as atmospheric obscurants, aerosols, water droplets [69, 70, 71] or artificial opaque screens [10]. By contrast, filament propagation terminates if the extended energy reservoir is blocked [9, 72]. Such a dynamic coexistence of localized and extended counterparts in the conical

wave offers many challenging tasks in applied research ranging from atmospheric applications to extended-depth microprocessing of transparent solids.

To date, much effort has been directed to the filamentation in scattering media with implications to long-range propagation, remote sensing and lightning control in adverse atmospheric conditions, in the presence of rain, fog, aerosol scattering and high turbulence [73, 74, 75, 76, 77], see also [78] for a comprehensive review on the topic. Numerically, light scattering in the atmospheric propagation may be simply simulated by introducing some energy dissipation through linear losses [79] or using a stratified model consisting of a sequence of aerosol screens [80]. On a smaller scale, many questions still remain open concerning the propagation of narrow light beams in biological systems that are transparent but exhibit strong scattering [81, 82]. To this regard, nonlinear propagation of the ultrashort light pulses in biological systems opens many new challenges as localized in-depth nonlinear excitation of biological agents, two-photon microscopy within a tissue and precise laser cutting [83, 84, 85], to mention a few.

In this chapter the report on numerical and experimental results on the picosecond laser pulse filamentation in a liquid scattering medium (aqueous suspension of 2 μm polystyrene microspheres of different concentration) is presented. Experimental and numerical results imply that strong scattering leads to distortions of the filament energy reservoir developing an apparent speckle structure, but does not greatly alter filament formation and propagation dynamics.

4.1 Scattering

Scattering of electromagnetic radiation is the process in which electromagnetic radiation is deflected by particles in the matter through which it propagate. In elastic scattering the photons of radiation are reflected; i.e. they bounce off the atoms and molecules without any change of energy [86]. Optical radiation scatter by particles is divided into two cases depending on the scattering particle size and scattered wavelength ratio. If the particle diameter is less than 1/15 of wavelength,

such scattering process is called Rayleigh scattering. If particles are larger than 1/15 of wavelength, the scatter process is usually called Mi scattering. G. A. Mi developed particle scattering theory in 1908 and applied it to spherical particles, but term "Mi scatter" is in use even when the scattering particles are nonsymmetric. In the limit of small particle size, the Mi theory becomes valid for Rayleigh scattering. Rayleigh found that scattered intensity is inversely proportional to the wavelength fourth power $I_v \sim \frac{1}{\lambda^4}$

The scattering particle is composed of large number of molecules. Each molecule behaves as an elementary dipole, oscillating in incident electro-magnetic field, and, thus generating secondary electromagnetic waves i.e. scattered radiation. Such approach is common both for Rayleigh and Mi scattering. However, there are some important differences:

1. In Rayleigh scattering the dipoles radiate coherently, while the Mi scattering is not composed by radiation of coherent dipoles: it is necessary to account for the optical path in particle and its surrounding.

2. The fields irradiated by elementary dipoles during Rayleigh scattering interfere and do not depend on the direction. In the Mi scattering the irradiated fields by dipoles at different directions and positions have different phases. Thus the interference result becomes dependant on angle: scattered wave intensity has some angular distribution.

The most remarkable difference between Rayleigh and Mi scattering is completely different dependence on wavelength. The Mi scattering is produced by large size particles and almost has no dependence on wavelength. On the contrary, Rayleigh scattering exhibits strong dependence on wavelength ($\frac{1}{\lambda^4}$), thus the shorter (blue) radiation is scattered more effectively than longer (red) radiation.

From mathematical point of view Mi theory is Maxwell equation solution while the elementary dipoles are positioned on a sphere surface and scattering centers are defined by magnetic permittivity and electrical conduction [87, 88]. Result consist

of sum series and could be easily found by computer. The Fig. 4.1 demonstrates transition from Rayleigh to Mi scattering when the size of the particle is increasing. The larger diameter of particles (d/λ¿¿1) causes the larger asymmetry between forward and backward scattering. When the particle size is very big the forward scattering dominates.

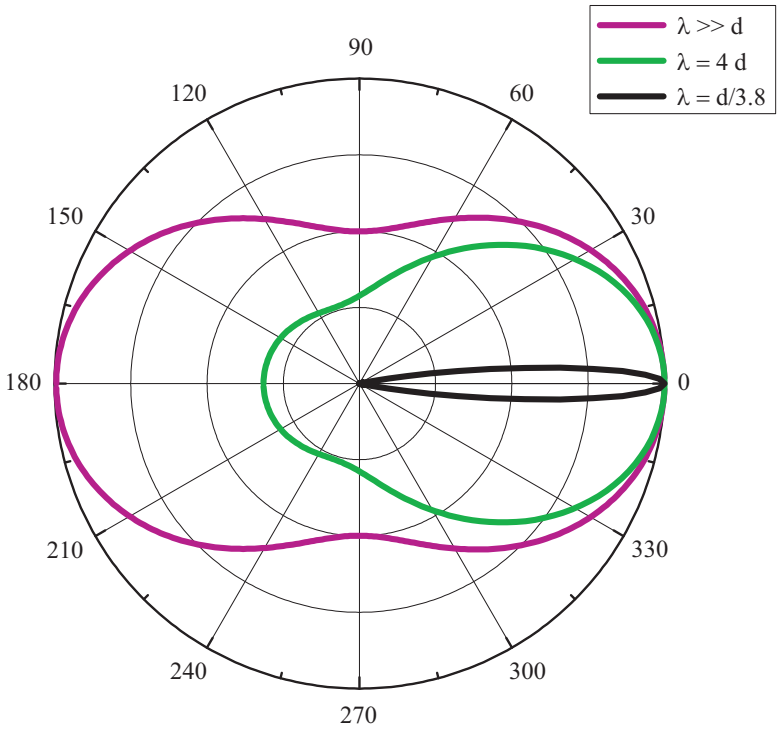

Figure 4.1: Normalized scattered field angular dependence in three different cases, where λ is wavelength and d - is particle diameter.

Scattering by very large particles ($r \gg \lambda$) is calculated by geometrical means, accounting interference, reflection and refraction on particle surface. Light scattering by very large particles determine aureole, rainbow and other effects in fog, rain and etc.. Rayleigh scattering explains the blue color of the sky, while Mi scatter the white color of the clouds.

4.2 Experiment setup and results

The experiment was carried out with chirped-pulse-amplification based Nd:glass laser system (Twinkle, Light Conversion Ltd.) delivering $\lambda = 1054$ nm, 1 ps pulses at 10 Hz repetition rate. The output laser beam was frequency doubled, attenu-

ated and spatially filtered to yield a clean Gaussian profile at $\lambda = 527$ nm with 1.2 mm FWHM diameter. The second-harmonic beam was loosely focused by a f=+500 mm lens down to 80 μm FWHM diameter onto the front-face of the syringe-shaped cuvette with fused silica windows. The cuvette was filled either with aqueous suspension of 2 μm diameter calibrated polystyrene microspheres, provided by Vasmo Inc. (Indianapolis, IN) or with pure water for a comparative study. The input pulse energy was set $E_{in} = 6$ μJ, so as to excite a single filament inside a cuvette filled with pure water at a distance $z = 12$ mm from its front-face. The construction of the cuvette allowed to easily vary its length and monitor the output beam near-field fluence profile, and therefore capture in detail the propagation dynamics. In doing so, the output face of the cuvette was imaged onto a 10-bit dynamic range Charge-Coupled Device (CCD) camera (COHU-6612 linked to Spiricon LBA-400PC frame grabber) by means of an achromatic f=+50 mm lens, with 7 $\times$ magnification.

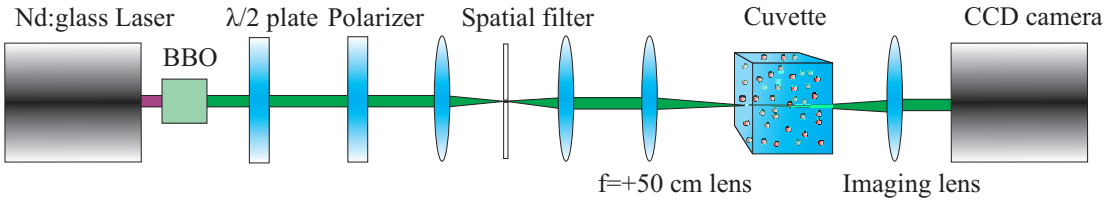

Figure 4.2: Experimental setup.

Fig. 4.3 compares beam propagation and filament formation dynamics in the absence (in pure water, Fig. 4.3 (a,c)) and in the presence (in aqueous suspension of 2 μm polystyrene microspheres with 6000 mm^{-3} particle density, Fig. 4.3 (b,d)) of light scattering. The general side-views of a full-length propagation in a 40-mm-long cuvette were taken by a digital photo camera using the same input energy of $E_{in} = 6$ μJ. The most of scattered light is confined within a cone having vertex angle of 10° indicated by light lines in Fig. 4.3 (b), whereas dark lines denote the scattering angle to half maximum intensity, as calculated using Mie scattering theory [89], and which are in good agreement with the experimental results. Laser beam filamentation is visualized by the appearance of the white-light continuum

emission and is detected using an orange filter that transmits only wavelengths longer than 600 nm as shown in Fig. 4.3 (c) and (d). In order to observe an appreciable signal from a side-view in pure water, a very diluted solution of the scatterers in this case and increased exposure time was used.

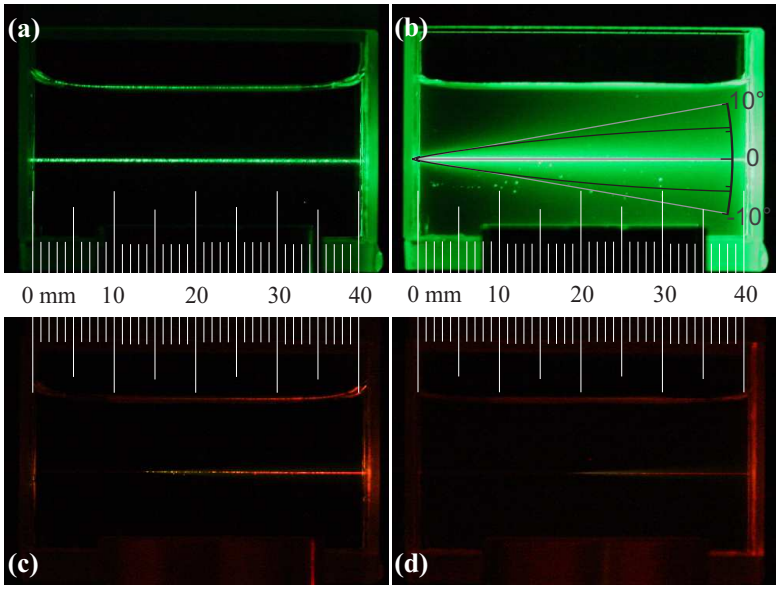

Figure 4.3: Side-view of the cuvette in the nonlinear propagation regime at $E_{in} = 6$ μJ: (a) pure water, (b) aqueous solution of 2 μm polystyrene microspheres with 6000 mm^{-3} particle density. (c) and (d) are the respective images recorded using an orange filter.

In pure water, beam filamentation starts at $z = 12$ mm from the input face as seen from Fig. 4.3 (c), whereas in the presence of scattering, the nonlinear focus and filament start point is shifted towards the output face, and under these experimental settings still occurs within the cuvette length. Typical near-field images of the radiation, which was detected by imaging the output face of the cuvette onto a CCD camera and continuously varying the propagation length are shown in Fig. 4.4. Although the scattering is found to affect the filament start position resulting in somewhat farther point of the nonlinear focus, observations suggests that even in the presence of strong scattering (energy losses up to 50%) the transverse beam profile, which takes the shape of an intense central core (filament) surrounded by an extended (conical) peripheral radiation is highly resistant to local perturbations imposed by the scatterers. The peripheral part of the radiation develops an apparent speckle structure, which is still able of refilling the nonlinear

losses due to MPA experienced by the intense central core and linear losses due to scattering experienced by the entire beam. Note that the diameter of a single microsphere comprises $\sim 16\%$ of the estimated filament FWHM width (12 μm).

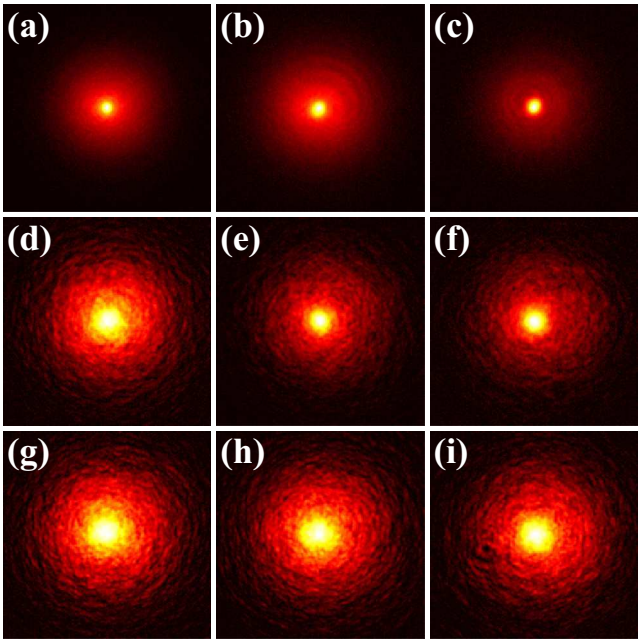

Figure 4.4: Experimentally measured single-shot fluence profiles of the beam beyond the nonlinear focus: (a-c) in pure water, (d-f) in aqueous suspension of the polystyrene microspheres of 6000 mm^{-3}, (g-i) - 8000 mm^{-3} aqueous polystyrene microspheres suspension at $z = 12, 16, 20$ mm. Window size is 0.3 mm x 0.3 mm.

4.3 The numerical model and results

The propagation in the scattering medium was modelled in the framework of the NLSequation for the monochromatic field amplitude A with account for diffraction, self-focusing, MPA [9] and with addition of a stochastic term, which simulates size, properties and distribution of the scattering particles:

$$\frac{\partial A}{\partial z} = \frac{i}{2k}(\frac{\partial^2}{\partial x^2} + \frac{\partial^2}{\partial y^2})A + \frac{i\omega n_2}{c}|A|^2 A - \frac{\beta^{(K)}}{2}|A|^{2K-2}A - \gamma A, \qquad (4.1)$$

where z is the propagation distance, ω is the carrier frequency, $k = n\omega/c$ is the wave number, n and n_2 are the linear and nonlinear refractive indexes, respectively, K is the order of MPA with $\beta^{(K)}$ being the MPA coefficient, and γ is the stochastic complex function (specified in the text below). In simulations following values of

the relevant parameters were used $n = 1.33$, $n_2 = 2.7 \times 10^{-16}$ cm^2/W, $K = 3$ (three photon absorption with account of water bandgap $E_g = 6.5$ eV) and $\beta^{(3)} = 2 \times 10^{-23}$ cm^3/W^2 as taken from Ref. [90]. Eq. 4.1 was solved by means of commonly used split-step Fourier method. Specifically, the medium is divided into a number of layers N of arbitrary thickness Δz, and the propagation through each particular layer was simulated in few passes. The full numerical procedure is schematically depicted in Fig. 4.5(a) and is performed as follows: the first pass through the N-th layer calculates the diffraction by solving equation

$$\frac{\partial A}{\partial z} = \frac{i}{2k}\left(\frac{\partial^2}{\partial x^2} + \frac{\partial^2}{\partial y^2}\right) A, \tag{4.2}$$

by means of fast Fourier transform. Thereafter the same layer is passed again, but just with account for self-focusing

$$\frac{\partial A}{\partial z} = \frac{i\omega n_2}{c}|A|^2 A. \tag{4.3}$$

The third passage accounts for MPA

$$\frac{\partial A}{\partial z} = -\frac{\beta^{(K)}}{2}|A|^{2K-2} A, \tag{4.4}$$

and the last one for scattering

$$\frac{\partial A}{\partial z} = -\gamma A, \tag{4.5}$$

where $\gamma(x, y, z)$ is a complex numbers matrix describes the properties and location of randomly distributed scattering particles. Specifically, its real part, $Re[\gamma(x, y)]$, describes the absorption, while its imaginary part, $Im[\gamma(x, y)]$ describes the phase shift (dephasing) introduced by a scattering particle. More generally, for N-th layer, $\gamma(x, y, z_N)$ represents a matrix of random complex values, characterizing the properties of the scatterers: concentration, size and opacity, as illustrated in Fig. 4.5(b). The calculation procedure is repeated within a next layer, with the

last step involving the generation of a new matrix $\gamma(x, y, z_N)$, which keeps particle physical properties fixed and changing just their spatial distribution. The layer thickness Δz in our calculations was chosen to be an average distance between the scattering particles, that is $\sim 45 - 55$ μm for the scattering particle concentration of 10000 to 6000 cm^{-3}. The grid size in the (x, y) plane was 0.2 mm $\times$ 0.2 mm, with 0.4 μm resolution and 2^{18} pixels.

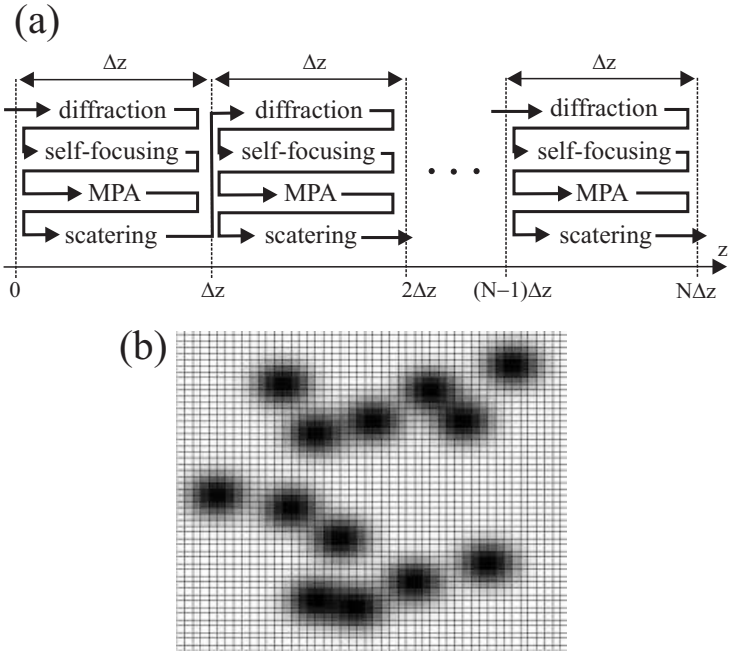

Figure 4.5: (a) A schematic representation of the numerical procedure, (b) example of the $\gamma(x, y, z)$.

Since the actual properties of the scattering particles (refractive index, absorption, etc.) were not provided by the producer, the actual extinction experienced by the laser beam was estimated from the energy loss due to scattering in the linear propagation regime of an extended Gaussian beam with wavelength 527 nm, and power below the critical power for self-focusing. Experimental estimation of the energy losses due to scattering in 10 mm cuvette, for 6000 mm^{-3}, 8000 mm^{-3} and 10000 mm^{-3} particle density gives values of 40%, 49% and 57%, respectively. In this measurement a 10-mm diameter iris aperture centered on the beam propagation axis and Ophir Optronics energy meter with a photodiode PE-10 were used. The iris aperture was placed 1 m after the cuvette in order to

detect the energy confined within a cone with angle of 10 mrad. The measured energy losses corresponded to the extinction coefficient of 0.051 mm^{-1}, 0.0673 mm^{-1} and 0.0844 mm^{-1}, respectively, for particle concentrations indicated above. These values were used for the calibration of the model.

Although the model is developed for monochromatic wave and it does not account for more specific features of the nonlinear medium owing to effective nonlinear refractive index [91], effects of scattering dependence on the pulse duration [92], a good qualitative agreement between numeric and experimental data was obtained. Fig. 4.6 compares the simulated and experimentally measured fluence profiles of the beam after 20 mm of propagation in aqueous suspension of polystyrene microspheres with 8000 mm^{-3} particle density outlining a development of apparent speckle structure in both cases. The only difference is observed in the far periphery because a portion of scattered light at large angles is not collected in the imaging lens in the experiment. Fig. 4.7 (a) compares measured and numerically simulated filamentation dynamics (diameter of the central core, i.e. filament, *versus* propagation distance).

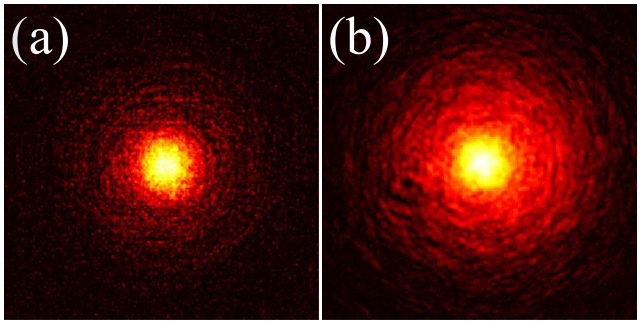

Figure 4.6: Numericaly retrieved (a) and experimentally measured (b) beam profiles after 20 mm propagation in aqueous suspension of polystyrene microspheres with 8000 mm^{-3} particle density. Window size is 0.3 mm x 0.3 mm.

Note, that in numeric simulation, the 2 μm-particle introduces strong diffraction, and the Fourier transform algorithm fails when the diffracted light becomes reflected from the boundary of the calculation window. This problem was solved in two different ways: (i) by introducing a spatial filter after passing each layer: the spatial filter cuts large angle spatial components, having no effect on the central

part of the beam; (ii) by replacing the scattering particles with the effective ones, which are larger in size and posses some effective absorption. In this case larger particles introduce smaller diffraction, so that the diminished scattering losses are "compensated" by the absorption. In the latter case we have used the effective particles of 16 μm diameter and 0.15 mm^{-1} absorption coefficient. The comparison between the two simulation approaches is illustrated in Fig. 4.7 (b). It can be seen that both algorithms provide a very similar result concerning the beam diameter, where a slight difference might be recognized only for larger particle concentration and for longer propagation distance. However, in the case of effective particles, the speckle structure is less developed and thus leads to smoother evolution of the beam diameter.

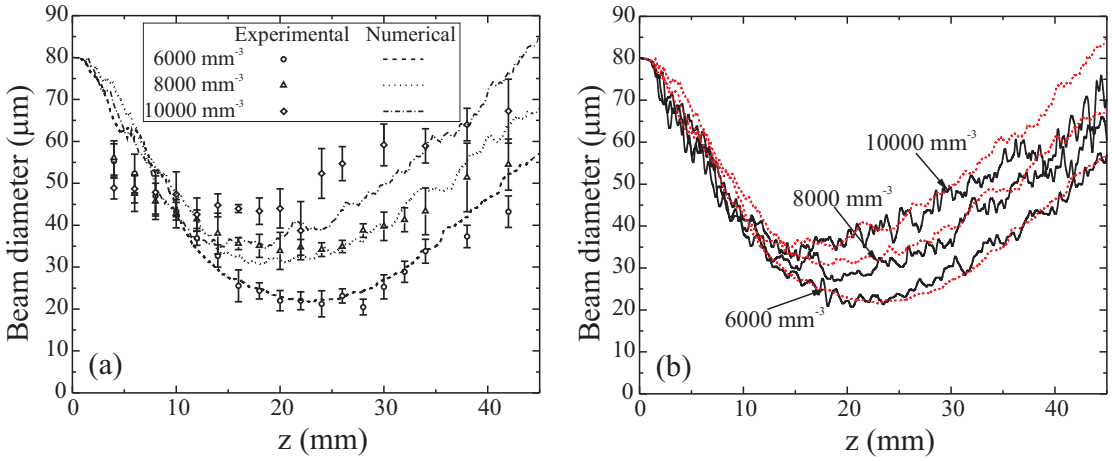

Figure 4.7: (a) comparison of experimental data with numerical simulations of the filament diameter during propagation in aqueous suspension of $2-\mu$m polystyrene microspheres of different concentration. (b) comparison of numerical results obtained with different computation algorithm, solid curves – introducing spatial filter, dotted curves – with larger effective particles. See text for details.

4.4 Conclusions

In conclusion, the filamentation dynamics of the ultrashort light pulses in a liquid scattering medium was investigated. It was shown that light scattering introduced by the polystyrene microspheres shifts the nonlinear focus (emergence of the filament) toward further propagation distance, and results in somewhat larger filament diameter along with appearance of speckle structure in the pe-

ripheral part of the beam. The developed monochromatic model, which accounts for diffraction, self-focusing, MPA and light scattering, qualitatively reproduces the relevant propagation features observed experimentally with picosecond light pulses. The model is flexible in choosing the parameters of scattering particles (density, size and transparency) and could be easily adopted to any other scattering medium.

Chapter 5

Filamentation of highly elliptical ultrashort pulsed laser beam

Material related to this thesis chapter was published in [A2,A3] and [C1,C2,C6-C8]

When the beam power well exceeds the critical power for self-focusing($P_0 \gg P_c$), the beam breaks-up into Multiple Filaments (MF) [93, 94, 95]. The nature of the multiple filamentation process is described in terms of growth of wave-front perturbations (known as transverse modulation instability) and leads to random filament distribution over a given transverse plane. Multiple filaments originating from a single input beam exhibit high coherence properties and serve as a source of multichannel white-light radiation [96], or may be used for phase-matched ultrafast Raman frequency conversion [97], production of plasma channels [98] and guiding of microwave radiation [99]. However, most of the applications require precise filament localization and high MF pattern reproducibility. Recently, a variety of methods to control multiple filamentation had been developed. The majority of the methods are based on the control of beam focusing conditions, that is the modification of the input beam amplitude and phase, introducing a beam astigmatism via tilted lens [100] or deformable mirror [101], grids and slits for periodic amplitude modulation [80, 102] and phase masks [103]. Alternatively, control of the MF patterns may be realized by the use of circularly polarized laser beams [104], by doping liquid media with strongly nonlinearly absorbing dye [105] and finally, by injection of a weak laser beam, which allows all-optical control of

switching on and off the multiple filamentation process [106, 107].

Another solution of obtaining regular MF patterns is to introduce a certain ellipticity on the input laser beam [108]. The break-up of elliptical laser beams is universal, and regular MF patterns had been experimentally observed in water [108], air [109], carbon disulfide [110], BK7 glass [111], and fused silica [112]. Regardless of the physical state of the nonlinear medium (solid, liquid or gas) even slight input beam ellipticity overcomes the random nature of the beam break-up and results in deterministic and highly reproducible MF patterns. It was recently demonstrated that in the case of large beam ellipticity, light filaments evolve along the major axis of the beam with constant spacing thus forming a periodic one-dimensional MF array [113]. Despite of a wide range of potential applications based on the periodicity of the MF array, specific factors determining the period has not been explicitly studied yet. The major question still concerns the distance between the adjacent filaments and the whole period of the MF array.

Giuliano in 1972 noticed [114], that elliptical beam critical self-focusing power exceeds the critical power for round (radially symmetric) beams. Thus it is possible to use higher beam energies without optically breaking the material. The more deep study on elliptical beam self-focusing was made by Cornoti with colleagues [115] in 1990. The aberration-free model of beam focusing was considered *i. e.* the beam maintains its shape during the self-focusing process

$$|E|^2 = \frac{E_0^2}{a\,(z)\,b\,(z)} exp\left(-\left[\frac{x}{a\,(z)}\right]^2 - \left[\frac{y}{b\,(z)}\right]^2\right) \tag{5.1}$$

where $a\,(z)$ and $b\,(z)$ are beam diameters on x and y axis. Using this assumption the NLS equation

$$\nabla^2 E + k^2\left(1 + \varepsilon_2 |E|^2\right) E = 0 \tag{5.2}$$

might be divided into two coupled differential equations, which describes beam

diameter evolution during propagation

$$\begin{aligned} k^2 \frac{d^2 a}{dz^2} &= \frac{1}{a^3} - \frac{\eta}{a^2 b}; \\ k^2 \frac{d^2 b}{dz^2} &= \frac{1}{b^3} - \frac{\eta}{b^2 a}. \end{aligned} \tag{5.3}$$

where $\eta = P_{el}/P_c$ - critical power ratio. The elliptical beam critical power for self-focusing was obtained from the solution of Eq. 5.3

$$P_{el}(e) = \left(\frac{e + 1/e}{2} \right) P_c, \tag{5.4}$$

where $e = b(0)/a(0)$ is the beam ellipticity and P_c is rounded Gauss beam critical self-focusing power. Further the non-aberrative focusing model was extended with addition of dispersion, saturating nonlinearity. However, findings were not compared with numerical simulations or experiments. Later it was recognized, that self-focusing is much more complex as it was thought. Beam undergo significant change of the envelope. It was noticed, that non-aberrative method is not accurate and even misleading. Variational method was proposed to fix the problems [116], additionally the Gaussian envelope was replaced by super-Gaussian, or sometimes hyperbolic secant. These methods usually called non-aberrative paraxial, variational, or coupled axis. However, all of these methods are based on false assumption, that propagating beam maintains its shape. Gross and Manassah demonstrated [117], that non-aberrative model does not coincide with NLS equation numerical simulation results. Furthermore it was noticed that elliptical beam propagating in nonlinear medium transforms into radially symmetric, that obviously contradicts non-aberrational propagation. The real critical self-focusing power of elliptical beam derived from fitting numerical NLS equation simulation results was determined by Fibich with Ilan [118]. Retrieved critical self-focusing power dependence on beam elipticity was 60% less than it could be calculated

from Eq. 5.4. The best retrieved approximation is

$$P_{el}\left(e\right) \approx \left(0.4h_e + 0.6\right) P_c, \tag{5.5}$$

here $h_e = \frac{e+1/e}{2}$. To explain such difference, the partial beam self-focusing model was proposed. Thus only a part of the beam is able to change its shape and undergo the collapse. As the evidence the elliptical beam reshaping to radially symmetric is represented. The retrieved super-Gaussian beam critical power in non-aberrative model was overestimated [59] too. In this chapter will be demonstrated that self-focusing of high power beams with large ellipticity lead to formation of periodic highly reproducible multifilament arrays.

5.1 2D numerical simulations of multiple filamentation dynamics

The time-integrated ultrashort pulse filamentation could be successfully described by continuous-wave models [119]. In this section multiple filamentation dynamics of monochromatic elliptical laser beam is studied by solving the NLS equation, which accounts for diffraction, self-focusing and MPA [108]:

$$\frac{\partial A}{\partial z} = \frac{i}{2k}\left(\frac{\partial^2}{\partial x^2} + \frac{\partial^2}{\partial y^2}\right) A + \frac{i\omega n_2}{c}|A|^2 A - \frac{\beta^{(K)}}{2}|A|^{2K-2}A, \tag{5.6}$$

where z is the propagation distance, ω is the carrier frequency, $k = n_0\omega/c$ is the wave number, n and n_2 are the linear and nonlinear refractive indexes, respectively, $\beta^{(K)}$ is the MPA coefficient with K being the order of the MPA. A is the complex amplitude of the electric field, defined at the input ($z = 0$) as

$$A_{in}(x, y) = A_0 \exp\left[-2\ln 2\left(\frac{x^2}{a_x^2} + \frac{y^2}{a_y^2}\right)\right], \tag{5.7}$$

where a_x and a_y are FWHM beam widths along x and y axes, respectively. Eq. (5.6) was solved numerically by split-step Fourier method with $\lambda = 527$ nm, $n_0 = 1.46$, $n_2 = 2.24 \times 10^{-20}$ m^2/W, $K = 3$, $\beta^{(3)} = 1 \times 10^{-23}$ cm^3/W^2, taking

the input beam dimensions $a_x = 1.3mm$ and $a_y = 0.17mm; 0.02mm$ as in the experiment. The added 5 % amplitude noise on the input beam profile, was very close to that evaluated experimentally. From the numerical simulations it was verified that the initial amplitude of the added noise (in the range of $1 - 10$ %) does not greatly alter the final result (MF period in particular), at least in the applied power range, what is in good agreement with the recent study concerning multiple filamentation of circular laser beams [119]. The input intensity I_0 was varied from 30 GW/cm^2 to 600 GW/cm^2 so as to cover the range of experimental values.

Fig. 5.1 (a)–(c) illustrates few examples of the near field intensity distribution of the beam *vs* propagation distance at $I_0 = 32$ GW/cm^2. The elliptical input beam [Fig. 5.1 (a)] propagating in the nonlinear medium experiences 1-dimensional self-focusing along its short (y) axis [Fig. 5.1 (b)] and eventually breaks-up into 1-dimensional array of regularly spaced light filaments [Fig. 5.1 (c)]. The numerically simulated propagation dynamics are qualitatively consistent with recent experimental observations of the beam propagation dynamics in water [113]. Fig. 5.1 (d) plots the near field intensity distribution at $I_0 = 58$ GW/cm^2, illustrating the formation of two-dimensional MF array. The simulated MF patterns at the output of the sample ($z = 45$ mm) reproduce those recorded in the experiment. More detailed comparison between the numerical and experimental data is accomplished in terms of the MF array period, with the results being summarized in section 5.3.

Fig. 5.2 illustrates the dynamics of the far field (numeric simulation) spectra plotted in (k_x, k_y) space, each of these correspond to the near field images presented in Fig. 5.1 (a)–(c). These plots demonstrate how the wave vector spectrum of the input beam [Fig. 5.2 (a)] notably broadens along k_y direction as a result of self-focusing [Fig. 5.2 (b)], while the occurrence of distinct sidebands along k_x direction [Fig. 5.2 (c)] triggers the beam break-up into multiple filaments. The position of the sidebands determines the period of the MF array. Closer inspection

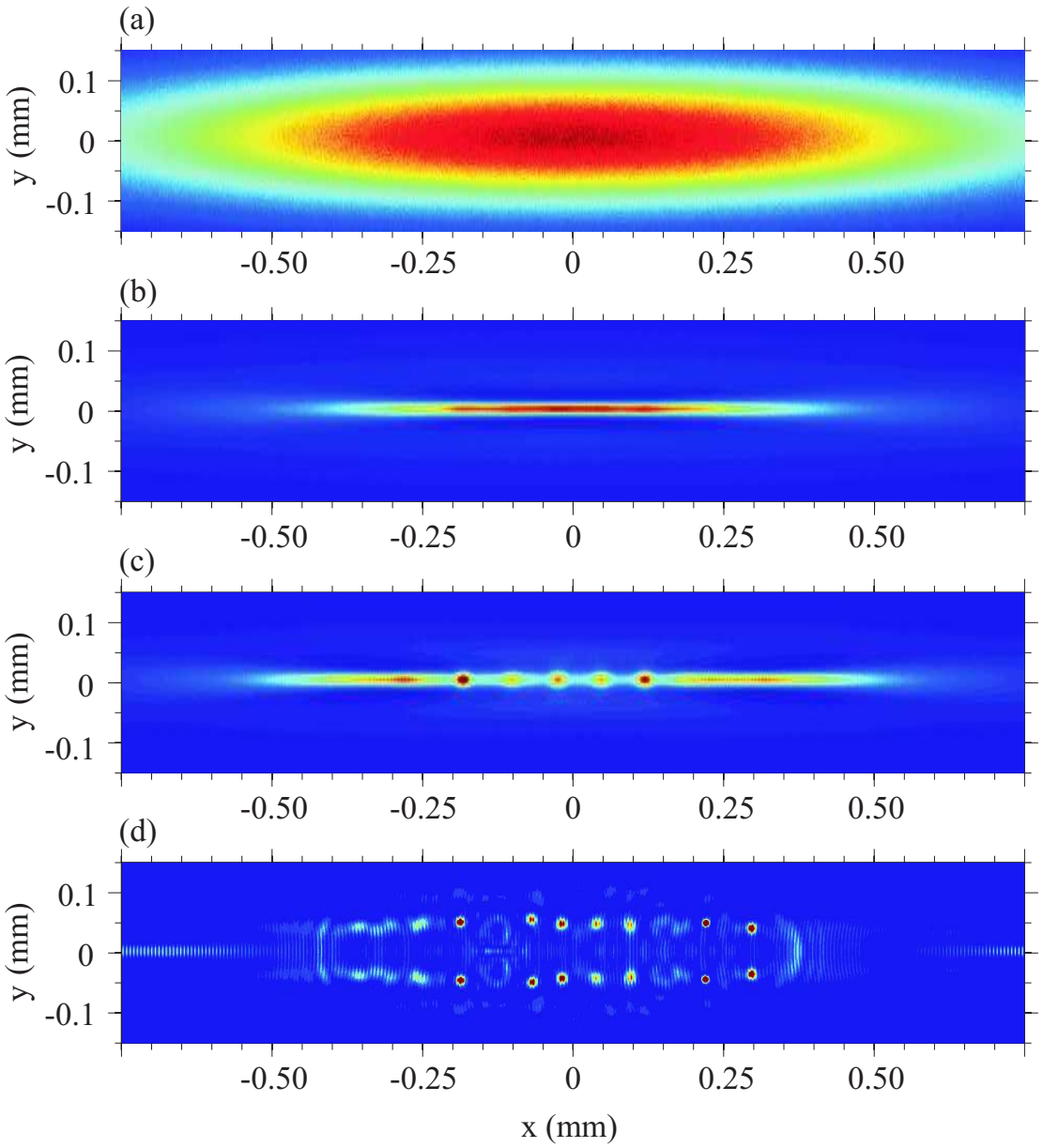

Figure 5.1: Numerical simulation of intense laser beam ($a_x = 1.7mm, a_y = 0.17mm$) propagation in fused silica. Normalized near field intensity profile (a) at the input ($z = 0$ mm), (b) inside ($z = 40$ mm), and (c) at the output ($z = 45$ mm) of the sample at $I_0 = 32$ GW/cm^2. (d) shows the output beam profile at $I_0 = 58$ GW/cm^2.

revealed that the position of the sidebands is in fair agreement with the standard modulational instability theory, which associates the break-up of intense laser beams into multiple filaments with the growth of perturbations present in the input beam wavefront by means of the four-wave parametric mixing process, as described in detail in [120].

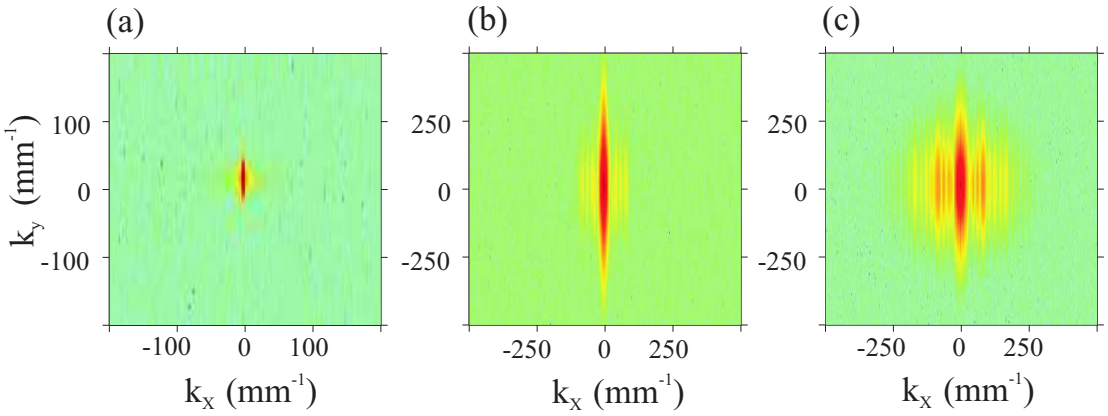

Figure 5.2: Far-field intensity distribution (on a logarithmic intensity scale) plotted as (k_x, k_y) spectra, corresponding to images shown in Fig. 5.1(a)–(c).

5.2 Multistep four-wave mixing model

Several alternative ways have been proposed to describe multiple filamentation phenomena without numerical integration and which provide useful insights into the underlying physics. In particular, a classical approach is based on the theory of modulational instability [120], while the most recent work considers ray tracing adopted to a nonlinear optical system [121]. In what follows, a simple analytical model was introduced, which explains multiple filamentation as a sole result of the multistep four-wave parametric interactions, occurring in the self-focusing high power elliptical laser beam and reproduces in detail the basic features of experimentally observed one- and two-dimensional MF arrays.

The schematic step-by-step representation of the interacting wave vectors is shown in Fig. 5.3. Suppose an input monochromatic elliptical Gaussian beam with the central wave vector $\vec{k}_1$, while its full $k-$vector spectrum is confined within an ellipse depicted by a dashed line in the (k_x, k_y) plane, as shown in Fig. 5.3 (a). In the first step, an input elliptical beam experiences self-focusing, which leads to enrichment of its wave vector spectrum by new components (within an ellipse depicted by a solid line) with a pair of vectors $\vec{k}_4$ among them, so that the non-collinear phase matching condition for the four-wave parametric amplification

$$\vec{k}_1 + \vec{k}_1 = \vec{k}_4 + \vec{k}_4 \tag{5.8}$$

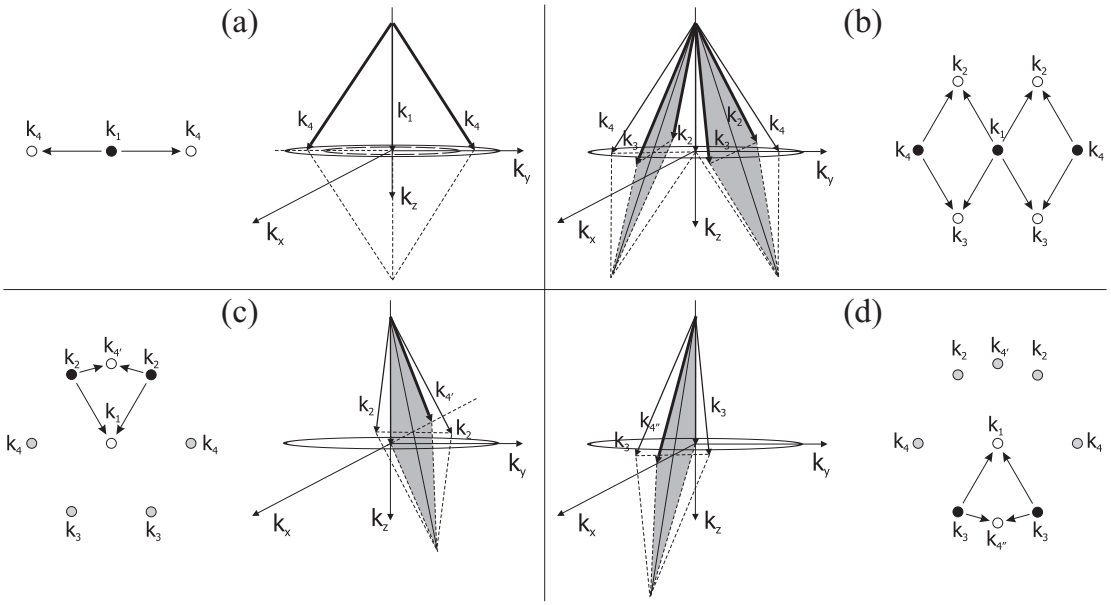

Figure 5.3: Schematic illustration of the multistep four-wave mixing process in $k-$space. The resulting wave vectors in each step are depicted by bold arrows. Shaded areas indicate that the resulting vectors lie in a different plane than the initial ones. The each step is also explained by showing 2D diagrams for transverse k vectors (depicted by circles). Black circles depicts pump wave of the current step, the white circles depicts the generated components via FWM and gray circles depicts waves generated in previous steps. The arrows in 2D diagrams describes the direction of energy transfer. See text for description.

becomes satisfied, where

$$|\vec{k}_1| = \frac{2\pi}{\lambda_0}(n_0 + n_2 I_0), \tag{5.9}$$

$$|\vec{k}_4| = \frac{2\pi}{\lambda_0}(n_0 + 2n_2 I_0), \tag{5.10}$$

are the wave vectors, modified via local refractive index change due to the optical Kerr effect. Assuming the monochromatic case and frequency-degenerate interaction, the modulus of $\vec{k}_1$ is modified as a result of the self-phase modulation, and which thus modifies the modulus of a weak signal $\vec{k}_4$ via cross-phase modulation, therefore $|\vec{k}_4|$ is longer than $|\vec{k}_1|$ by $\frac{2\pi n_2 I_0}{\lambda_0}$. Here $\lambda_0 = 527$ nm denotes the central wavelength of the laser radiation. Note that vectors $\vec{k}_1$ and $\vec{k}_4$ lie in the (k_y, k_z) plane with their endpoints located along k_y axis. The second step considers four-wave interaction between $\vec{k}_1$ and $\vec{k}_4$, which gives rise to occurrence of wave vectors

$\vec{k}_2$ and $\vec{k}_3$ as illustrated in Fig. 5.3 (b):

$$\vec{k}_1 + \vec{k}_4 = \vec{k}_2 + \vec{k}_3. \tag{5.11}$$

Here $|\vec{k}_2| = |\vec{k}_3| = |\vec{k}_4|$ and wave vectors moduli are modified via cross-phase modulation. Note that the resultant phase matched vectors $\vec{k}_2$ and $\vec{k}_3$ lie in a tilted plane [perpendicular to (k_y, k_z)], which is indicated by gray shading. The endpoint locations of vectors $\vec{k}_2$ and $\vec{k}_3$ are symmetric with respect to principal axes k_x and k_y, respectively. In the third step, vectors $\vec{k}_2$ and $\vec{k}_3$ interact with the central vector $\vec{k}_1$, and generates $\vec{k}_{4'}$ and $\vec{k}_{4''}$ components

$$\vec{k}_2 + \vec{k}_2 - \vec{k}_1 = \vec{k}_{4'}, \tag{5.12}$$

$$\vec{k}_3 + \vec{k}_3 - \vec{k}_1 = \vec{k}_{4''};$$

$$|\vec{k}_{4'}| = |\vec{k}_{4''}| = |\vec{k}_4|, \tag{5.13}$$

so as $\vec{k}_{4'}$ and $\vec{k}_{4''}$ occur as shown in Fig. 5.3 (c) and (d), whose endpoints are located along k_x axis. Strictly speaking, in the case of monochromatic waves, the phase matching conditions described by Eqs. (5.12) and (5.13) could be fulfilled only by introducing a nonzero phase mismatch Δk. In our experimental settings the phase mismatch was found to be negligibly small ($\Delta k \approx 4$ cm^{-1}), so the wave vectors $\vec{k}_{4'}$ and $\vec{k}_{4''}$ could be generated with still reasonable efficiency. And finally, $\vec{k}_{4'}$ and $\vec{k}_{4''}$ are parametrically amplified by the intense pump $\vec{k}_1$, in analogy with the first step:

$$\vec{k}_1 + \vec{k}_1 = \vec{k}_{4'} + \vec{k}_{4''}. \tag{5.14}$$

The phase-matched multistep four-wave processes therefore give rise to a particular set of wave vectors $\vec{k}_j$ ($j = 1, 2, 3, 4, 4', 4''$). It should be noted that in every four wave mixing step the pump $\vec{k}_1$ vector is one of the phase matched vectors, because it has the biggest power. Power from pump moves to newly gen-

erated waves, therefore phase matched FWM configuration where pump vector is included is most efficient. Furthermore we assume a set of monochromatic waves with central wave vectors $\vec{k}_j$ generated at different steps of the four-wave mixing process as replicas of the initial pump beam with the envelope A_{in} described by Eq. (5.7):

$$A_j(x,y) = C_j A_{\text{in}}(x,y) \exp\left[i(k_{j,x}x + k_{j,y}y)\right], \tag{5.15}$$

where $k_{j,x}$ and $k_{j,y}$ are the respective projections of the wave vectors $\vec{k}_j$. Here arbitrary coefficients C_j represent weighted contributions to the amplitudes of each wave. The output intensity pattern is calculated as a superposition of waves described by Eq. 5.15:

$$I(x,y) = \left| \sum A_j(x,y) \right|^2. \tag{5.16}$$

Figure 5.4 illustrates the resulting intensity distribution calculated for different input beam intensities, and qualitatively reproduces the experimentally observed MF patterns and the occurrence of the secondary filament bands in particular. Values of C_j ($C_1 = 1.0, C_2 = C_3 = C_4 = 0.6, C_{4'} = C_{4"} = 0.4$) in our calculation were chosen so as to obtain a distinct visibility contrast in the resulting intensity distribution pattern. We note that in the present model C_j is a freely chosen parameter, which, however, has just a weak effect on the period of the MF array. Therefore periodic break-up of the elliptical laser beam along its long axis is dictated by beating of the wave vector components along k_x axis, while the secondary MF bands originate from the beating of the wave vector components distributed along k_y axis. Also note that possible interactions between the neighboring filaments as well as the input beam contraction due to self-focusing are not accounted for.

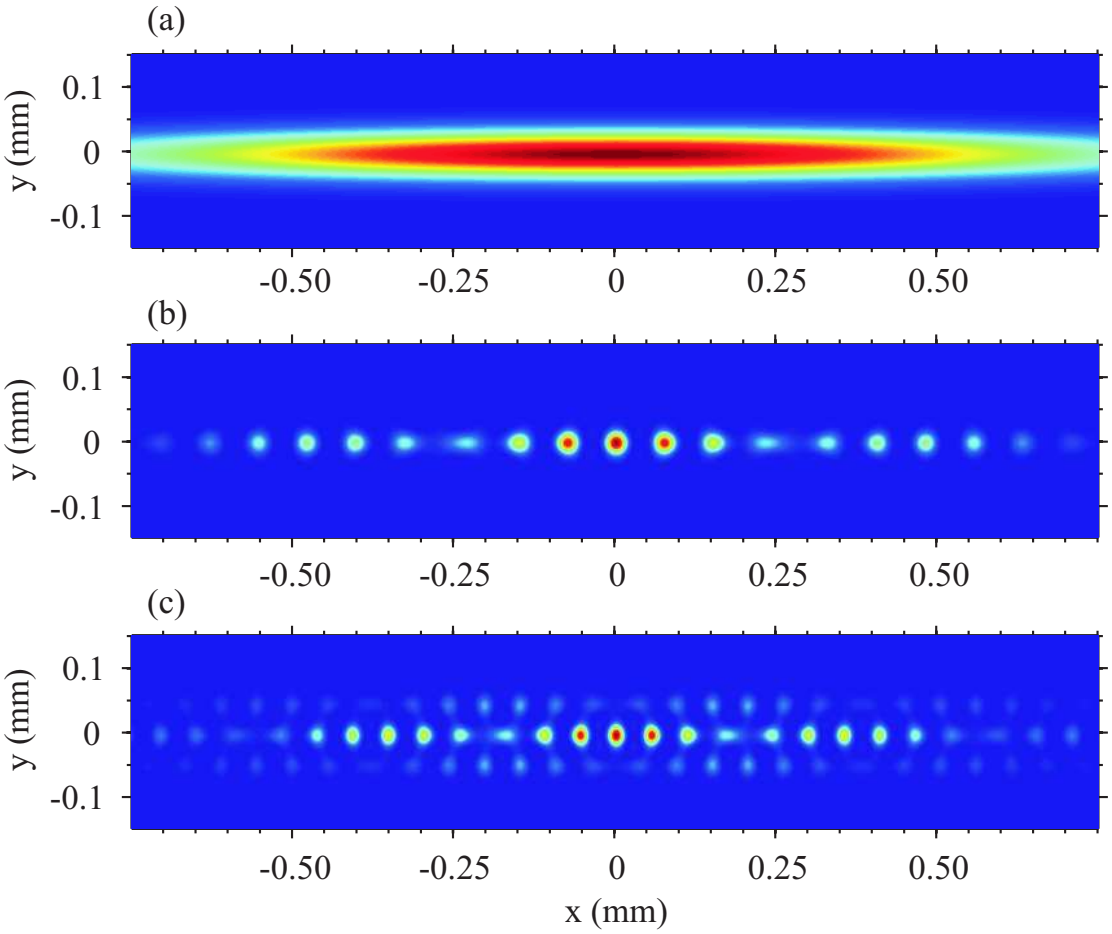

Figure 5.4: Numerical simulation using an analytical model: (a) input beam, (b) filament array formed at $I_0 = 90$ GW/cm^2 and (c) $I_0 = 170$ GW/cm^2.

5.3 Comparison of theoretical model and 2D numerical simulation results

For a qualitative comparison of the experimental data, numerical simulations and the results obtained using an analytical model, in Fig. 5.5 plot the period of the MF array *vs* the input beam intensity is presented. The data from the numerical model and the experiment coincide fairly well in the full range of the input intensities. It is worth mentioning that the MF period does not depend on the input beam ellipticity, defined as a_x/a_y, at least while the input beam ellipticity remains sufficiently large. In fact, these results suggest that the period of the MF array may be efficiently controlled via the input beam intensity. For what concerns the results obtained using an analytical model, the general trend closely follows the results obtained for the beam break-up in planar waveguides [122].

However, the results of analytical model notably depart from the experimental and numerical data in the low intensity limit ($30 - 60$ GW/cm^2), but fit the data well for high ($100 - 600$ GW/cm^2) input intensities. These differences could be explained by the fact that the analytical multistep four-wave mixing model does not account for the beam propagation, where the input beam experiences notable contraction due to self-focusing prior to break-up. As a result, the initial intensity at which the multistep four-wave parametric processes are triggered, remains undefined. However, a quantitative agreement between the data in the intensity range of $30 - 60$ GW/cm^2 could be achieved with scaling the input intensity in the analytical model by a factor of ~ 3, so as $I_0^{\mathrm{an}} = 3I_0^{\mathrm{exp}}$, which thus "compensates" for the intensity change due to the beam contraction. The resulting MF period after this adjustment is plotted by a bold dashed curve in Fig. 5.5. Conversely, in the high intensity limit, the input conditions are those that no beam contraction there occurs, and the results of the analytical model coincide very well with the numerical and experimental data.

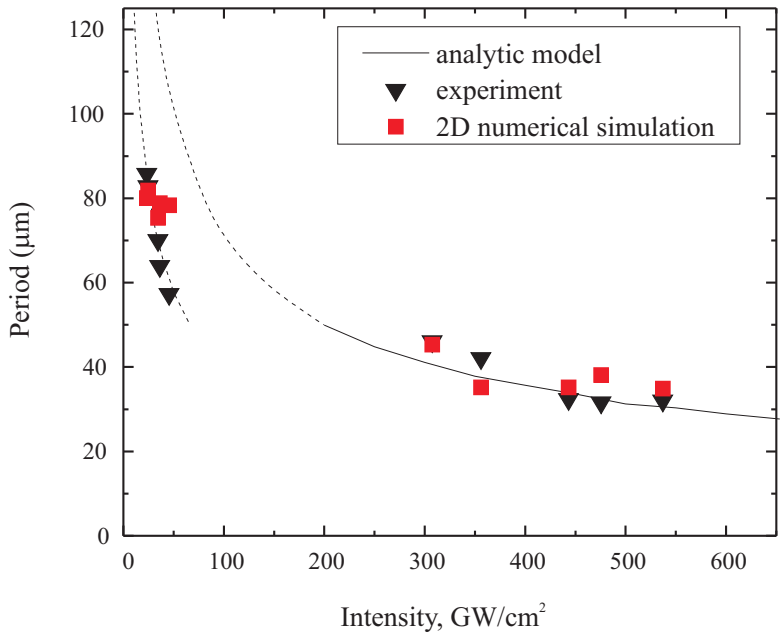

Figure 5.5: Period of the MF array *vs* the input beam intensity. Experimental data points are shown by solid triangles ▼, while the results of the numerical simulation are illustrated by ■. The results of the analytical model are plotted by curves, see text for details.

To summarize the results of above, it was demonstrated that intense highly el-

liptical laser beam breaks-up into periodic one- and two dimensional arrays of light filaments. Although the multiple filamentation is initiated by random amplitude noise, it forms highly reproducible periodic MF patterns, whose periodicity may be easily controlled via the input beam intensity. On simple physical grounds the observed periodicity in the MF array could be understood within a simple analytical framework of phase-matched multistep degenerate four-wave parametric interactions. The periodic break-up of the elliptical input beam is initiated by noncollinear nearly degenerate four-wave parametric amplification of certain wave vectors, which fulfil the phase-matching condition. The intensity dependence of the period in the MF array is explained as due to modification of the phase-matching condition by self- and cross-phase-modulation via nonlinear refractive index. The results of the analytical model well explain the experimental and numerical data at high input intensity and short nonlinear medium length, where the initial beam does not undergo contraction dynamics. The model is still feasible in explaining the results of the MF pattern formation in long samples with lower input intensity, however, a correction on the input beam intensity and diameter should be applied.

5.4 3D spatio-temporal analysis of the multiple filament arrays formation

Although a significant progress in control and regularization of the MF arrays has been achieved in practice, many aspects of the spatiotemporal dynamics, which takes place within the MF array in dense dispersive media, are still poorly investigated. The knowledge of temporal, and more generally speaking, spatiotemporal behavior of the individual light filaments comprising the MF array is vital for understanding and optimization of the energy deposition in light and matter interactions. Therefore the aim of this section is to study the spatiotemporal dynamics that emerges in the MF regime, set by self-focusing of femtosecond elliptical laser beams in fused silica. Experimentally high resolution reconstruction

of spatiotemporal intensity profiles of the light pulses within the entire MF array can by done by three dimensional mapping technique [123] using ultrashort (30 fs) pulses. For numerical investigation of MF generation a numerical model that qualitatively reproduces the experimental results and helps to identify some of the key physical mechanisms behind the space-time dynamics of multiple filamentation process was developed.

The study of experimental and numerical spatiotemporal dynamics of the multiple filament arrays excited by self-focusing of intense elliptical laser beams in fused silica will be presented in sections 5.5 and 5.6. Results demonstrate that although multiple filament arrays emerge as apparently regular patterns in the space domain, the spatiotemporal dynamics of the individual filaments is governed by the input-beam power and the input-beam ellipticity. In the case of moderate input-beam ellipticity, the individual filaments propagate in curved trajectories arising from skewed (spatiotemporal) coherence. The spatiotemporal propagation dynamics is regularized by increasing the input-beam ellipticity, and in part due to permanent modifications of fused silica that occur under intense irradiation. In this case, strong pulse reshaping and shock-front generation is observed, which yields a regular array of very short (< 5 fs) superluminally propagating localized peaks in the leading front, followed by the sub-pulses centered on the input-pulse top, and trailed by subluminally propagating pulses with rather complex transverse intensity distribution.

5.5 3D numerical model

The propagation dynamics of the ultrashort-pulsed elliptical light beams in the nonlinear medium with cubic nonlinearity was studied using one-directional propagation equation for the linearly polarized wave with the complex envelope $A(t, x, y, z)$:

$$\frac{\partial A}{\partial z} + \int\int\int_{+\infty}^{-\infty} T(t', x', y')A(t - t', x - x', y - y', z)dx'dy'dt' = \frac{i\omega_0 n_2}{c}|A|^2 A - \frac{\beta^{(K)}}{2}|A|^{2K-2}A - \frac{\sigma}{2}(1 + i\omega_0\tau_c)\rho A, \quad (5.17)$$

where z is the propagation variable, t is the temporal coordinate corresponding to the frame of reference moving with the GV of the pulse $v_g = \frac{\partial\omega}{\partial k}\big|_{\omega_0}$, ω_0 is the carrier frequency, $k(\omega) = \omega n(\omega)/c$ is the wave number, $k_0 = k(\omega_0)$, n and n_2 are the linear and nonlinear refractive indexes, respectively, c is the speed of light in vacuum, K is the order of the MPA, $\beta^{(K)}$ is the MPA coefficient, ρ is the free electron density, σ is the cross-section for electron-neutral inverse bremsstrahlung and τ_c is the electronic collision time in the conduction band. The evolution of the wave envelope due to diffraction and material dispersion was accounted via "medium response" function:

$$T(t, x, y) = \int\int\int_{+\infty}^{-\infty} D(\Omega, k_x, k_y) \exp\big[-i(\Omega t - k_x x - k_y y)\big] d\Omega dk_x dk_y, \quad (5.18)$$

where $\Omega = \omega - \omega_0$ is the frequency detuning from the carrier frequency, and k_x and k_y are the transverse components of the wavevector. Eq.5.17 was solved using the split step method, accounting for full material dispersion and diffraction in the non-paraxial case through a parameter

$$D(\Omega, k_x, k_y) = \sqrt{k(\omega_0 + \Omega)^2 - k_x^2 - k_y^2} - k_0 - \frac{\Omega}{v_g}, \quad (5.19)$$

which describes the spectral phase shift. The dynamics of the free electron density was assumed is contributed by the multiphoton and avalanche ionization only, neglecting electron diffusion and recombination terms owing to a sufficiently long lifetime of the electron plasma (170 fs [124]), which exceeds the input-pulse dura-

tion. The evolution equation for the electron density is then given by

$$\frac{\partial \rho}{\partial t} = \frac{\beta^{(K)}}{K\hbar\omega_0}|A|^{2K} + \frac{\sigma}{E_g}\rho|A|^2, \tag{5.20}$$

where E_g denotes the medium bandgap. The cross-section for inverse bremsstrahlung reads as

$$\sigma = \frac{e^2\tau_c}{cn_0\epsilon_0 m(1+\omega_0^2\tau_c^2)}, \tag{5.21}$$

where $m = 0.635m_e$ is the reduced electron-hole mass. The calculations were performed for $t_p = 130$ fs pulses with central wavelength $\lambda_0 = 800$ nm, using the following relevant parameters of the fused silica: $n_0 = 1.45$ and the full dispersion relation from [125], $n_2 = 2.8 \times 10^{-16}$ cm^2/W [126], $E_g = 7.8$ eV, and $K = 6$, assuming a single photon energy $\hbar\omega_0 = 1.5$ eV. The parameters of the electron plasma were evaluated using the formalism described in [127], which yielded the six photon absorption coefficient $\beta^{(6)} = 1.1 \times 10^{-66}$ cm^9/W^5 and $\sigma = 7.3 \times 10^{-22}$ m^2, taking the electronic collision time in the conduction band $\tau_c = 1.7$ fs [124].

The input-pulse was defined as an elliptical Gaussian beam characterized by FWHM beam widths a_x and a_y along x and y axes, respectively, and by FWHM pulse duration t_p:

$$A(t, x, y, z = 0) = A_0 \exp\left[-2\ln 2\left(\frac{t^2}{t_p^2} + \frac{x^2}{a_x^2} + \frac{y^2}{a_y^2}\right)\right]. \tag{5.22}$$

The calculations were performed by adding 5% intensity noise to the input beam. We note that the numerical simulations allowed only qualitative comparison between the numerical and experimental data: the period of the simulated MF array and the diameter of the individual filaments were smaller by a factor of $2 \div 4$, as compared to the experimentally measured values. This issue will be discussed in more detail the next section. Nevertheless, the numerical simulations enabled capturing the propagation dynamics (versus z) and corresponding spatiotemporal evolution of the MF array in detail, as well as calculation of the

spatiotemporal spectra, whose intensity range extends over more than 6 orders of magnitude and therefore not possible to measure experimentally.

And finally, intensity cross-correlation function of the output (test) pulses with 30-fs probe pulses via sum-frequency generation process was simulated, as it was performed in the experiment. Therefore we have calculated the intensity cross-correlation function between the test pulse at the output of the fused silica sample $I_t(t, x, y, z = L)$, where L is the sample length, and 30-fs Gaussian probe pulse:

$$I_{cc}(t, x, y) = \int I_t(t, x, y) I_p(t - \tau, x, y) d\tau = \frac{1}{2\pi} \int S_t(\Omega, x, y) \exp\left(-\frac{\Omega^2 \tau_p^2}{16 \ln 2}\right) \exp(-i\Omega t) d\Omega, \tag{5.23}$$

where $I_{cc}(t, x, y)$ is the cross-correlation intensity (intensity of the sum-frequency signal), $S_t(\Omega, x, y)$, is the power spectrum of the test pulse, τ_p is the probe pulse duration, and τ is the time delay.

5.6 Numerical modeling results of modulation instability driven multifilamentation

In the experiment, formation of the MF arrays was investigated in two particular cases: using moderate ($a_y/a_x = 3.5$) and high ($a_y/a_x = 6.8$) input-beam ellipticity. In the first case, the dimensions of the input beam at the input face of the fused silica sample were set as $a_x = 80$ μm and $a_y = 280$ μm ($a_y/a_x = 3.5$). The self-focusing dynamics of the elliptical light beams is well known from previous studies: an intense elliptical input-beam undergoes self-focusing in its shorter dimension (a_x) and eventually breaks-up into multiple filaments, arranged in a (quasi)periodic MF pattern along the longer dimension of the beam [113, 128]. With present experimental settings, a distinct MF array starts to emerge at the output of 20-mm fused silica sample with the input-beam energy of $E_{in} > 10$ μJ.

Figure 5.6 summarizes the experimental results obtained with the input-beams

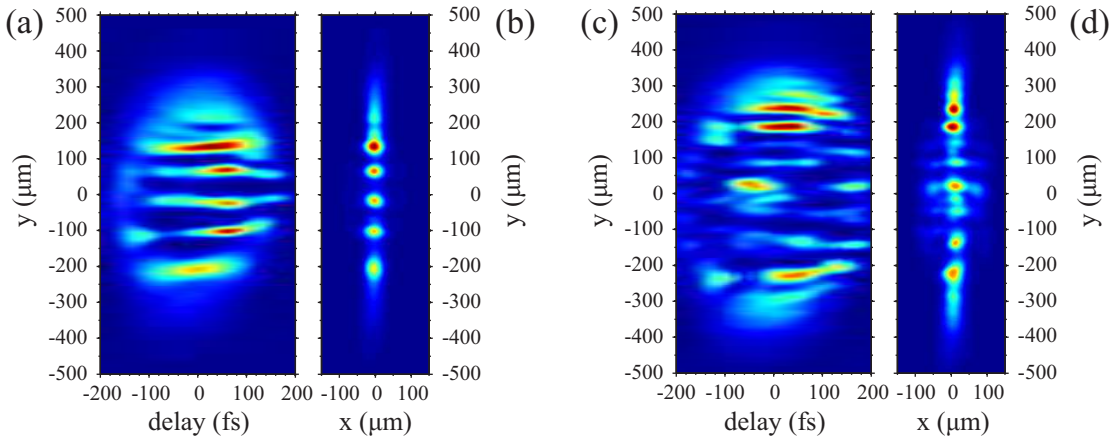

Figure 5.6: Central cross-section in the y-t plane of the experimentally measured spatiotemporal intensity distribution in the MF array, excited by (a) 12 μJ and (c) 14 μJ energy pulses with moderate input-beam ellipticity. Panels (b) and (d) show the corresponding time-integrated images.

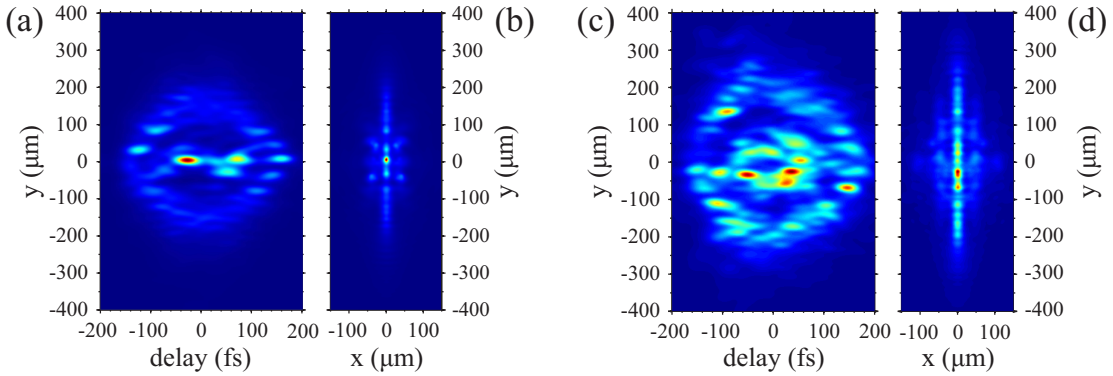

Figure 5.7: Numerically simulated intensity cross-correlation between the MF array and 30-fs probe pulse at different input-beam intensity: (a) $I_{in} = 200$ GW/cm^2, (c) $I_{in} = 250$ GW/cm^2. Panels (b) and (d) show the corresponding time-integrated images.

of moderate ellipticity. The central cross-section in the y-t plane of the spatiotemporal intensity profile of the MF array excited by $E_{in} = 12$ μJ pulses is illustrated in Fig. 5.6(a). Although the temporal reshaping of the pulses comprising the individual filaments is barely visible, the striking feature of the MF array is that the individual filaments propagate in curved trajectories. It is also interesting that the time integration of the full spatiotemporal intensity profile yields a periodic MF pattern, as illustrated in Fig. 5.6(b), which is familiar to that captured directly with the time-integrating CCD camera [128].

With slightly higher input energy ($E_{in} = 14$ μJ), the number of the individual filaments increases, the pulse break-up regime sets in, and the measured spatiotemporal intensity profile increases in complexity, as illustrated in Fig. 5.6(c). In this case, short temporal peaks emerge in the leading front (whose origin and features will be discussed later), while the remaining spatiotemporal intensity distribution acquires a complex shape and shows a superficial resemblance with the propagation of intense femtosecond pulses in air, in the so called optically turbulent regime [129], which recently has also been revealed from numerical simulations of the propagation of infrared and ultraviolet pulsed beams in fused silica [130]. The curvature of the individual filament trajectories becomes apparently three-dimensional, the time-integrated MF pattern becomes deteriorated; note how the centers of the individual filaments deviate from a straight central $x = 0$ line, as shown in Fig. 5.6(d).

The results of numerical simulation are presented in Fig. 5.7 and qualitatively reproduce the essential features observed experimentally: the curvature of the individual filament trajectories, occurrence of the short temporal peaks, and showing how the complexity of the spatiotemporal picture increases with increasing the input-beam energy. Also note, how these apparently irregular structures "merge" into quasi-regular MF patterns in the time-integrated representation. However, we note the marked differences in the period of the MF array and the diameter of the individual filaments, as obtained by the numerical simulations and measured

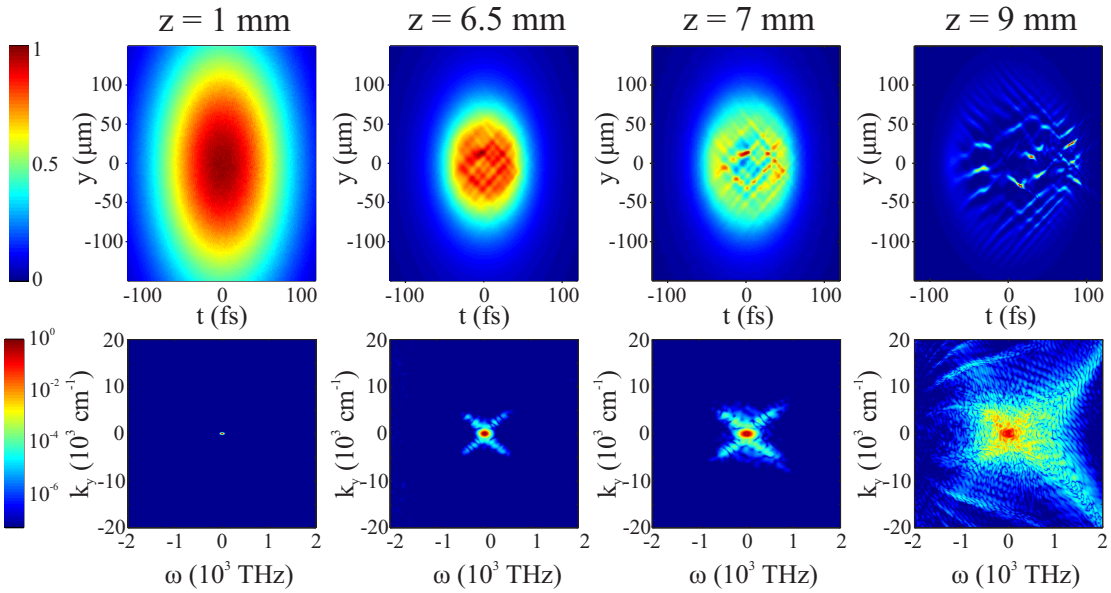

Figure 5.8: Numerically simulated evolution of (top panel) spatiotemporal intensity distribution in the y-t plane and (bottom panel) corresponding spatiotemporal spectrum of the self-focusing elliptical beam of moderate input-beam ellipticity at $I_{in} = 250$ GW/cm^2.

experimentally. For instance, by comparing the results depicted in Fig. 5.6(b) and Fig. 5.7(b), the experimental data suggests the MF period of 85 μm and FWHM diameter of the individual filament of 30 μm, whereas these values obtained from the numerical simulation are 30 μm and 5 μm, respectively. Indeed, in the earlier study [90], it was found that the filament diameter is intimately related to the nonlinear losses, which reflect the contribution of the MPA and electron plasma. However, there remains an unresolved problem of matching of these two quantities, as obtained from the simulation and from the experiment, because of the uncertainties in knowledge of the relevant plasma parameters and because of the limitations of the theoretical model itself. As a result, the differences in the filament diameter by a factor of 2 were obtained in the case of three and four photon absorption [90]. In the present case, the nonlinear losses associated with 6-photon absorption, therefore it is not surprising that the differences in relevant parameters characterizing the MF array are even larger.

Despite the aforementioned differences, the results of numerical simulation provide useful insights into formation dynamics of the MF array. Specifically, the origin of the curved filament trajectories may be interpreted in terms of so-called

hidden (or skewed) coherence between waves arising from nonlinear interactions [31]. These space-time trajectories rely on the phase-matching conditions and are featured by emergence of the X-shaped spatiotemporal spectrum, as recently demonstrated in the case of the three-wave parametric interactions [131, 132]. In our case, the governing process is the four-wave interaction. Indeed, the four-wave parametric interaction mediates the beam break-up [128] and generates the fields that are self-correlated along specific spatiotemporal trajectories as well. A closer look at the early spatiotemporal dynamics is presented in Fig. 5.8, where we plot the magnified portion of the numerically simulated spatiotemporal intensity distribution and its spatiotemporal spectrum as a function of the propagation distance z. Note, how the intensity modulation at the beam center manifests itself along specific lines, that are skewed with respect to y and t axes at $z = 6.5$ mm, and how these lines intensify and form a distinct "net-shaped" intensity modulation at $z = 7$ mm. At the same time, the corresponding spatiotemporal spectra develop a clearly distinguishable X-shaped profiles, whose arms are directed along the phase-matching lines. The increased intensity modulation (at $z = 9$ mm) provides centers of attraction, that precede formation of light filaments. On the other hand, the X-shaped spatiotemporal spectra are unambiguously linked to the X-wave formation in the filamentation regime [33], and therefore sets the link between formation of the MF array and X-wave generation.

In the second experiment, the dimensions of the input beam were set as $a_x = 90$ μm and $a_y = 610$ μm, producing high ($a_y/a_x = 6.8$) input-beam ellipticity. The threshold for emergence of the MF array in this case was found at $E_{in} = 48$ μJ. Figure 5.9(a) plots the measured spatiotemporal intensity distribution of the MF array excited with $E_{in} = 58$ μJ input pulses. It worth mentioning that in this case the experimental and numerical MF periods and filament diameters differ by a factor of 2. The emerging spatiotemporal picture exhibits much more regularity as compared with the picture discussed above. Specifically, the individual filaments experience well-distinguished temporal and spatial reshaping, trajectories

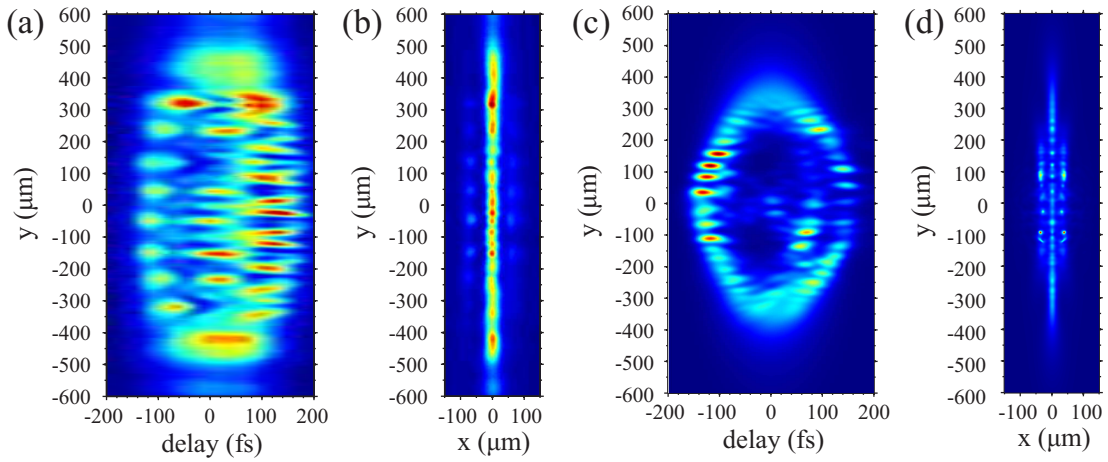

Figure 5.9: (a) Central cross-section in the y-t plane of the experimentally measured spatiotemporal intensity distribution and (b) time-integrated image of the MF array, excited by 58 μJ energy pulses with high input-beam ellipticity; (c), (d) show the corresponding cross-correlation data obtained by the numerical simulation with $I_{in} = 180$ GW/cm^2.

of the individual filaments are no longer curved, although skewed spatiotemporal substructures are still present at the beam periphery. Three distinct arrays of sub-pulses may be identified: very short superluminally (with respect to the GV of the input pulse) propagating localized peaks in the leading front, which are followed by longer sub-pulses centered on the input-pulse top, and trailed by subluminally propagating sub-pulses at the back front, which form fork-shaped spatiotemporal structures; see also the isointensity plot in Fig. 5.10, which is provided for illustrative reasons and clearly outlines the basic features. The experimental observations are qualitatively reproduced by the numerical simulations, illustrated in Figs. 5.9 (c) and (d).

By comparing Figs. 5.9 and 5.10 and taking into account the findings in early propagation dynamics, the emerging spatiotemporal dynamics within the MF array could be interpreted in terms of the interplay between the X-wave formation and development of shock-fronts, which are considered to play the key role in the single filament dynamics [30, 133]. At the leading front, very short, equally spaced (in the direction perpendicular to the propagation direction) localized peaks (the leading shock-fronts) line-up into a distinct temporal head of the MF array. The FWHM duration of each of the peaks was estimated from the cross-correlation

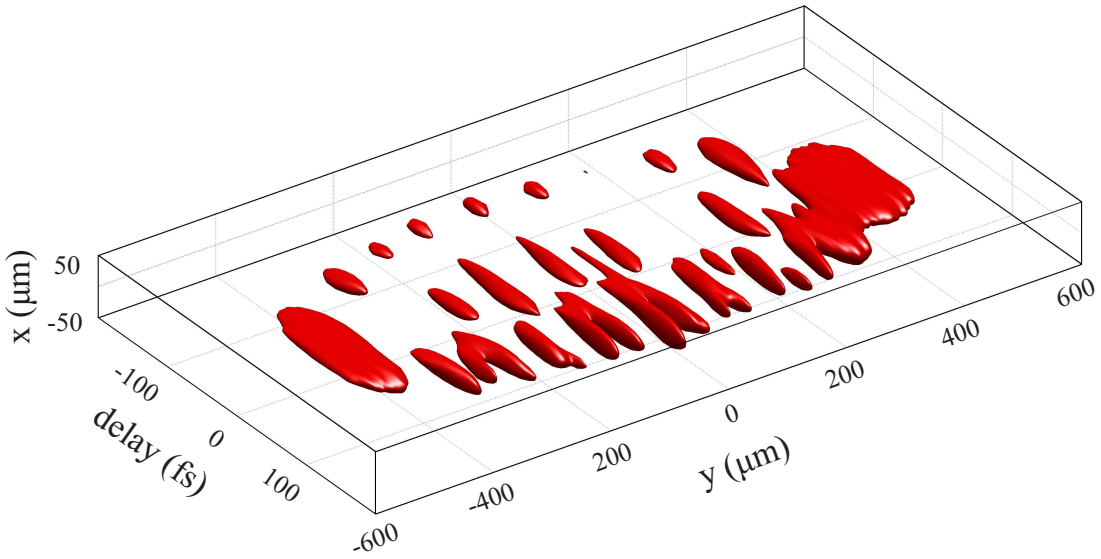

Figure 5.10: Spatiotemporal isointensity surface at 45% maximum intensity level of the MF array depicted in Fig. 5.9(a) and (b).

data and was found to be close to 30 fs, that corresponds to the length of the probe pulse itself. This indicates that the actual temporal width of the leading shock-fronts is much shorter. Indeed, their duration, as estimated from the numerical simulation, is close to 5 fs. These extremely short shock-fronts advance the input pulse (whose top is centered at t=0), and that is a clear signature of their superluminal propagation. Indeed, the superluminal propagation of the leading shock-fronts was recently captured in the single filament propagation regime in dense media with normal GVD by time-gated angular spectrum characterization [133], time-resolved optical polarigraphy [134] and shadowgraphy [135]. The leading shock-fronts experience strong self-compression and comprise an apparent bow-shaped front of the MF array: note, how the shortest and the most advanced peaks reside in the center of the beam, where the input-beam intensity is the highest and where the beam break-up and pulse splitting events occur first. Also note, how the pulse splitting is absent in the very periphery of the beam, where the input-beam intensity is the lowest.

The occurrence of distinct central sub-pulses at t=0 (at the top of the input-pulse), which are only marginally present in the numerical simulation, might be attributed to permanent structural change of fused silica under intense pulse ir-

radiation. Indeed, intense long-term irradiation at 1 kHz repetition rate induces permanent guiding channels with slightly higher refractive index due to material densification [136]. These channels trap and guide the radiation from the closest vicinity. To our opinion, the guiding effect also contributes to the "straightening" of the propagation trajectories of the individual filaments. Note also that skewed spatiotemporal structures still persist away from the beam center, as seen in Figs. 5.9(a) and (c).

At the trailing front, an array of subluminally propagating (and therefore delayed with respect to the input pulse top) shock-fronts are formed as well, however, with substantial differences as compared to the single filament dynamics. The complex trailing spatiotemporal structure is likely produced by a collective interplay between extended conical tails of the neighboring filaments, central subpulses and trailing shock-fronts and by electron plasma contribution. It is worth mentioning that this structure is two dimensional and is located only at the center of the y-t plane, as evident from the isointensity plot in Fig. 5.10. Note also, how these complex trailing formations blur the time-integrated MF pattern, as seen from Figs. 5.9(b) and (d). Yet, exact physical mechanisms responsible for the formation of complex trailing spatiotemporal part in the MF array are still pending to be disclosed.

5.7 Conclusions

In conclusion, experimental and numerical investigation of the spatiotemporal behavior of the MF arrays excited by intense elliptical laser beams in fused silica revealed a number of interesting features. Although intense elliptical input-beams carrying femtosecond light pulses break-up into regular and quasi-periodic MF patterns in the space domain, the spatiotemporal behavior of the individual filaments exhibits surprising features, which depend on the input-beam ellipticity and power. In the case of moderate input-beam ellipticity, the individual filaments propagate in curved trajectories and form complex spatiotemporal struc-

tures, which resemble optically turbulent propagation. These features originate from skewed (spatiotemporal) coherence arising in phase-matched four-wave interactions within self-focusing elliptical light beam. Conversely, the input-beams with high ellipticity break-up into (quasi)regular spatiotemporal patterns, featuring a distinct bow-shaped temporal head of the MF array, composed of extremely short peaks, which originate from the interplay between the X-wave and shock-front formation, and share many common with the single filament dynamics. In particular, extremely short ($\sim$ 5 fs) and localized (FWHM width of 20 μm) shock-fronts at the leading edge propagate at superluminal velocity with respect to the GV of the input pulse. Each individual filament in the MF array is almost a replica of its neighbor, just with different temporal position of the leading shock-front, indicating when, earlier or later, the pulse splitting event occurs as a function of the local input-beam intensity. The trailing spatiotemporal part of the MF array reveals a number of specific features, that are likely promoted by collective interactions among weak and extended conical tails of the neighboring filaments, central sub-pulses, trailing shock-fronts and by electron plasma contribution. It is interesting to note, that MF array period closely follows theoretically predicted through four wave mixing process Fig. 5.11, only the period has to be multiplied by two. Also the diameter of the filament is too times smaller than in experiment. The difference factor two in numerical and experimental filament diameters which are formed in water is common [90].

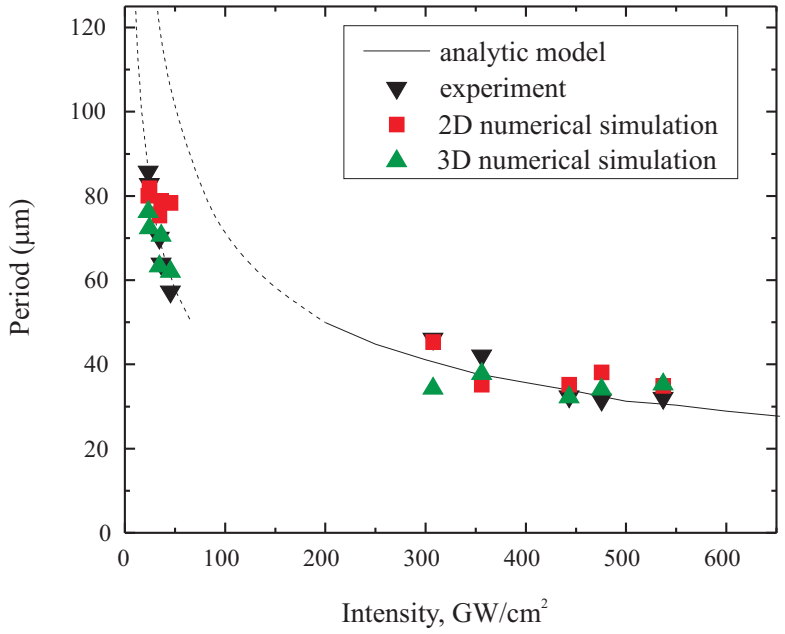

Figure 5.11: Period of the MF array *vs* the input beam intensity. Experimental data points are shown by solid triangles ▼, while the results of the 2D numerical simulation are illustrated by ■ and 3D numerical simulation are illustrated by ▲. The results of the analytical model are plotted by curves, see text for details.

And finally, our findings might be of use by providing useful hints for better understanding and optimization of light and matter interactions, concerning energy localization and deposition processes in dense dispersive media in particular; the knowledge that is on demand for many practical applications.

Chapter 6

Extreme events and Rogue waves in a bulk Kerr media

Material related to this thesis chapter was published in [A4,A5,A6] and [C9,C11]

Rogue or freak waves are well known in hydrodynamics, referring to statistically rare giant waves that occur on the surface oceans and seas, see for instance [137] for a review. From a general point of view, rogue waves, or more generally, rogue (extreme) events represent an extreme sensitivity of the nonlinear system to the initial conditions. Indeed, recently rogue-wave-like behavior was shown to be inherent to diverse nonlinear physical environments: propagation of acoustic waves in superfluid helium [138], variation of local atomic density in Bose-Einstein condensates [139], ion-acoustic and Alfvén wave propagation in plasmas [140], and propagation of acoustic-gravity waves in the atmosphere [141].

As it was mentioned rogue or extreme events (frequently termed rogue waves) are rare high-amplitude events, observed in various physical systems, where nonlinear wave interactions take place [142]. The occurrence probability of rogue events is described by so-called extreme-value or heavy-tailed (L-shaped) statistical distribution, which suggests that events with very high amplitude (as compared to the mean value) occur much more frequently than could be expected from normal-value (Gaussian) statistics. A considerable progress in understanding the rogue waves in hydrodynamics and optics has been achieved thanks to close analogy between the underlying physical mechanisms that initiate rogue

wave formation [143, 144]. Optical rogue waves [145] are extensively studied in one-dimensional optical systems, i.e. photonic crystal fibers, where nonlinear light propagation gives rise to complex temporal behavior and spectral superbroadening. Here optical rogue waves manifest themselves as high amplitude red-shifted soliton pulses [145] and blue-shifted dispersive waves [146] that emerge from noise-seeded modulation instability, with soliton collisions identified as the main mechanism responsible for rogue wave formation [147]. The rogue-wave-like behavior in optical fibres was observed with different pulsewidths, ranging from continuous wave to picosecond and femtosecond pulses [148, 149, 150], and under a variety of operating conditions [151, 152, 153].

Extreme-value statistics are also inherent to various nonlinear optical systems, where dimensionality and nonlinear wave dynamics is more complex as compared to optical fibers: nonlinear optical cavities [154], nonlinear optical lattices [155], nonlinear waveguides [156] and ultrashort pulse filamentation [157]. The latter case is of particular interest, since it represents an ultimate regime of light and matter interaction, and the nonlinear dynamics is governed by the interplay of self-focusing and self-phase modulation, white-light continuum generation, diffraction, nonlinear absorption, free-electron plasma generation and space-time effects [58]. On the other hand, filamentation phenomena find a broad spectrum of applications, ranging from atmospheric analysis [78] to laser micromachining [158], and therefore the stability issues of the filaments are of primary importance.

More recently, rogue wave-like behavior was observed in bulk media, in the femtosecond filamentation regime in gasses (air) [157] and liquids (water) [11] and predicted to occur in even more complex regimes of propagation, such as multiple filamentation [130]. In contrast to optical fibres, where nonlinear dynamics takes place only in one (temporal) dimension, in the filamentation regime, the nonlinear wave interaction occurs in full three-dimensional space. Optical rogue waves in bulk media are therefore not linked to soliton dynamics and formation of particular soliton pulses with extreme characteristics; here, due to space-time

coupling, they emerge from modulational instability-mediated pulse splitting and energy redistribution in space and time, taking a form of the X waves [11], which are weakly localized nondiffractive and nondispersive wave packets spontaneously occurring in media with normal GVD [159, 30].

In this chapter the numerical model is presented, with afterward discussion on a class of optical rogue events, that occur in three-dimensional space geometries as distinct from the widely studied one- or two-dimensional systems. In three-dimensional space, strong space-time coupling may lead to emergence of rogue events that bear some specific features, namely, a trailing peak with a lower-than-average intensity albeit with a wider spectrum. We show that these extreme events are associated to X-wave formation in the normal group-velocity-dispersion regime, as opposed to the temporal solitons observed in the anomalous regime in optical fibres.

Many aspects of the White-Light Continuum (WLC) generation in thin (typically, of few-millimeter thickness) bulk media share a close similarity with the filamentation phenomena, since the threshold for white-light continuum generation almost coincides with the threshold for self-focusing and filamentation. The part of chapter 6 is dedicated to the statistical study of the WLC generation in a sapphire plate, which reveals that in the certain input-pulse energy interval the blue-shifted spectral components of the WLC exhibit large shot-to-shot intensity variations that obey extreme-value statistical distribution. The explanation of L shaped statistics of spectral intensity through pulse splitting, and the suppression of it through intensity clamping will be presented also.

6.1 Numerical model for rogue wave analysis

In order to quantitatively reproduce the experimental results and characterize the spatiotemporal structure of the extreme events the numerical simulations were used. The extended NLS equation was solved, which in the spectral domain reads

as

$$\frac{\partial S(\Omega, k_\perp)}{\partial z} + iD(\Omega, k_\perp)S(\Omega, k_\perp) = S_N(\Omega, k_\perp), \tag{6.1}$$

where z is the longitudinal coordinate, $\Omega = \omega - \omega_0$ is the frequency detuning from the carrier frequency ω_0, and $k_\perp$ is the transverse wave number. The function $D(\Omega, k_\perp)$ describes linear propagation and accounts for diffraction in the non-paraxial case, full dispersion for distilled water [160], and linear absorption:

$$D(\Omega, k_\perp) = \sqrt{k(\omega_0 + \Omega)^2 - k_\perp^2} - k_0 - \frac{\Omega}{\nu_g} - i\alpha(\Omega), \tag{6.2}$$

where $\nu_g = \frac{\partial \omega}{\partial k}|_{\omega_0}$ is the GV of the pulse, $k(\omega) = \omega n(\omega)/c$ is the wave number, $k_0 = k(\omega_0)$, and $\alpha(\Omega)$ is the absorption coefficient. The complex amplitude of the pulse $A(t, r, z)$ and $S(\Omega, k_\perp)$ are related via Fourier - Hankel transform:

$$A(t, r, z) = \int_{-\infty}^{+\infty} \int_0^{+\infty} S(\Omega, k_\perp) e^{i\Omega t} J_0(k_\perp r) k_\perp \, \mathrm{d}k_\perp \, \frac{\mathrm{d}\Omega}{2\pi}, \tag{6.3}$$

where t is the temporal coordinate corresponding to the frame of reference moving with the GV of the pulse and r is the radial coordinate. $S_N(\Omega, k_\perp)$ is the spectral representation of the nonlinear terms namely:

$$S_N(\Omega, k_\perp) = \int_{-\infty}^{+\infty} \int_0^{+\infty} N(t, r) e^{-i\Omega t} J_0(k_\perp r) r \, \mathrm{d}r\mathrm{d}t \tag{6.4}$$

where

$$N(t, r) = \frac{i\omega_0 n_2}{c}|A|^2 A - \frac{n_2}{c}\frac{\partial}{\partial t}(|A|^2 A) - \frac{\beta^{(K)}}{2}|A|^{2K-2} - \frac{\sigma}{2}(1 + i\omega_0\tau_c)\rho A. \tag{6.5}$$

The nonlinear term includes the instantaneous Kerr effect, self-steepening, multiple photon absorption, and the effect of free electron plasma.

6.2 Spatiotemporal rogue waves in femtosecond filamentation

The rogue wave generation was studied by filament generation in water. The bandgap of water is $E_g = 6.5$ eV and a single photon energy is $\hbar\omega_0 = 1.5$ eV (at 800 nm). That corresponds to MPA order $K = 5$. MPA coefficient was taken as $\beta^{(5)} = 1.1 \times 10^{-51}$ cm^7/W^4, the cross section for electron-neutral inverse bremsstrahlung was $\sigma = 4.7 \times 10^{-22}$ m^2, and the electronic collision time in the conduction band is $\tau_c = 3$ fs [90]. The values of $\beta^{(5)}$ and σ were evaluated using the formalism described in [127], the plasma dynamics was accounted for in the same manner as in [27], including multiphoton and avalanche ionization and neglecting electron diffusion and recombination owing to sufficiently longer lifetime of the electron plasma as compared to the pulse width [161]. Absorption coefficient values in the visible and infrared were combined using data from [162] and [163]. The calculations were performed for input Gaussian pulsed beam with 60 μm diameter, $t_p = 130$ fs FWHM pulsewidth, central wavelength $\lambda_0 = 800$ nm and the input-beam intensity of $I_0 = 133$ GW/cm^2. In order to simulate the output statistics, we have modified the input-beam by introducing 2% intensity noise, 0.5% phase noise and 0.3% energy noise. The noise has Gaussian distribution and was implemented using Box-Muller transform of uniformly distributed random numbers.

The occurrence of extreme events in the filamentation regime is readily observable in the extreme-value statistics of the spectral intensity, which exhibits characteristic L-shaped distribution. Fig. 6.1(a) illustrates the statistics of 3500 numerically simulated single-shot spectra. Multiple gray curves show the individual single-shot spectra, whose average spectral intensity profile is overplotted by a black curve. The widest and the narrowest spectra are highlighted by the red and blue curves, respectively.

A more detailed statistical analysis of these spectra is presented in Fig. 6.1 (b)

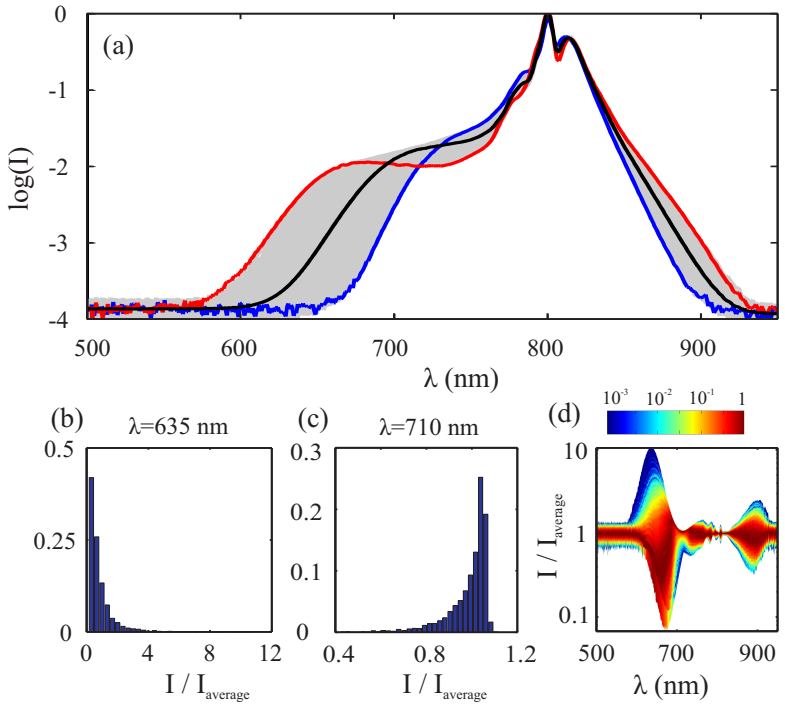

Figure 6.1: (a) The 3500 numerically simulated single-shot spectra (gray curves). The average spectrum is shown by the black curve, the widest and the narrowest extremes are highlighted by the red and blue curves. Frequency distributions of the spectral intensity at: (b) 635 nm, (c) 710 nm. (d) Statistics of the spectral intensity across the entire wavelength range.

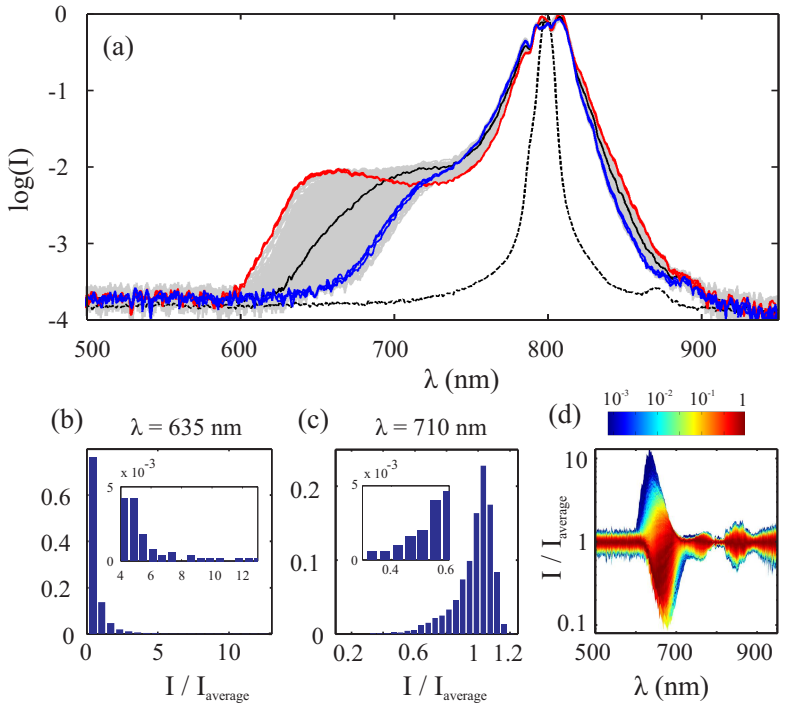

Figure 6.2: (a) The 5000 experimentally measured single-shot spectra of the filament (gray curves) recorded at 1.23 P_{cr}. Curve designations are the same as in Fig. 6.1(a), while the input spectrum is plotted by the dashed curve. Frequency distributions of the spectral intensity at: (b) 635 nm, (c) 710 nm. Insets show a magnified portion of the long tails. (d) statistics of the spectral intensity across the entire spectral detection range.

and (c) by plotting the frequency distribution of the spectral intensity at particular wavelengths of 635 nm and 710 nm, respectively. At 635 nm, the spectral intensity exhibits a clear right-tailed distribution. The spectral intensity of the most prominent extreme events is more than 10-20 times larger than the average. Interestingly, at 710 nm, the L-shaped distribution is left-tailed, i.e. showing that in the same dataset there is a number of events exposing small-intensity extremes. A closer look at Fig. 6.1(a) reveals that these marginal spectra have different shapes: those with the highest spectral intensity at 650 nm exhibit a dip around 710 nm, and vice versa. Hence, the observed statistics at different wavelengths is determined by the change of the spectral shape due to correlation between frequency components that occur in the self-phase modulation-induced spectral broadening [36]. Fig. 6.1(d) combines the statistics of the spectral intensity across the entire spectral detection range, where (logarithmic) color coding renders the normalized frequency of the spectral intensity at a particular wavelength. Notice that distinct extreme events occur mostly on the blue-shifted side of the spectrum.

Note here, that in the presentation of the numerical results, we have added an artificial noise at the level, which corresponds to experimental detection range of the fiber spectrometer. The numerical data fairly recovers all the essential statistical features captured experimentally. The statistical results obtained by the experimental measurements are shown in Fig. 6.2. Fig. 6.2(a) illustrates 5000 individual axial spectra, panels (b) and (c) show the statistical distributions of the spectral intensity at 635 and 710 nm, respectively, and which are summarized for the entire spectral range in panel (d).

The relevant question is how the extreme events in the spectral intensity manifest themselves in the space-time domain? In the fiber environment, rogue waves are associated with the red-shifted soliton pulses of extreme amplitude, which emerge in the region of anomalous group-velocity dispersion. However, the temporal dynamics in femtosecond filamentation is different: the spectral broadening

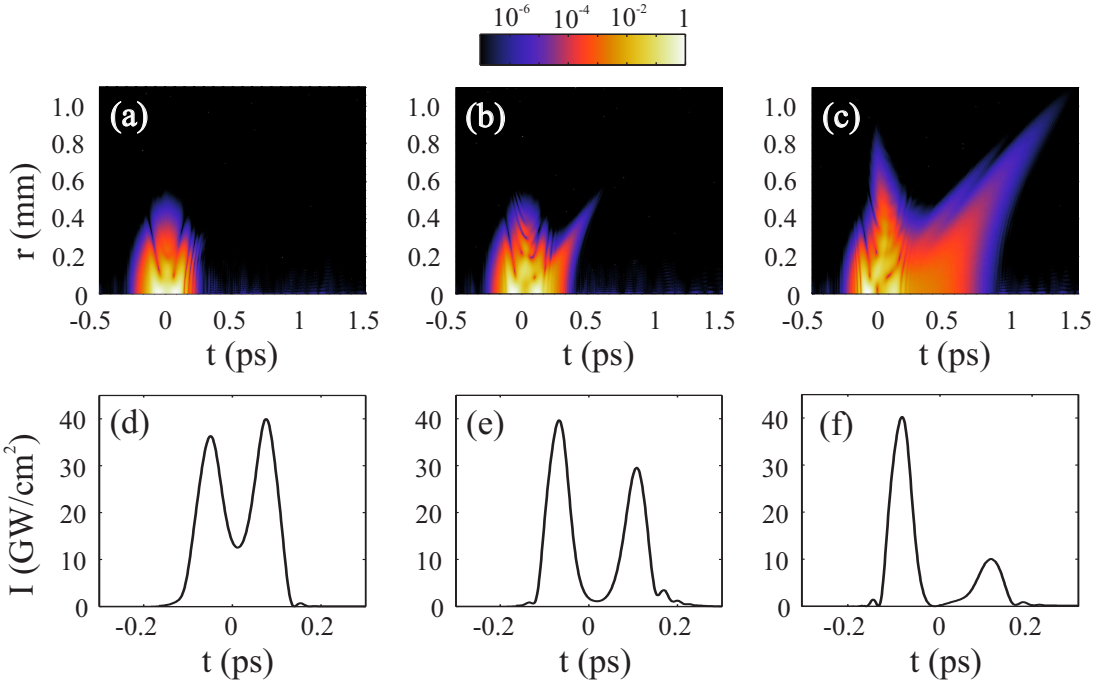

Figure 6.3: (Color online) (a)-(c) spatiotemporal and (d)-(f) on-axis intensity profiles corresponding to the spectra highlighted in Fig. 6.1(a). See text for details.

during self-focusing of the ultrashort light pulses in a medium with normal group-velocity dispersion is linked to pulse splitting and shock-front dynamics, where the leading shock-front is associated with the red-shifted axial radiation, and the trailing shock-front with the blue-shifted axial radiation [164]. A more general view of this concept was proposed in the framework of two split nonlinear X-waves, one traveling at subluminal and another at superluminal velocities with respect to the GV of the input Gaussian pulse, and whose localization is ensured by the off-axis, conical part of the beam (conical emission) [7, 30, 133].

Figures 6.3(a)-(c) show the numerically simulated spatiotemporal intensity distributions, that correspond to the narrowest, the average and the widest spectra, respectively, as highlighted in Fig. 6.1(a), indicating formation of the split X-waves. Panels (d)-(f) show the corresponding on-axis temporal intensity profiles, which highlight pulse splitting events and formation of optical shocks, that are recognized by weak and rapidly decaying oscillations at the pulse fronts. Notably, major differences between the three different cases are observed only in the trailing X-wave, whose spatiotemporal extent and on-axis intensity exhibit great

variability if compared with the leading peak.

6.3 The emergence and suppression of the rogue wave statistics

From more detailed statistical investigations carried out for WLC generation in sapphire by varying the input-pulse energy from 0.2 to 1 μJ, it was found that distinct L-shaped statistical distributions were characteristic just to spectral components in the blue edge of the WLC spectrum. Moreover, the L-shaped statistics were observed only within a narrow input-energy interval between 0.40 and 0.46 μJ, when the blue edge of the WLC was confined in the wavelength interval of $480 - 590$ nm. In order to quantitatively explain this finding, further examination of spectral broadening dynamics versus the input-pulse energy was performed. The measured average (over 2000 laser shots) wavelength of the WLC blue edge, which was detected at a fixed intensity level of $10^{-3.5}$ I_{max}, where I_{max} is the peak spectral intensity around 800 nm. The corresponding numerical simulations were performed using the numerical model, which solves the extended NLS equation, and which accounts for diffraction, dispersion, the instantaneous Kerr effect, self-steepening, 5-photon absorption, and the effect of free electron plasma, as described in detail in [11] and section 6.1. The noise was not included in the simulations, thus yielding fairly average values of the wavelength and peak intensity. The experimental and numerical data are compared in Fig. 6.4(a).

The experimentally measured non-Gaussian statistical distributions of the WLC spectral intensity at the blue edge were quantified by using a three-parameter Weibull fit function [147]:

$$f(x) = C\left(\frac{x - x_0}{l}\right)^{k-1} \exp\left(-\left(\frac{x - x_0}{l}\right)^{k}\right), \tag{6.6}$$

where k, l and x_0 are shape, scale and location parameters, respectively, and C is the normalization constant. The shape parameter k, which characterizes the skew-

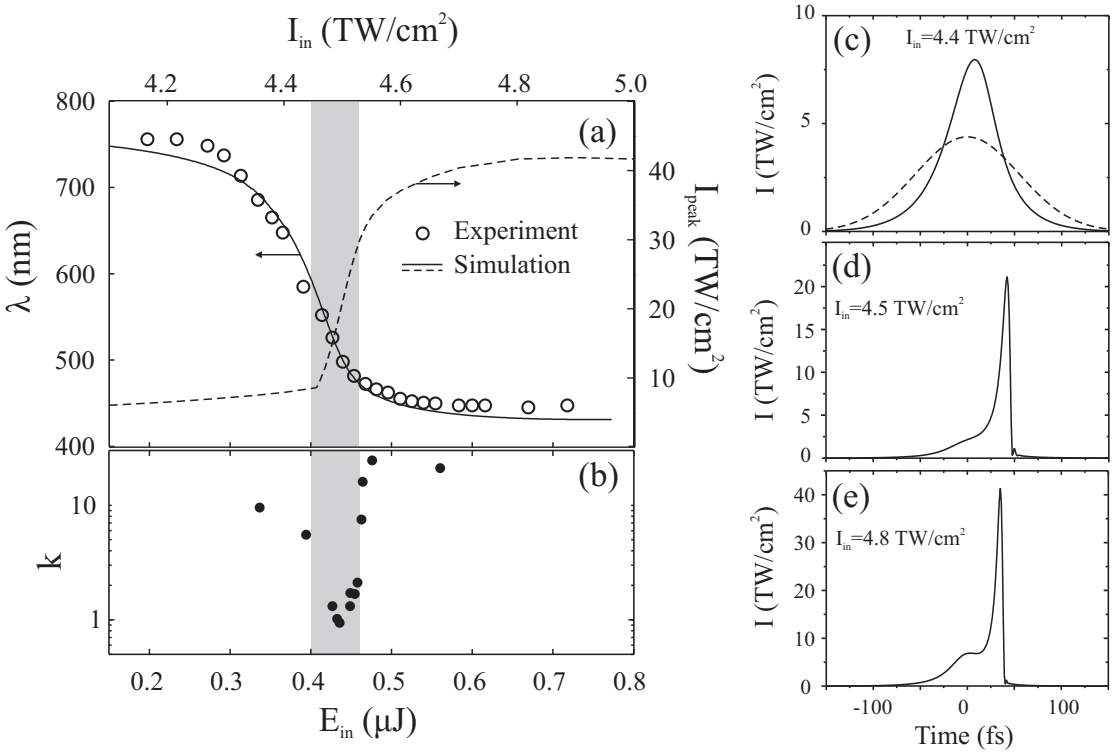

Figure 6.4: (a) Dynamics of the spectral broadening expressed as the wavelength of the blue edge. Dashed curve depicts the peak intensity inside the sapphire sample. (b) Shape parameter of the Weibull fit function vs input-pulse energy. Shaded area marks the energy (intensity) range where extreme-value statistics is detected. (c)-(e) Numerically simulated on-axis intensity profiles. Dashed curve shows the input-pulse.

ness of the statistical distribution is plotted in Fig. 6.4(b). Note that for nearly-symmetric distributions that were recorded at the lowest ($E_{in} < 0.3\mu J$) and at the highest ($E_{in} > 0.6\mu J$) input-pulse energies, the fit function given by Eq. 6.6 yielded high k-values, but also a large error, therefore these data points were not included in the plot. Summarizing the results illustrated in Figs. 6.4(a) and 6.4(b), we conclude that the dynamics of the spectral broadening undergoes three distinct stages, that are linked to the temporal dynamics of the pulse and resulting peak intensity inside the nonlinear medium, as shown by a dashed curve in Fig. 6.4(a), and where the blue-shifted spectral components of the WLC exhibit different statistical distributions. The initial WLC generation stage ($E_{in} = 0.28 - 0.40\mu$J) is mainly associated with self-phase modulation-induced almost symmetric spectral broadening, where no extreme-value statistics were detected. In the time domain, the pulse profile becomes gradually reshaped [Fig. 6.4(c)], however no

pulse splitting occurs yet. The second stage ($E_{in} = 0.40 - 0.46\mu$J) is related to an abrupt increase of the peak intensity, which clearly indicates the pulse splitting event. The spectral broadening is governed by highly asymmetric pulse splitting, pulse front steepening and generation of the shock-front at the trailing edge of the pulse, as shown in Fig. 4(d), which is consistent with WLC generation scenario [164]. On the other hand, the spectral broadening might be described in terms of four-wave mixing and occurrence of two split X waves in full three-dimensional space [30], whose mutual interaction provides suitable phase matching condition for generation of the blue-shifted spectral components. In this stage, the build-up of the intense trailing pulse (which may be called transient stage of WLC generation) strongly depends on the input-pulse intensity. In fact, this suggests that any small intensity variation (intensity noise) in the input beam has a large impact on the resulting peak intensity of the trailing pulse, thus giving rise to the observed rogue-wave-like statistical distribution. In the final stage of the WLC generation ($E_{in} > 0.46\mu$J), the spectral broadening markedly slows down and finally stops at $E_{in} = 0.55\mu$J as the intensity of the trailing pulse is clamped at $\sim 41TW/cm^2$ due to MPA (5-photon, in our case). The corresponding intensity profile is shown in Fig. 6.4(e). Here the dynamical picture settles and no extreme events occur. This in fact suggests that the intensity clamping acts as the mechanism, which suppresses occurrence of the extreme events. The extreme events therefore occur only within a narrow input-pulse energy (intensity) range, which is defined by the pulse splitting and intensity clamping.

6.4 Deterministic extreme events in femtosecond filamentation

It is proved both experimentally and numerically, that pulsed wavepacket undergoes rapid noise cleaning during self-focusing [165, 166, 167]. The high intensity spots and tiny phase variations (noise) become spatio-temporally diffused (due to combined action of dispersion, diffraction, nonlinearity and absorption). Due to

such smoothing of the wavepacket, the two input pulses with equal energy, but with different noise distribution, evolve into two distinct profiles having different intensity and energy, as shown in Fig. 6.5. The most drastic change occurs near the filamentation threshold. Since the pulses generated by laser possesses some variations of the envelope (even having identical energy), it leads to some wandering of the filament at the output.

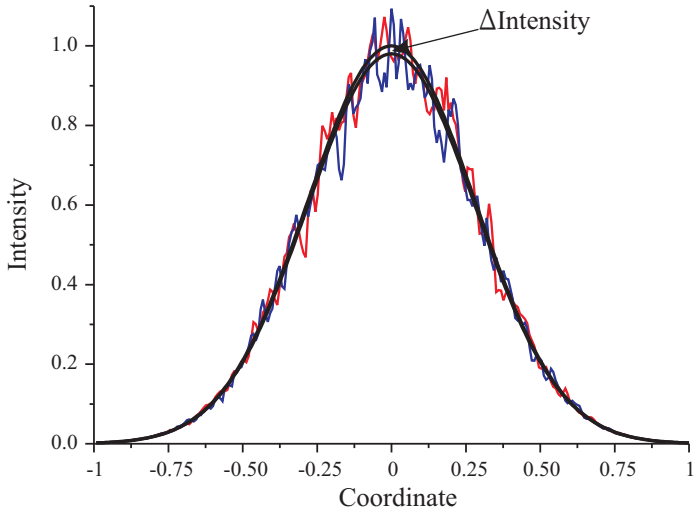

Figure 6.5: Blue and red lines present two initial pulse/beam intensity profiles having the same energy, but different random modulation. Two black lines show the intensity profiles which coincides to the integral energy remaining after noise cleaning by diffraction, dispersion, nonlinearity and absorption. Note the difference in intensities of the pulse profiles after noise cleaning.

The understanding, that energy is the main parameter which defines formation of the filament, supports the idea of the deterministic nature of the rogue events. In order to verify it we did several numeric experiments. In the first one, the large number of the filaments were formed (calculated) starting from clean Gaussian wavepackets, having different initial intensity but the same beam size and duration. Since the experimentally measured laser power fluctuations nearly correspond to the normal distribution, which is described by Gaussian probability density function, we also did calculations with the initial pulse intensity distributed accordingly to normal distribution. Four different cases corresponding to four different mean intensity value of the initial pulse (125 GW/cm^2, 130 GW/cm^2, 135 GW/cm^2, 140 GW/cm^2) were investigated. The standard variation

(variance) was the same in all cases. Results are presented in Fig. 6.6. It seems possible to get good coincidence with the experimental data statistics, and to demonstrate appearance of extreme events (L-shaped statistics) just by changing mean value i.e. the center of the Probability Density Function (PDF). In normal GVD region after the pulse splitting into two X waves filament becomes nearly formed, and extreme value statistics becomes evident both in red and blue part of the spectrum (see Fig. 6.6). Due to nonsymmetric pulse splitting the trailing blue-shifted pulse has much higher intensity than the leading red-shifted pulse. The refractive index dependence on intensity tunes phase matching conditions for the FWM process, therefore phase matching becomes possible within wide range of blue part of spectra and much less in the red part. So near the filament formation threshold the small variation of the input intensity ($< 1\%$) leads to appearance of huge variation of the output spectra, (especially in blue part) and appearance of the L-shaped probability distribution. The maximum of extreme events takes place at 130 GW/cm^2 mean input intensity value. At higher intensity the extreme value (L-shaped) statistics becomes suppressed (Fig. 6.6 (i)) due to intensity clamping [168, 169].

The proposed deterministic rogue event model is very versatile. It is possible to analyze the extreme event statistics not only by altering mean input intensity value (center of PDF), but also by changing intensity variation width (see Fig. 6.7). The increase of the standard deviation from 1 GW/cm^2 to 3 GW/cm^2 (see Fig. 6.7) induces the abrupt growth of the instabilities at the output. The statistical spectrum analysis (see Fig. 6.7 (e-g)) reveals the drastic increase in maximum reached deviation from average intensity value, and some shift to the blue side of the spectrum.

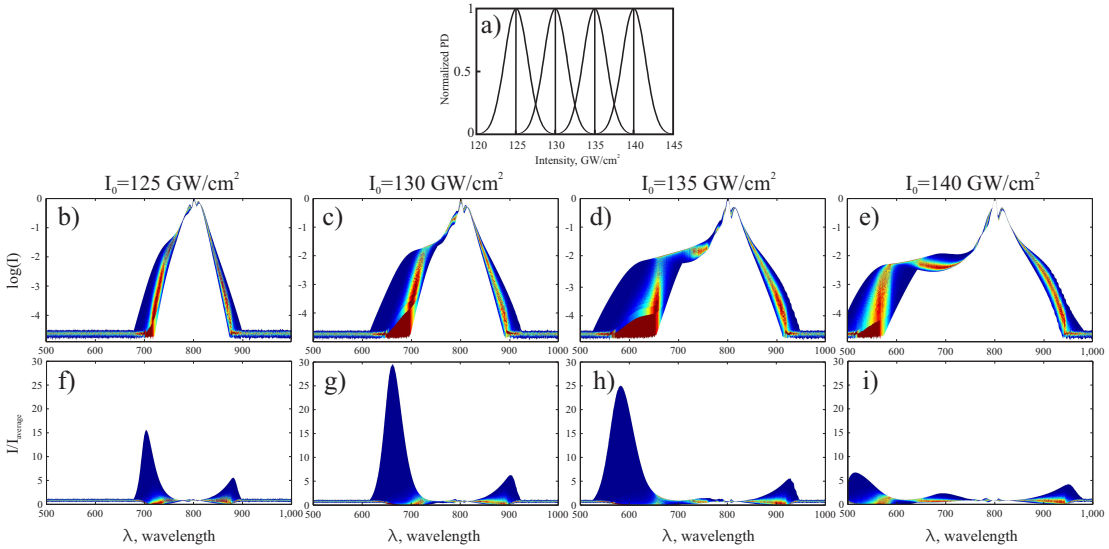

Figure 6.6: Filament on axis spectra variations (b-i) due to input wavepacket intensity variation. (a)Four cases of the input intensity distributions for four different mean intensity values (125 GW/cm^2, 130 GW/cm^2, 135 GW/cm^2, 140 GW/cm^2). Shifting of central PDF intensity (power) changes output filament spectrum. a) figure represents shifting of PDF. b, c, d, e shows the filament spectrum variance, while f, g, h, i - the change of spectral intensity statistics due to the shift of average intensity. Intensities were 125 GW/cm^2, 130 GW/cm^2, 135 GW/cm^2, 140 GW/cm^2 respectively. The variance was fixed at 2 GW/cm^2.

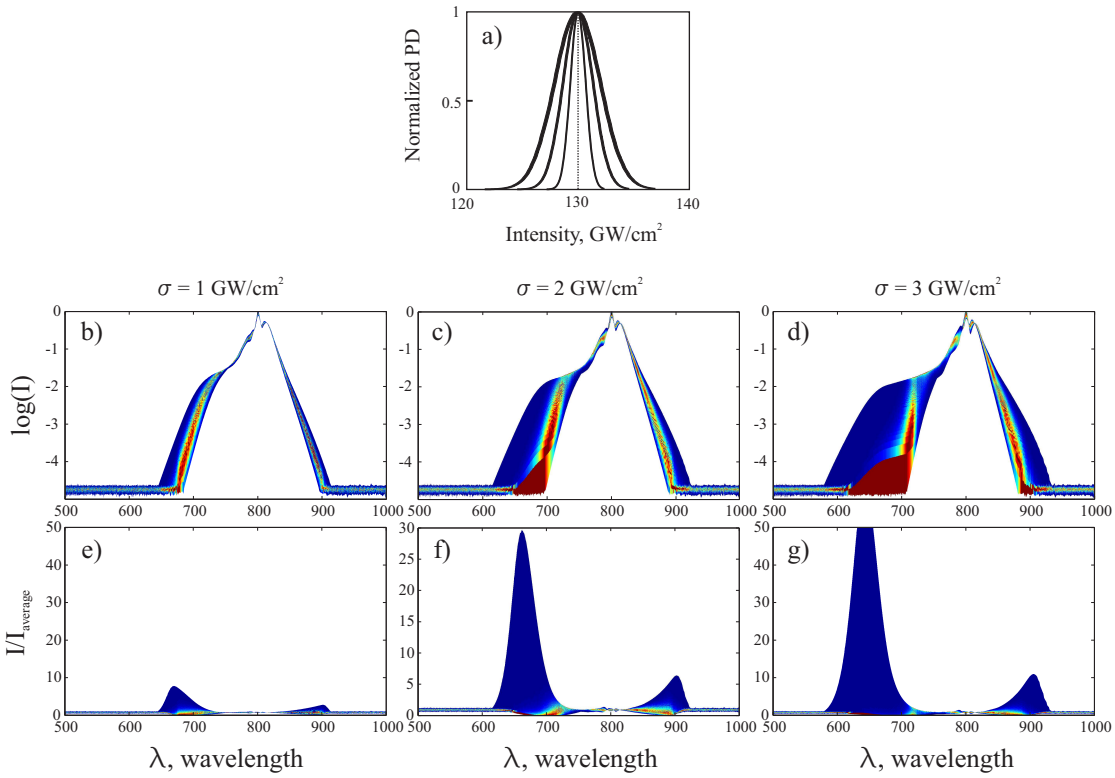

Figure 6.7: Filament on axis spectra variations (b-g) due to input wavepacket intensity variation. (a)Three cases of the input intensity distributions for three different intensity variances (1 GW/cm^2, 2 GW/cm^2 and 3 GW/cm^2). The widening of PDF changes output filament spectrum. a) figure represents widening of PDF. b, c, d shows the filament spectrum variance, while e, f, g - the change of spectral intensity statistics due to the altering of PDF variance. Variances were 1 GW/cm^2, 2 GW/cm^2 and 3 GW/cm^2 respectively. The average intensity was fixed at 130 GW/cm^2.

The main idea of the our deterministic model rests on the PDF transformation within nonlinear dynamic system. It also describes the PDF symmetrization and suppression of the extreme value statistics caused by intensity clamping effect (intensity saturation). Such scenario is common for many nonlinear systems. It was shown, recently, that the parametric amplifier within some parameter range shows L-shaped rogue-wave-like statistics which could be washed-out by saturating amplifier [168].

6.5 Conclusions

Under investigated experimental conditions, the extreme events in the femtosecond filamentation regime are identified as large *space-time coupled* intensity fluctuations and formation of an X-wave at the trailing edge of the input pulse. The results are significantly different with respect to one-dimensional fibre settings in which extreme events are associated to higher-than-average intensities. The three-dimensional extreme event needs to be visualized in full three-dimensional rather than in a reduced one-dimensional space: indeed, in Fig. 6.3(c) we immediately notice that the extreme event is associated to the clear formation of an X-wave with largely extended conical tail, i.e. of a truly space-time coupled, three-dimensional wave-packet. Due to the ubiquity of space-time coupled effects in three-dimensional systems the similar rogue X-wave formation and wave localization events in other settings involving e.g, acoustic [170] and even seismic waves [171] might be observed.

It was also demonstrated that the rogue-wave-like statistics of the spectral intensity of the WLC generated in a wide-bandgap solid (sapphire) are observed only in the transient stage of the WLC generation, and are associated with pulse splitting and build-up of intense trailing pulse, that strongly depend on the input-pulse intensity. The intensity clamping was found to be a mechanism which suppresses the occurrence of the extreme events. These findings also explain why the extreme events in WLC generation in bulk medium are observed only in a

narrow input-energy (intensity) interval.

The proposed rogue wave deterministic model based on the nonlinear transformation of the PDF, allowed to reveal the emergence of the rogue wave statistics. It was demonstrated, that the blue-shifted and red-shifted conical waves formed after the pulse splitting event are amplified via FWM process, when the intensity dependent phase matching transforms the normally distributed input to the L-shaped output.

Chapter 7

Conclusions

1. The Gaussian beam in nonlinear scattering medium reshapes into conical wave, namely, light filament and is capable to propagate distances over many Rayleigh range. It is shown that light scattering introduced by the polystyrene microspheres shifts the nonlinear focus (emergence of the filament) toward further propagation distance, and results in somewhat larger filament diameter along with appearance of speckle structure in the peripheral part of the beam.

2. It is demonstrated that intense highly elliptical laser beam breaks up into periodic one- and two-dimensional arrays of light filaments. Although the multiple filamentation is initiated by random amplitude noise, it forms highly reproducible periodic multiple filaments patterns, whose periodicity may be easily controlled via the input beam intensity. The observed periodicity in the multiple filaments array could be understood within a simple analytical framework of phase-matched multistep degenerate four-wave parametric interactions. The periodic breakup of the elliptical input beam is initiated by noncollinear nearly degenerate four-wave parametric amplification of certain wave vectors, which fulfil the phasematching condition. The intensity dependence of the period in the multiple filaments array is explained as due to modification of the phase-matching condition by self-phase and cross-phase modulation via nonlinear refractive index.

3. The spatiotemporal behavior of the individual filaments exhibits specific features,which depend on the input-beam ellipticity and power. In the case of moderate input-beam ellipticity, the individual filaments propagate in curved trajectories and form complex spatiotemporal structures, which resemble optically turbulent propagation. This small scale intensity structure originates from skewed (X-shaped) coherence arising in phase-matched four-wave interactions. The input beams with high ellipticity break up into (quasi) regular spatiotemporal patterns, featuring a distinct bow-shaped spatiotemporal head of the multiple filaments array, composed of extremely short peaks, which originate from the interplay between the X-wave and shock-front formation, and share many commonalities with the single filament dynamics.

4. The extreme events in the femtosecond filamentation regime are identified in the spectral domain, as either large or small extremes of the spectral intensity, justified by right- or left-tailed statistical distributions, respectively. In the time domain, the observed extreme events are associated with pulse splitting and energy redistribution in space and manifest themselves as large space-time coupled intensity fluctuations due to formation of X waves.

5. The rogue-wave-like statistics of the spectral intensity of the supercontinuum generated in a wide-bandgap solid are observed only in the transient stage, and are associated with pulse splitting and build-up of intense trailing conical wave, that strongly depend on the input-pulse intensity. The intensity clamping is found to be a mechanism which suppresses the occurrence of the extreme events. These findings also explain why the extreme events generation in bulk medium are observed only in a narrow input-energy (intensity) interval.

6. The appearance of the rogue wave statistics could be understood within the deterministic model based on nonlinear transformation of the probability density function.

Bibliography

[1] M. Hercher. Laser-induced damage in transparent media. *J. Opt. Soc. Am.*, 54:563, 1964.

[2] A. Braun, G. Korn, X. Liu, D. Du, J. Squier, and G. Mourou. Self-channeling of high-peak-power femtosecond laser pulses in air. *Opt. Lett.*, 20(1):73–75, 1995.

[3] R. Y. Chiao, E. Garmire, and C. H. Townes. Self-trapping of optical beams. *Phys. Rev. Lett.*, 13(15):479–482, 1964.

[4] V. N. Lugovoi and A. M. Prokhorov. A possible explanation of the small-scale self-focusing filaments. *JETP Lett.*, 7(5):117–119, 1969.

[5] M. Mlejnek, E. M. Wright, and J. V. Moloney. Dynamic spatial replenishment of femtosecond pulses propagating in air. *Opt. Lett.*, 23(5):382–384, 1998.

[6] M. Mlejnek, E. M. Wright, and J. V. Moloney. Femtosecond pulse propagation in argon: a pressure dependence study. *Phys. Rev. E*, 58(4):4903–4910, 1998.

[7] M. Kolesik, E.M.Wright, and J.V. Moloney. Dynamic nonlinear xwaves for femtosecond pulse propagation in water. *Phys. Rev. Lett.*, 92(25):253901, 2004.

[8] M. Kolesik, E.M.Wright, and J.V. Moloney. Interpretation of the spectrally resolved far field of femtosecond pulses propagating in bulk nonlinear dispersive media. *Opt. Express*, 13(26):10729–10741, 2005.

[9] A. Dubietis, E. Gaižauskas, G. Tamošauskas, and P. Di Trapani. Light filaments without self-channeling. *Phys. Rev. Lett.*, 92(25):253903, 2004.

[10] A. Dubietis, E. Kučinskas, G. Tamošauskas, M. A. Porras E. Gaižauskas, and P. Di Trapani. Self-reconstruction of light filaments. *Opt. Lett.*, 29(24):2893, 2004.

[11] D. Majus, V. Jukna, G. Valiulis, D. Faccio, and A. Dubietis. Spatio-temporal rogue events in femtosecond filamentation. *Phys. Rev. A*, 83:025802, 2011.

[12] R.W. Boyd, S. G. Lukishova, and Y.R. Shen. *Self-focusing: Past and Present: Fundamentals and Prospects (Topics in Applied Physics)*. Springer Berlin / Heidelberg, USA, 2009.

[13] C.-W. Chen, J.-L. Tang, K.-H. Chung, T.-H. Wei, and T.-H. Huang. Negative nonlinear refraction obtained with ultrashort laser pulses. *Opt. Express*, 15(11):7006–7018, 2007.

[14] R. Y. Chiao, E. Garmire, and C. H. Townes. Self-trapping of optical beams. *Phys. Rev. Lett.*, 13(15):479 – 482, 1964.

[15] E. L. Dawes and J. H. Marburger. Computer studies in self-focusing. *Phys. Rev.*, 179(3):862–868, 1969.

[16] J. H. Marburger. Self-focusing: theory. *Prog. Quantum Electron.*, 4:85–110, 1975.

[17] A. Couairon, E. Brambilla, T. Corti, D. Majus, O. de J. Ramrez-Gngora, and M. Kolesik. Practitioner's guide to laser pulse propagation models and simulation. numerical implementation and practical usage of modern pulse propagation models. *Eur. Phys. J. Special Topics*, 199:5–76, 2011.

[18] G. Fibich and G. C. Papanicolaou. Self-focusing in the perturbed and unperturbed nonlinear schrödinger equation in critical dimension. *SIAM J. Appl. Math.*, 60(1):183–240, 1999.

[19] B. J. LeMesurier. Dissipation at singularities of the nonlinear schrdinger equationthrough limits of regularisations. *Physica D*, 138:334–343, 2000.

[20] N. A. Zharova, A. G. Litvak, T. A. Petrova, A. M. Sergeev, and A. D. Yunakovskii. Multiple fractionation of wave structures in a nonlinear medium. *JETP Lett.*, 44(1):13–17, 1986.

[21] A. Couairon. Dynamics of femtosecond filamentation from saturation of self-focusing laser pulses. *Phys. Rev. A*, 68:015801, 2003.

[22] G. Fibich and G. C. Papanicolaou. Self-focusing in the presence of small time dispersion and nonparaxiality. *Opt. Lett.*, 22(18):1379–1381, 1997.

[23] G. Fibich and B. Ilan. Deterministic vectorial effects lead to multiple filamentation. *Opt. Lett.*, 26(11):840–842, 2001.

[24] G. Fibich and B. Ilan. Vectorial and random effects in self-focusing and in multiple filamentation. *Physica D*, 157:112, 2001.

[25] O. Jedrkiewicz, A. Picozzi, M. Clerici, D. Faccio, and P. Di Trapani. Emergence of x-shaped spatiotemporal coherence in optical waves. *Phys. Rev. Lett.*, 97:243903, 2006.

[26] O. Jedrkiewicz, M. Clerici, A. Picozzi, D. Faccio, and P. Di Trapani. X-shaped space-time coherence in optical parametric generation. *Phys. Rev. A*, 76:033823, 2007.

[27] D. Majus, V. Jukna, G. Tamošauskas, G. Valiulis, and A. Dubietis. Three-dimensional mapping of multiple filament arrays. *Phys. Rev. A*, 81:043811, 2010.

[28] D. Faccio, A. Averichi, A. Couairon, A. Dubietis, R. Piskarskas, A. Matijosius, F. Bragheri, M. A. Porras, A. Piskarskas, and P. Di Trapani. Competition between phase-matching and stationarity in kerr-driven optical pulse filamentation. *Phys. Rev. E*, 74:047603, 2006.

[29] J. E. Rothenberg. Pulse splitting during self-focusing in normally dispersive media. *Opt. Commun.*, 17(8):583–585, 1992.

[30] D. Faccio, M. A. Porras, A. Dubietis, F. Bragheri, A. Couairon, and P. Di Trapani. Conical emission, pulse splitting, and x-wave parametric amplification in nonlinear dynamics of ultrashort light pulses. *Phys. Rev. Lett.*, 96:193901, 2006.

[31] A. Picozzi and M. Haelterman. Hidden coherence along space-time trajectories in parametric wave mixing. *Phys. Rev. Lett.*, 88:083901, 2002.

[32] G. G. Luther, J. V. Moloney, A. C. Newell, and E. M. Wright. Self-focusing threshold in normally dispersive media. *Opt. Lett.*, 19(12):862–864, 1994.

[33] A. Couairon, E. Gaižauskas, D. Faccio, A. Dubietis, and P. Di Trapani. Nonlinear x-wave formation by femtosecond filamentation in kerr media. *Phys. Rev. E*, 73:016608, 2006.

[34] V. Loriot, E. Hertz, O. Faucher, and B. Lavorel. Measurement of high order kerr refractive index of major air components. *Opt. Express*, 17(16):13429–13434, 2009.

[35] V. Loriot, E. Hertz, O. Faucher, and B. Lavorel. Measurement of high order kerr refractive index of major air components: erratum. *Opt. Express*, 18(3):3011–3012, 2010.

[36] P. Béjot, J. Kasparian, S. Henin, V. Loriot, T. Vieillard, E. Hertz, O. Faucher, B. Lavorel, and J.-P. Wolf. Higher-order kerr terms allow ionization-free filamentation in gases. *Phys. Rev. Lett.*, 104:103903, 2010.

[37] P. Béjot, E. Hertz, B. Lavorel, J. Kasparian, J.-P. Wolf, and O. Faucher. From higher-order kerr nonlinearities to quantitative modeling of third and fifth harmonic generation in argon. *Opt. Lett.*, 36(6):828–830, 2011.

[38] P. Béjot and J. Kasparian. Conical emission from laser filaments and higher-order kerr effect in air. *Opt. Lett.*, 36(24):4812–4814, 2011.

[39] P. Béjot, E. Hertz, J. Kasparian, B. Lavorel, J. P. Wolf, and O. Faucher. Transition from plasma-driven to kerr-driven laser filamentation. *Phys. Rev. Lett.*, 106:243902, 2011.

[40] Carsten Brée, Ayhan Demircan, and Günter Steinmeyer. Saturation of the all-optical kerr effect. *Phys. Rev. Lett.*, 106:183902, 2011.

[41] B. Borchers, C. Brée, S. Birkholz, A. Demircan, and G. Steinmeyer. Saturation of the all-optical kerr effect in solids. *Opt. Lett.*, 37(9):1541–1543, 2012.

[42] M. Kolesik, E. M. Wright, and J. V. Moloney. Femtosecond filamentation in air and higher-order nonlinearities. *Opt. Lett.*, 35(15):2550–2552, 2010.

[43] P. Polynkin, M. Kolesik, E. M. Wright, and J. V. Moloney. Experimental tests of the new paradigm for laser filamentation in gases. *Phys. Rev. Lett.*, 106:153902, 2011.

[44] O. Kosareva, J.-F. Daigle, N. Panov, T. Wang, S. Hosseini, S. Yuan, G. Roy, V. Makarov, and S. L. Chin. Arrest of self-focusing collapse in femtosecond air filaments: higher order kerr or plasma defocusing? *Opt. Lett.*, 36(7):1035–1037, 2011.

[45] J. K. Wahlstrand, Y.-H. Cheng, Y.-H. Chen, and H. M. Milchberg. Optical nonlinearity in ar and n_2 near the ionization threshold. *Phys. Rev. Lett.*, 107:103901, 2011.

[46] J. M. Brown, E. M. Wright, J. V. Moloney, and M. Kolesik. On the relative roles of higher-order nonlinearity and ionization in ultrafast light-matter interactions. *Opt. Lett.*, 37(10):1604–1606, 2012.

[47] E. Volkova, A. Popov, and O. Tikhonova. Nonlinear polarization response of an atomic gas medium in the field of a high-intensity femtosecond laser pulse. *JETP Letters*, 94:519–524, 2011.

[48] D. Strickland and G. Mourou. Compression of amplified chirped optical pulses. *Opt. Commun.*, 56:219, 1985.

[49] J. K. Ranka, R. W. Schirmer, and A. L. Gaeta. Observation of pulse splitting in nonlinear dispersive media. *Phys. Rev. Lett.*, 77(18):3783–3786, 1996.

[50] S. A. Diddams, H. K. Eaton, A. A. Zozulya, and T. S. Clement. Amplitude and phase measurements of femtosecond pulse splitting in nonlinear dispersive media. *Opt. Lett.*, 23(5):379–381, 1998.

[51] J. K. Ranka and A. L. Gaeta. Breakdown of the slowly varying envelope approximation in the self-focusing of ultrashort pulses. *Opt. Lett.*, 23(7):534–536, 1998.

[52] J. E. Rothenberg. Space-time focusing: breakdown of the slowly varying envelope approximation in the self-focusing of femtosecond pulses. *Opt. Lett.*, 17(19):1340–1342, 1992.

[53] J. T. Manassah and B. Gross. Self-focusing of (3+1)-d femtosecond pulses in nonlinear kerr media. *Laser Physics*, 6(3):563–578, 1996.

[54] J. K. Ranka and A. L. Gaeta. Breakdown of the slowly varying envelope approximation in the self-focusing of ultrashort pulses. *Opt. Lett.*, 23(7):534–536, 1998.

[55] A. A. Zozulya, S. A. Diddams, and T. S. Clement. Investigations of nonlinear femtosecond pulse propagation with the inclusion of raman, shock, and third-order phase effects. *Phys. Rev. A*, 58(4):3303–3310, 1999.

[56] A. A. Zozulya, S. A. Diddams, A. G. Van Engen, and T. S. Clement. Propagation dynamics of intense femtosecond pulses: Multiple splittings, coalescence, and continuum generation. *Phys. Rev. Lett.*, 82(7):1430–1433, 1999.

[57] S. A. Diddams, H. K. Eaton, A. A. Zozulya, and T. S. Clement. Characterizing the nonlinear propagation of femtosecond pulses in bulk media. *IEEE J. Select. Topics Quantum Electron.*, 4(2):306–316, 1998.

[58] A. Couairon and A. Mysyrowicz. Femtosecond filamentation in transparent media. *Phys. Rep.*, 441:47 – 189, 2007.

[59] G. Fibich and A. L. Gaeta. Critical power for self-focusing in bulk media and in hollow waveguides. *Opt. Lett.*, 25(5):335–337, 2000.

[60] K. D. Moll, A. L. Gaeta, and G. Fibich. Self-similar optical wave collapse: Observation of the townes profile. *Phys. Rev. Lett.*, 90(20):203902, 2003.

[61] N. Zhavoronkov. Fine control of self-compression dynamics in a femtosecond filament. *J. Opt. A: Pure Appl. Opt.*, 11:125201, 2009.

[62] M. A. Porras, A. Parola, D. Faccio, A. Couairon, and P. Di Trapani. Light-filament dynamics and the spatiotemporal instability of the townes profile. *Phys. Rev. A*, 76:011803, 2007.

[63] A. Brodeur, C. Y. Chien, F. A. Ilkov, S. L. Chin, O. G. Kosareva, and V. P. Kandidov. Moving focus in the propagation of ultrashort laser pulses in air. *Opt. Lett.*, 22(5):304–306, 1997.

[64] Y. R. Shen and Michael M. T. Loy. Theoretical interpretation of small-scale filaments of light originating from moving focal spots. *Phys. Rev. A.*, 3(6):2099–2105, 1971.

[65] G. Valiulis, J. Kilius, O. Jedrkiewicz, A. Bramati, S. Minardi, C. Conti, S. Trillo, A. Piskarskas, and P. Di Trapani. Space-time nonlinear compression and three-dimensional complex trapping in normal dispersion. In *Quantum Electronics and Laser Science Conference, 2001. QELS '01. Technical Digest. Summaries of Papers Presented at the*, pages QPD10–1 – QPD10–2, may 2001.

[66] G. Valiulis, V. Jukna, O. Jedrkiewicz, M. Clerici, E. Rubino, and P. DiTrapani. Propagation dynamics and x-pulse formation in phase-mismatched second-harmonic generation. *Phys. Rev. A*, 83:043834, 2011.

[67] D. Faccio, P. Di Trapani, S. Minardi, A. Bramati, F. Bragheri, C. Liberale, V. Degiorgio, A. Dubietis, and A. Matijosius. Far-field spectral characterization of conical emission and filamentation in kerr media. *J. Opt. Soc. Am. B*, 22(4):862–869, 2005.

[68] D. Faccio, A. Averchi, A. Lotti, M. Kolesik, J. V. Moloney, A. Couairon, and P. Di Trapani. Generation and control of extreme blueshifted continuum peaks in optical kerr media. *Phys. Rev. A*, 78:033825, 2008.

[69] F. Courvoisier, V. Boutou, J. Kasparian, E. Salmon, G. Méjean, J. Yu, and J.P. Wolf. Ultraintense light filaments transmitted through clouds. *Appl. Phys. Lett.*, 83:213, 2003.

[70] M. Kolesik and J. V. Moloney. Ultraintense light filaments transmitted through clouds. *Opt. Lett.*, 29(6):590, 2004.

[71] S. Skupin, L. Bergé, U. Peschel, and F. Lederer. Interaction of femtosecond light filaments with obscurants in aerosols. *Phys. Rev. Lett.*, 93(2):023901, 2004.

[72] W. Liu, J.-F. Gravel, F. Théberge, A. Becker, and S. L. Chin. Background reservoir: its crucial role for long-distance propagation of femtosecond laser pulses in air. *Appl. Phys. B*, 80:857–860, 2005.

[73] G. Méchain, G. Méjean, R. Ackermann, P. Rohwetter, Y.-B. André, J. Kasparian, B. Prade, K. Stelmaszczyk, J. Yu, E. Salmon, W. Winn, L.A. Schlie, A. Mysyrowicz, R. Sauerbrey, L. Wöste, and J.-P. Wolf. Background reservoir: its crucial role for long-distance propagation of femtosecond laser pulses in air. *Appl. Phys. B*, 80:785, 2005.

[74] R. Ackermann, K. Stelmaszczyk, P. Rohwetter, G. Méjean, E. Salmon, J. Yu, J. Kasparian, G. Méchain, V. Bergmann, S. Schaper, B. Weise, T. Kumm, K. Rethmeier, W. Kalkner, L. Wöste, and J.-P. Wolf. Triggering and guiding of megavolt discharges by laser-induced filaments under rain conditions. *Appl. Phys. Lett.*, 85(23):5781, 2005.

[75] R. Ackermann, G. Mejean, J. Kasparian, J. Yu, E. Salmon, and J.-P. Wolf. Triggering and guiding of megavolt discharges by laser-induced filaments under rain conditions. *Opt. Lett.*, 31(1):86, 2006.

[76] A. A. Zemlyanov and Yu. E. Geints. Filamentation length of ultrashort laser pulse in presence of aerosol layer. *Opt. Commun.*, 259:799, 2006.

[77] A. A. Zemlyanov and Yu. E. Geints. Aerosol scattering of supercontinuum radiation formed upon femtosecond laser pulse filamentation in the atmosphere. *Opt. Commun.*, 270:47, 2007.

[78] J. Kasparian and J.-P. Wolf. Physics and applications of atmospheric nonlinear optics and filamentation. *Opt. Express*, 16:466, 2008.

[79] G. Méjean, J. Kasparian, J. Yu, E. Salmon, S. Frey, J.-P. Wolf, S. Skupin, A. Vinçotte, R. Nuter, S. Champeaux, and L. Bergé. Triggering and guiding of megavolt discharges by laser-induced filaments under rain conditions. *Phys. Rev. E.*, 72:026611, 2005.

[80] V.P. Kandidov and V.O. Militsin. Computer simulation of laser pulse filament generation in rain. *Appl. Phys. B*, 83:171, 2006.

[81] W.-F. Cheong, S. A. Prahl, and A. J. Welsh. A review of the optical properties of biological tissues. *IEEE J. Quantum Electron.*, 26:2166, 1990.

[82] A. Yodh and B. Chance. Spectroscopy and imaging with diffusing light. *Phys. Today*, 48:34, 1995.

[83] J. Squier. Ultrafast optics opening new windows in biology. *Opt. Photon. News*, 13:41, 2002.

[84] P. S. Tsai, B. Friedman, J. Squier, and D. Kleinfeld. Ultrashort pulsed laser light a cool tool for ultraprecise cutting of tisue and cells. *Opt. Photon. News*, 15:24, 2004.

[85] R. Cicchi, F. S. Pavone, D. Massi, and D. D. Sampson. Contrast and depth enhancement in two-photon microscopy of human skin ex vivo by use of optical clearing agents. *Opt. Express*, 13:2337, 2005.

[86] *Oxford dictionary of physics.* Oxford University Press, Oxford, Great Brittain, 2009.

[87] A. A. Kokhanovsky. *Light scattering media optics. Problems and solutions.* Springer, New York, 2004.

[88] C.F. Bohren and D. R. Huffman. *Absorbtion and scattering of light by small particles.* Willey, New York, 2004.

[89] S. Prahl. Mie scattering calculator.

[90] A. Dubietis, A. Couairon, G. Tamošauskas E. Kučcinskas, E. Gaižauskas, D. Faccio, and P. Di Trapani. Measurement and calculation of nonlinear absorption associated with femtosecond filaments in water. *Appl. Phys. B*, 84(3):439–446, 2006.

[91] A. Ashkin, J. M. Dziedzic, and P. W. Smith. Continuous-wave self-focusing and self-trapping of light in artificial kerr media. *Opt. Lett.*, 7(6):276, 1982.

[92] C. Calba, C. Rozé, T. Girasole, and L. Méès. Monte carlo simulation of the interaction between an ultra-short pulse and a strongly scattering medium: The case of large particles. *Opt. Commun.*, 265:373, 2006.

[93] L. Bergé, S. Skupin, F. Lederer, G. Méjean, J. Yu, J. Kasparian, E. Salmon, J.P. Wolf, M. Rodriguez, L.Wöste, R. Bourayou, and R. Sauerbrey. Multiple filamentation of terawatt laser pulses in air. *Phys. Rev. Lett.*, 92:225002, 2004.

[94] S. A. Hosseini, Q. Luo, B. Ferland, W. Liu, S. L. Chin, O. G. Kosareva, N. A. Panov, N. Aközbek, and V. P. Kandidov. Competition of multiple filaments during the propagation of intense femtosecond laser pulses. *Phys. Rev. A*, 70:033802, 2004.

[95] S. Skupin, L. Bergé, U. Peschel, F. Lederer, G. Méjean, J. Yu, J. Kasparian, E. Salmon, J. P. Wolf, M. Rodriguez, L. Wöste, R. Bourayou, and R. Sauerbrey. Competition of multiple filaments during the propagation of intense femtosecond laser pulses. *Phys. Rev. E*, 70:046602, 2004.

[96] K. Cook, A. K. Kar, and R. A. Lamb. White-light supercontinuum interference of self-focused filaments in water. *Appl. Phys. Lett.*, 83(19):3861–3863, 2003.

[97] D. Faccio, A. Dubietis, G. Tamošauskas, P. Polesana, G. Valiulis, A. Piskarskas, A. Lotti, A. Couairon, and P. Di Trapani. Phase- and group-matched nonlinear interactions mediated by multiple filamentation in kerr media. *Phys. Rev. A*, 76:055802, 2007.

[98] O. G. Kosareva, T. Nguyen, N. A. Panov, W. Liu, A. Saliminia, V. P. Kandidov, N. Aközbek, M. Scalora, R. Vallée, and S. L. Chin. Array of femtosecond plasma channels in fused silica. *Opt. Commun.*, 267(2):511–523, 2006.

[99] M. Châteauneuf, S. Payeur, J. Dubois, and J.-C. Kiefer. Microwave guiding in air by a cylindrical filament array waveguide. *Appl. Phys. Lett.*, 92(9):091104, 2008.

[100] G. Méchain, A. Couairon, M. Franco, B. Prade, and A. Mysyrowicz. Organizing multiple femtosecond filaments in air. *Phys. Rev. Lett.*, 93:035003, 2004.

[101] Z. Jin, J. Zhang, M. H. Lu, Y. T. Li, Z. H. Wang, Z. Y. Wei, X. H. Yuan, and W. Yu. Control of filamentation induced by femtosecond laser pulses propagating in air. *Opt. Express*, 13(25):10424–10430, 2005.

[102] H. Schroeder, J. Liu, and S. L. Chin. From random to controlled small-scale filamentation in water. *Opt. Express*, 12(20):4768–4774, 2004.

[103] T. Pfeifer, L. Gallmann, M. J. Abel, D. M. Neumark, and S. R. Leone. Circular phase mask for control and stabilization of single optical filaments. *Opt. Lett.*, 31(15):2326–2328, 2006.

[104] A. Trisorio and C. P. Hauri. Control and characterization of multiple circularly polarized femtosecond filaments in argon. *Opt. Lett.*, 32(12):1650–1652, 2007.

[105] L. Guyon, F. Courvoisier, V. Boutou, R. Nuter, A. Vincǫtte, S. Champeaux, L. Bergé, P. Glorieux, and J.-P. Wolf. Self-organized bundle of lasing filaments in dense media. *Phys. Rev. A*, 73:051802(R), 2006.

[106] J. Liu, H. Schroeder, S. L. Chin, R. Li, and Z. Xu. Ultrafast control of multiple filamentation by ultrafast laser pulses. *Appl. Phys. Lett.*, 87(16):161105, 2005.

[107] A. Dubietis, G. Tamošauskas, P. Polesana, G. Valiulis, H. Valtna, D. Faccio, P. Di Trapani, and A. Piskarskas. Highly efficient four-wave parametric amplification in transparent bulk kerr medium. *Opt. Express*, 15(18):11126–11132, 2007.

[108] A. Dubietis, G. Tamošauskas, G. Fibich, and B. Ilan. Multiple filamentation induced by input-beam ellipticity. *Opt. Lett.*, 29(10):1126–1128, 2004.

[109] G. Fibich, S. Eisenmann, B. Ilan, and A. Ziegler. Control of multiple filamentation in air. *Opt. Lett.*, 29(15):1772–1774, 2004.

[110] M. Centurion, Y. Pu, and D. Psaltis. Self-organization of spatial solitons. *Opt. Express*, 13(16):6202–6211, 2005.

[111] T. D. Grow and A. L. Gaeta. Dependence of multiple filamentation on beam ellipticity. *Opt. Express*, 13(12):4594–4599, 2005.

[112] V. Kudriašov, E. Gaižauskas, and V. Sirutkaitis. Beam transformation and permanent modification in fused silica induced by femtosecond filaments. *J. Opt. Soc. Am. B*, 22(12):2619–2627, 2005.

[113] A. Dubietis, E. Kučinskas, and G. Tamošauskas. Formation of periodic multifilamentary structures by use of highly elliptic light beams. *Lithuanian J. Phys.*, 47(1):27–30, 2007.

[114] C. R. Giuliano, J. H. Marburger, and A. Yariv. Enhancement of self-focusing threshold in sapphire with elliptical beams. *Appl. Phys. Lett.*, 21(2):58–60, 1972.

[115] F. Cornolti, M. Lucchesi, and B. Zambon. Elliptic gaussian beam self-focusing in nonlinear media. *Opt. Commun.*, 75(2):129–135, 1990.

[116] D. Anderson, M. Bonnedal, and M. Lisak. Self-trapped cylindrical laser beams. *Phys. Fluids*, 22:1838–1840, 1979.

[117] B. Gross and J. T. Manassah. Numerical solution for the propagation of an elliptic gaussian beam in a kerr medium. *Phys. Lett. A*, 169(5):371–378, 1992.

[118] G. Fibich and B. Ilan. Self-focusing of elliptic beams: an example of the failure of the aberrationless approximation. *J. Opt. Soc. Am. B*, 17:1749–1758, 2000.

[119] G. Fibich, S. Eisenmann, B. Ilan, Y. Erlich, M. Fraenkel, Z. Henis, A. Gaeta, and A. Zigler. Self-focusing distance of very high power laser pulses. *Opt. Express*, 13(15):5897–5903, 2005.

[120] R. W. Boyd. *Nonlinear Optics*. Academic Press, San Diego, CA, 2003.

[121] N. Gavish, G. Fibich, L. T. Vuong, and A. L. Gaeta. Predicting the filamentation of high-power beams and pulses without numerical integration: A nonlinear geometrical optics method. *Phys. Rev. A*, 78:043807, 2008.

[122] R. Malendevich, L. Jankovic, and G. Stegeman. Spatial modulation instability in a kerr slab waveguide. *Opt. Lett.*, 26(23):1879–1881, 2001.

[123] M. A. C. Potenza, S. Minardi, J. Trull, G. Blasi, D. Salerno, A. Varanavičius, A. Piskarskas, and P. Di Trapani. Three dimensional imaging of short pulses. *Opt. Commun.*, 229:381–390, 2004.

[124] Q. Sun, H. Jiang, Y. Liu, Z. Wu, H. Yang, and Q. Gong. Measurement of the collision time of dense electronic plasma induced by a femtosecond laser in fused silica. *Opt. Lett.*, 30(3):320–332, 2005.

[125] Q. Sun, H. Jiang, Y. Liu, Z. Wu, H. Yang, and Q. Gong. Interspecimen comparison of the refractive index of fused silica. *J. Opt. Soc. Am.*, 55(10):1205–1208, 1965.

[126] D. Milam. Review and assessment of measured values of the nonlinear refractive-index coefficient of fused silica. *Appl. Opt.*, 37(3):546–550, 1998.

[127] J. Noack and A. Vogel. Laser-induced plasma formation in water at nanosecond to femtosecond time scales: calculation of thresholds, absorption coefficients, and energy density. *IEEE J. Quantum Electron.*, 35(8):1156–1167, 1999.

[128] D. Majus, V. Jukna, G. Valiulis, and A. Dubietis. Generation of periodic filament arrays by self-focusing of highly elliptical ultrashort pulsed laser beams. *Phys. Rev. A*, 79:033843, 2009.

[129] M. Mlejnek, M. Kolesik, J. V. Moloney, and E. M. Wright. Optically turbulent femtosecond light guide in air. *Phys. Rev. Lett.*, 83:2938, 1999.

[130] L. Bergé, S. Mauger, and S. Skupin. Multifilamentation of powerful optical pulses in silica. *Phys. Rev. A*, 81:013817, 2010.

[131] O. Jedrkiewicz, A. Picozzi, M. Clerici, D. Faccio, and P. Di Trapani. Emergence of x-shaped spatiotemporal coherence in optical waves. *Phys. Rev. Lett.*, 97:243903, 2006.

[132] O. Jedrkiewicz, M. Clerici, A. Picozzi, D. Faccio, and P. Di Trapani. X-shaped space-time coherence in optical parametric generation. *Phys. Rev. A*, 76:033823, 2007.

[133] F. Bragheri, D. Faccio, A. Couairon, A. Matijošius, G. Tamošauskas, A. Varanavičius, V. Degiorgio, A. Piskarskas, and P. Di Trapani. Conical-emission and shock-front dynamics in femtosecond laser-pulse filamentation. *Phys. Rev. A*, 76:025801, 2007.

[134] A. Couairon, E. Gaižauskas, D. Faccio, A. Dubietis, and P. Di Trapani. Manifestations of sub- and superluminality in filamented femtosecond laser pulse in fused silica. *Opt. Commun.*, 73(9):016608, 2006.

[135] S. Minardi, A. Gopal, A. Couairon, G. Tamošauskas, R. Piskarskas, A. Dubietis, and P. Di Trapani. Accurate retrieval of pulse-splitting dynamics of a femtosecond filament in water by time-resolved shadowgraphy. *Opt. Lett.*, 34(8):3020–3022, 2009.

[136] A. Saliminia, N. T. Nguyen, S. L. Chin, and R. Valée. Densification of silica glass induced by 0.8 and 1.5 μm intense femtosecond laser pulses. *J. Appl. Phys.*, 99(9):093104, 2006.

[137] K. Dysthe, H. E. Krogstad, and P.Müller. Oceanic rogue waves. *Annu. Rev. Fluid Mech.*, 40:287–310, 2008.

[138] A. N. Ganshin, V. B. Efimov, G. V. Kolmakov, L. P. Mezhov-Deglin, and P. V. E. McClintock. Observation of an inverse energy cascade in developed acoustic turbulence in superfluid helium. *Phys. Rev. Lett.*, 101:065303, 2008.

[139] Yu. V. Bludov, V. V. Konotop, and N. Akhmediev. Matter rogue waves. *Phys. Rev. A*, 80:033610, 2009.

[140] M. S. Ruderman. Freak waves in laboratory and space plasmas. *Eur. Phys. J. Special Topics*, 185:57–66, 2010.

[141] L. Stenflo and M. Marklund. Rogue waves in the atmosphere. *J. Plasma Phys.*, 76:293–295, 2010.

[142] N. Akhmediev and E. Pelinovsky. Rogue waves − towards a unifying concept? *Eur. Phys. J. Spec. Top.*, 185:1–266, 2010.

[143] A. I. Dyachenko and V. E. Zakharov. Modulation instability of stokes wave implies a freak wave. *JETP Lett.*, 81:255–259, 2005.

[144] N. Akhmediev, J. M. Soto-Crespo, and A. Ankiewicz. Extreme waves that appear from nowhere: On the nature of rogue waves. *Phys. Lett. A*, 373(25):2137–2145, 2009.

[145] D. R. Solli, C. Ropers, P. Koonath, and B. Jalali1. Optical rogue waves. *Nature*, 450:1054, 2007.

[146] M. Erkintalo, G. Genty, and J. M. Dudley. Giant dispersive wave generation through soliton collision. *Opt. Lett.*, 35(5):658–660, 2010.

[147] J. M. Dudley, G. Genty, and B. J. Eggleton. Harnessing and control of optical rogue waves in supercontinuum generation. *Opt. Express*, 16(6):3644–3651, 2008.

[148] A. Mussot, A. Kudlinski, M. Kolobov, E. Louvergneaux, M. Douay, and M. Taki. Observation of extreme temporal events?in cw-pumped supercontinuum. *Opt. Express*, 17(19):17010–17015, 2009.

[149] D. R. Solli, C. Ropers, and B. Jalali. Active control of rogue waves for stimulated supercontinuum generation. *Phys. Rev. Lett.*, 101:233902, 2008.

[150] M. Erkintalo, G. Genty, and J. M. Dudley. Rogue-wave-like characteristics in femtosecond supercontinuum generation. *Opt. Lett.*, 34(16):2468–2470, 2009.

[151] A. Kudlinski, B. Barviau, A. Leray, C. Spriet, L. Héliot, and A. Mussot. Control of pulse-to-pulse fluctuations in visible supercontinuum. *Opt. Express*, 18(26):27445–27454, 2010.

[152] A. Aalto, G. Genty, and J. Toivonen. Extreme-value statistics in supercontinuum generation by cascaded stimulated raman scattering. *Opt. Express*, 18(2):1234–1239, 2010.

[153] K. Hammani, A. Picozzi, and C. Finot. Extreme statistics in raman fiber amplifiers: From analytical description to experiments. *Opt. Commun.*, 284(10-11):2594–2603, 2011.

[154] A. Montina, U. Bortolozzo, S. Residori, and F. T. Arecchi. Non-gaussian statistics and extreme waves in a nonlinear optical cavity. *Phys. Rev. Lett.*, 103:173901, 2009.

[155] A. Maluckova, Lj. Hadžievski, N. Lazarides, and G. P. Tsironis. Extreme events in discrete nonlinear lattices. *Phys. Rev. E*, 79:025601(R), 2009.

[156] Yu. V. Bludov, V. V. Konotop, and N. Akhmediev. Rogue waves as spatial energy concentrators in arrays of nonlinear waveguides. *Opt. Lett.*, 34(19):3015–3017, 2009.

[157] J. Kasparian, P. Bjot, J. P. Wolf, and J. M. Dudley. Optical rogue wave statistics in laser filamentation. *Opt. Express*, 17(14):12070–12075, 2009.

[158] D. Kiselev, L. Woeste, and J.-P. Wolf. Filament-induced laser machining (film). *Appl. Phys. B.*, 100(3):515–520, 2010.

[159] C. Conti, S. Trillo, P. Di Trapani, G. Valiulis, A. Piskarskas, O. Jedrkiewicz, and J. Trull. Nonlinear electromagnetic x waves. *Phys. Rev. Lett.*, 90:170406, 2003.

[160] M. Daimon and A. Masumura. Measurement of the refractive index of distilled water from the near-infrared region to the ultraviolet region. *Appl. Opt.*, 46(18):3811–3820, 2007.

[161] S. Minardi, A. Gopal, M. Tatarakis, A. Couairon, G. Tamošauskas, R. Piskarskas, A. Dubietis, and P. Di Trapani. Time-resolved refractive index and absorption mapping of light-plasma filaments in water. *Opt. Lett.*, 33(1):86–88, 2008.

[162] R. M. Pope and E. S. Fry. Absorption spectrum (380 − 700 nm) of pure water. ii. integrating cavity measurements. *Appl. Opt.*, 36(33):8710–8723, 1997.

[163] L. Kou, D. Labrie, and P. Chylek. Refractive indices of water and ice in the 0.65- to 2.5-m spectral range. *Appl. Opt.*, 32(19):3531–3540, 1993.

[164] A. L. Gaeta. Catastrophic collapse of ultrashort pulses. *Phys. Rev. Lett.*, 84:3582, 2000.

[165] B. Prade, M. Franco, A. Mysyrowicz, A. Couairon, H. Buersing, B. Eberle, M. Krenz, D. Seiffer, and O. Vasseur. Spatial mode cleaning by femtosecond filamentation in air. *Opt. Lett.*, 31(17):2601–2603, 2006.

[166] S.L. Chin, F. Thberge, and W. Liu. Filamentation nonlinear optics. *Appl. Phys. B.*, 86:477–483, 2007.

[167] W. W. Liu and S. Chin. Understanding the beam self-cleaning behavior of ultrashort laser pulse filamentation. *Sci. China Ser. E-Tech. Sci.*, 50:413–421, 2007.

[168] V. Jukna, D. Majus, G. Valiulis, and A. Dubietis. Transformation of the probability density function in an optical parametric amplifier: Application to rogue-wave-like statistics. *Opt. Commun.*, 285:3654–3658, 2012.

[169] D. Majus, V. Jukna, E. Pileckis, G. Valiulis, and A. Dubietis. Rogue-wave-like statistics in ultrafast white-light continuum generation in sapphire. *Opt. Express*, 19(17):16317–16323, 2011.

[170] J. Lu and J. F. Greenleaf. Experimental verification of nondiffracting x waves. *IEEE Trans. Ultrason. Ferroelectr. Freq. Control*, 39(3):441–446, 1992.

[171] E. Larose, L. Margerin, B. A. van Tiggelen, and M. Campillo. Weak localization of seismic waves. *Phys. Rev. Lett.*, 93:048501, 2004.